

NASA TECHNICAL NOTE



NASA TN D-4578

NASA TN D-4578

PRELIMINARY FLIGHT EVALUATION OF  
THE STABILITY AND CONTROL DERIVATIVES  
AND DYNAMIC CHARACTERISTICS OF THE  
UNAugMENTED XB-70-1 AIRPLANE  
INCLUDING COMPARISONS WITH PREDICTIONS

*by Chester H. Wolowicz, Larry W. Strutz, Glenn B. Gilyard,  
and Neil W. Matheny*

*Flight Research Center  
Edwards, Calif.*

NATIONAL AERONAUTICS AND SPACE ADMINISTRATION • WASHINGTON, D. C. • MAY 1968

PRELIMINARY FLIGHT EVALUATION OF THE STABILITY AND  
CONTROL DERIVATIVES AND DYNAMIC CHARACTERISTICS  
OF THE UNAUGMENTED XB-70-1 AIRPLANE INCLUDING  
COMPARISONS WITH PREDICTIONS

By Chester H. Wolowicz, Larry W. Strutz,  
Glenn B. Gilyard, and Neil W. Matheny

Flight Research Center  
Edwards, Calif.

NATIONAL AERONAUTICS AND SPACE ADMINISTRATION

PRELIMINARY FLIGHT EVALUATION OF THE STABILITY AND  
CONTROL DERIVATIVES AND DYNAMIC CHARACTERISTICS  
OF THE UNAUGMENTED XB-70-1 AIRPLANE INCLUDING  
COMPARISONS WITH PREDICTIONS

By Chester H. Wolowicz, Larry W. Strutz,  
Glenn B. Gilyard, and Neil W. Matheny  
Flight Research Center

SUMMARY

Stability and control characteristics of the XB-70-1 airplane were evaluated from data obtained during the early phases of the flight-test program at Mach numbers extending to 2.56 and altitudes to 64,700 feet (19,700 meters).

Flight-determined stability and control derivatives and dynamic characteristics for three wing-tip configurations were found generally to be in fair agreement with predictions based on wind-tunnel tests and theoretical estimates of structural flexibility effects.

The results show the short-period and Dutch roll modes of the unaugmented aircraft to be positively damped for the flight conditions evaluated. Longitudinal damping characteristics tended generally to correspond with predictions for the flexible aircraft; a fairly heavy damping ratio of the order of 0.5 was evident at low subsonic speeds and a light damping ratio of the order of 0.1 at high supersonic speeds. Dutch roll damping of the order of 0.2 or less throughout the Mach number range was underestimated at supersonic conditions, primarily as a result of underestimating the yaw damping due to yaw rate.

The neutral point was approximately 30 percent of the mean aerodynamic chord for 25° and 65° wing-tip configurations at supersonic conditions and 27 percent to 29 percent of the mean aerodynamic chord subsonically with the wing tips up. The predicted values were slightly higher.

The airplane exhibited negative (adverse) values of the aileron-yaw parameter  $C_{n\delta_a}$  at Mach numbers above about 0.90, although proverse values were predicted.

Positive values were obtained at subsonic speeds, but the flight-measured values were less than predicted.

The flight-determined effective dihedral was negative for fully deflected wing tips (65°) and higher than predicted. The combination of negative effective dihedral and adverse aileron yaw was conducive to divergent pilot-induced oscillation tendencies.

Flight tests showed a marked reduction in directional stability beyond approximately 2° of sideslip. This nonlinearity was found in wind-tunnel studies to be the result of canard interference.

Comparison of the results from rigid-model wind-tunnel tests with those from flight shows that the effects of aeroelasticity appear to be significant for the static pitch stability, pitch-control effectiveness, roll-control effectiveness, static directional stability, and effective dihedral derivatives.

## INTRODUCTION

The XB-70 is a large, high performance, supersonic aircraft (fig. 1) and represents the closest approach in size and weight to the proposed supersonic transports, with similar structural and performance characteristics. It therefore provides an excellent test vehicle for obtaining data pertinent to the development of the supersonic transport.

The XB-70 flight-test program is a two-phase operation. The first phase, which ended in June 1966, was a joint North American Aviation/Air Force program in which the performance capabilities of the aircraft were demonstrated. The second phase of the program, which started in March 1967, is a joint NASA/Air Force research effort to obtain additional data primarily in support of the supersonic-transport program.

A substantial amount of stability and control data was obtained throughout the flight envelope of the aircraft during the first phase of the program. Although the information was obtained under more or less random conditions of altitude, weight, and center of gravity, it is of sufficient scope to warrant a preliminary evaluation of the stability and control characteristics of the aircraft. This report summarizes the results of the evaluation and compares the flight-determined derivatives with those obtained from wind-tunnel tests and with estimated effects of aeroelasticity.

The flight data presented were derived from tests of the XB-70-1 aircraft extending to a Mach number of 2.56 and an altitude of 64,700 feet (19,700 meters). The data, for the most part, fall within a relatively small band that closely resembles typical climbout corridors of the proposed supersonic transport. Thus, to provide a more consistent basis for discussion of the correlation of the flight data with the predicted characteristics, the flight data were adjusted to correspond to a hypothetical supersonic transport mid-corridor climbout profile. The data determined at actual flight-test conditions are also included for comparative reference.

## SYMBOLS

The data presented are in the form of standard NASA coefficients of forces and moments which are referred to the body axes passing through the center of gravity. The positive directions are: X, forward; Y, to the right; Z, down. Positive directions of the forces, moments, and angular displacements and velocities are in accord with the right-hand rule.

Measurements were taken in the U. S. Customary System of Units. Equivalent values in the International System of Units (SI) are indicated. Details concerning the use of SI, together with physical constants and conversions, are given in reference 1.

The coefficients are defined in terms of the span, area, and mean aerodynamic chord of the wing-tips-up configuration.

$a_n$	normal acceleration at center of gravity, g units
$a_{ni}$	indicated normal acceleration uncorrected for instrument position, g units
$a_t$	transverse acceleration at center of gravity, g units
$a_{ti}$	indicated transverse acceleration uncorrected for instrument position, g units
$b$	wing span, tips undeflected, feet (meters)
$C_L$	lift coefficient, $\frac{\text{Lift}}{\bar{q}S}$
$C_l$	rolling-moment coefficient, $\frac{\text{Rolling moment}}{\bar{q}Sb}$
$C_{l_p}$	damping-in-roll derivative, $\frac{\partial C_l}{\partial \frac{pb}{2V}}$ , per radian
$C_{l_r} = \frac{\partial C_l}{\partial \frac{rb}{2V}}$	, per radian
$C_{l_\beta}$	effective dihedral derivative, $\frac{\partial C_l}{\partial \beta}$ , per degree
$C_{l_{\delta_a}}$	roll-control derivative, $\frac{\partial C_l}{\partial \delta_a}$ , per degree
$C_{l_{\delta_r}} = \frac{\partial C_l}{\partial \delta_r}$	, per degree
$C_m$	pitching-moment coefficient, $\frac{\text{Pitching moment}}{\bar{q}S\bar{c}}$
$C_{m_0}$	pitching-moment coefficient at zero lift with $\delta_c = \delta_e = 0$
$C_{m_q} = \frac{\partial C_m}{\partial \frac{q\bar{c}}{2V}}$	, per radian

$C_{m_\alpha}$  static pitch-stability derivative,  $\frac{\partial C_m}{\partial \alpha}$ , per degree

$$C_{m_{\dot{\alpha}}} = \frac{\partial C_m}{\partial \frac{\dot{\alpha} \bar{c}}{2V}}, \text{ per radian}$$

$$C_{m_{\delta_c}} = \frac{\partial C_m}{\partial \delta_c}, \text{ per degree}$$

$$C_{m_{\delta_e}} = \frac{\partial C_m}{\partial \delta_e}, \text{ per degree}$$

$C_{m_{\bar{\delta}_e}}$  pitch-control derivative,  $C_{m_{\delta_e}} + C_{m_{\delta_c}} \left( \frac{d\delta_c}{d\delta_e} \right)$ , per degree

$C_N$  normal-force coefficient,  $\frac{\text{Normal force}}{\bar{q}S}$

$$C_{N_\alpha} = \frac{\partial C_N}{\partial \alpha}, \text{ per degree}$$

$$C_{N_{\dot{\alpha}}} = \frac{\partial C_N}{\partial \frac{\dot{\alpha} \bar{c}}{2V}}, \text{ per radian}$$

$$C_{N_{\delta_c}} = \frac{\partial C_N}{\partial \delta_c}, \text{ per degree}$$

$$C_{N_{\delta_e}} = \frac{\partial C_N}{\partial \delta_e}, \text{ per degree}$$

$$C_{N_{\bar{\delta}_e}} = C_{N_{\delta_e}} + C_{N_{\delta_c}} \left( \frac{d\delta_c}{d\delta_e} \right), \text{ per degree}$$

$$C_{N_q} = \frac{\partial C_N}{\partial \frac{q \bar{c}}{2V}}, \text{ per radian}$$

$C_n$  yawing-moment coefficient,  $\frac{\text{Yawing moment}}{\bar{q}Sb}$

$$C_{n_p} = \frac{\partial C_n}{\partial \frac{pb}{2V}}, \text{ per radian}$$

$$C_{n_r} = \frac{\partial C_n}{\partial \frac{rb}{2V}}, \text{ per radian}$$

$$C_{n_\beta} \quad \text{static directional-stability derivative, } \frac{\partial C_n}{\partial \beta}, \text{ per degree}$$

$$C_{n_{\delta_a}} = \frac{\partial C_n}{\partial \delta_a}, \text{ per degree}$$

$$C_{n_{\delta_r}} = \frac{\partial C_n}{\partial \delta_r}, \text{ per degree}$$

$$C_y \quad \text{lateral-force coefficient, } \frac{\text{Lateral force}}{\bar{q}S}$$

$$C_{y_\beta} = \frac{\partial C_y}{\partial \beta}, \text{ per degree}$$

$$C_{y_{\delta_a}} = \frac{\partial C_y}{\partial \delta_a}, \text{ per degree}$$

$$C_{y_{\delta_r}} = \frac{\partial C_y}{\partial \delta_r}, \text{ per degree}$$

$$\bar{c} \quad \text{mean aerodynamic chord, tips undeflected, feet (meters)}$$

$$g \quad \text{acceleration of gravity, feet/second}^2 \text{ (meters/second}^2\text{)}$$

$$h_p \quad \text{pressure altitude, feet (meters)}$$

$$I_X, I_Y, I_Z \quad \text{moments of inertia about X-, Y-, and Z-body axes, respectively, slug-foot}^2 \text{ (kilogram-meter}^2\text{)}$$

$$I_{XZ} \quad \text{product of inertia referred to the body X- and Z-axes, slug-foot}^2 \text{ (kilogram-meter}^2\text{)}$$

$$M \quad \text{Mach number}$$

$m$	mass, slugs (kilograms)
$N_{Re}$	Reynolds number, $\frac{\rho V \bar{c}}{\mu}$
$P$	period of damped natural frequency of the airplane, seconds
$p, q, r$	time rate of change of roll, pitch, and yaw about body X-, Y-, and Z-axes, respectively, radians/second (unless noted otherwise)
$\dot{p}, \dot{q}, \dot{r}$	time rate of change of $p$ , $q$ , and $r$ , respectively, radians/second <sup>2</sup> (unless noted otherwise)
$\bar{q}$	dynamic pressure, $\frac{1}{2}\rho V^2$ , pounds/foot <sup>2</sup> (newtons/meter <sup>2</sup> )
$S$	wing area, tips undeflected, feet <sup>2</sup> (meters <sup>2</sup> )
$T_s, T_r$	spiral- and roll-mode time constants, respectively, seconds
$T_{1/2}$	time required for absolute value of transient oscillation to damp to one-half amplitude, seconds
$t$	time, seconds
$V$	true airspeed of airplane, feet/second (meters/second)
$x_{a_n}, x_{a_t}, x_\alpha, x_\beta$	distance from center of gravity to normal- and transverse-acceleration sensors and $\alpha$ and $\beta$ sensors, respectively, measured parallel to X-body axis, positive when forward of center of gravity, feet (meters)
$z_{a_t}, z_\beta$	distance from center of gravity to respective sensors as measured parallel to the Z-body axis, positive when below center of gravity, feet (meters)
$\alpha, \beta$	angle of attack and angle of sideslip, respectively, degrees
$\dot{\alpha}, \dot{\beta}$	time rate of change of $\alpha$ and $\beta$ , respectively, radians/second
$\Delta$	perturbed value
$\delta_c$	canard deflection, positive when leading edge up, degrees
$\delta_e, \delta_a, \delta_r$	average elevon, aileron, and rudder deflections, respectively: trailing edge of elevator down, positive; total aileron deflection that produces right roll, positive; trailing edge of both rudders to left, positive, degrees

$\frac{d\delta_c}{d\delta_e}$  gearing ratio of canard deflection to elevator deflection (see fig. 4)

$\delta_T$  wing-tip position, degrees

$\zeta$  ratio of actual damping to critical damping

$\theta, \varphi, \psi$  Euler angles of pitch, roll, and yaw, respectively, degrees

$\dot{\theta}, \dot{\varphi}$  time rate of change of  $\theta$  and  $\varphi$ , respectively, radians/second

$\rho$  mass density of air, slugs/foot<sup>3</sup> (kilograms/meter<sup>3</sup>)

$\omega_n$  undamped natural frequency, radians/second

$\mu$  coefficient of absolute viscosity, pound-second/foot<sup>2</sup>  
(newton-second/meter<sup>2</sup>)

Subscripts:

i indicated quantity

o initial value

The phase angle of a vector  $j$  relative to another vector  $k$  is indicated by  $\phi_{jk}$ . The second subscript  $k$  designates the reference vector.

## AIRPLANE

The XB-70 airplane (fig. 1) was originally designed as a weapons system with long-range supersonic-cruise capabilities. The two airplanes built were identical in configuration except that the first airplane (XB-70-1) had zero geometric dihedral, and the second (XB-70-2) had 5° geometric dihedral. The tip deflections with respect to the horizontal plane remained the same. The derivatives and dynamic characteristics in this paper were determined only for the XB-70-1. The physical characteristics of the XB-70-1 are given in table I.

The airplane has a design gross weight in excess of 500,000 pounds (226,800 kilograms) and a design cruising speed of Mach 3.0 at approximately 70,000 feet (21,300 meters) altitude. It has a thin, low-aspect-ratio, highly swept delta wing with folding wing tips, twin movable vertical stabilizers, elevon surfaces for pitch and roll control, a movable canard with trailing-edge flaps, and twin inlets enclosed in a single nacelle.

The normal operational limits for the three wing-tip configurations are shown in figure 2.

## Control System

The control system, described in detail in reference 2, is irreversible. Some of the pertinent external aspects are shown in figure 3.

The canard surface provides part of the pitch control and has a flap surface for use during takeoff and landing. In the normal flight configuration, the canard is geared to the elevator action of the elevons through a ratio of 1 to -6.67, as shown in figure 4. Coordinated movement of the two surfaces is provided by the pitch-control column in the cockpit. Full elevator travel of the elevons for the first phase of the flight program was  $15^\circ$  to  $-25^\circ$ ; corresponding full travel of the canard was  $0^\circ$  to  $6^\circ$  with a setting of  $2.25^\circ$  when elevators were at zero deflection. For normal takeoffs and landings, the forepart of the canard is fixed at  $0^\circ$  incidence and the canard flap is full down at  $20^\circ$ . The additional down elevator required to trim out the pitching moments due to this canard-flap configuration provides additional lift.

The elevons are segmented with six segments on each wing semispan to prevent binding as a result of bending of the wing. When the wing tips are in the deflected position, the two outboard segments on each tip are faired at a zero setting and become part of the folded tip.

Roll control is obtained by differential action of the elevons. Yaw control is provided by rotation of the vertical stabilizers about a  $45^\circ$  hinge line.

The airplane is equipped with a flight augmentation control system to provide added stability to the vehicle in pitch, roll, and yaw. It is also equipped with a lateral bob-weight to augment the Dutch roll stability above a Mach number of 2.6.

## Propulsion System

Propulsion is provided by six YJ93-GE-3 engines equipped with afterburners. Each engine has a 30,000-pound (133,200-newton) thrust classification at sea level. The six engines are mounted side by side in the rear of the fuselage in a single nacelle under the center section of the wing. The nacelle is divided into twin inlets; each inlet provides air to three engines.

The left- and right-hand air-intake ducts are each equipped with six inlet-air bypass doors on top of each duct just forward and between the leading edge of the vertical stabilizers (fig. 1). These doors are manually controlled in conjunction with the variable two-dimensional throats on the XB-70-1 to control the position of the normal shock in each of the ducts. The position of the bypass doors causes changes in pitch trim and lift with symmetrical bypass-door deflection (ref. 3).

## INSTRUMENTATION

A pulse code modulation (PCM) system is used to enable rapid processing of approximately 1100 parameters. The system converts analog signals from the sensor to digital format and records the digitized data on tape on a time-sharing basis.

The instrumentation pertinent to the stability and control investigation is listed in table II. Included are instrument location, accuracy, range, and sampling rate of the sensor signals.

The Euler attitude, angular rate, and linear accelerometers were aligned to within approximately  $0.5^\circ$  relative to the body axes.

The Mach numbers presented, as determined with a nose-boom sensor, are considered to be accurate to within 0.01 below  $M = 1.0$ , within 0.03 at  $M = 1.0$ , within 0.02 at  $M = 1.5$ , and within 0.03 at  $M = 2.0$ . Above  $M = 2.0$ , the error increases with increasing Mach number to approximately 0.09 at  $M = 3.0$ .

## FLIGHT DATA

### Test Conditions

The flight conditions associated with the various stability and control data are shown in figure 5 and are summarized in tables III and IV. The climbout and descent profiles shown in the figure are typical for a Mach 3.0 flight.

The longitudinal characteristics were determined from pullup and release maneuvers, which included transient oscillations following release. The lateral-directional characteristics were determined from "release from sideslip" maneuvers. The pitch mode of the flight augmentation control system was off for the longitudinal maneuvers; the roll and yaw modes were off for the lateral-directional maneuvers.

In general, the maneuvers were performed with no direct or systematic control of weight, center of gravity, or altitude.

### Midcorridor Climbout Profile

Most of the data points in figure 5 fall within a relatively narrow corridor approximately midway between the boundaries of the flight envelope and in figure 6 lie in a profile which is typical of the climbout profiles proposed for the supersonic transport. To minimize the scatter in the data caused by the more or less random conditions of weight and center of gravity within this midcorridor range, the flight data were normalized to a common set of conditions defined by the variations in weight, center of gravity, and inertia with Mach number shown in figures 7 to 9 for climbout portions of a typical Mach 3.0 flight of the XB-70. The normalizing procedure consisted of determining the incremental differences in the predicted derivative characteristics corresponding to the differences in flight and midcorridor weight and center of gravity for each point in the corridor and applying these derivative increments directly to the flight-determined derivatives. These increments were in general small, and the overall accuracy of the results was not significantly compromised. The resulting modified data were used as the basis for the discussion and are designated hereafter as flight-based data. These data represent the derivative variations along the hypothetical midcorridor climbout profile. The data for the actual flight-test conditions are included for comparative reference.

## Data Analysis and Accuracy

A study of the time histories of pullup and release maneuvers and release from sideslip maneuvers showed that simple analytical techniques for determining longitudinal and lateral-directional stability and control derivatives (ref. 4) would not be adequate for determining most of the derivatives. The quality of the maneuvers and recorded data during the first phase of the program were, in general, substandard for detailed analysis of the stability and control characteristics. As a result, the technique of matching flight time histories of maneuvers on an analog (ref. 5) was used. The limitations of the data that necessitated the use of this technique are discussed in appendix A, and the mathematical relationships used are summarized in appendix B. Typical analog matches are shown in figures 10(a) and 10(b) and figure 11.

The longitudinal short-period, the Dutch roll, spiral, and roll-subsidence characteristics could not be determined directly from the flight time histories because of the effects of pilot control inputs. Instead, these characteristics were calculated from the actual flight-determined derivatives, and the characteristics in the mid-corridor profile were calculated at climbout conditions from the flight-based derivatives. Digital programs based on the dynamics equations in appendix B were used for this purpose.

The uncertainty in the value of each derivative was estimated by varying the magnitude of the derivative in both directions from the best match value until a noticeable mismatch became evident. The average of the increments from the best match value was then taken to be a measure of the uncertainty. This technique was strongly influenced by the damping characteristics at the flight-test condition as well as by the quality of the maneuver.

The maximum uncertainties of the longitudinal derivatives in percent of the best match values are summarized in the following table, although in most cases the actual uncertainties were considerably less than the maximum values listed:

Derivatives	Maximum uncertainty, percent	
	Subsonic	Supersonic
$C_{N_\alpha}$	20	10
$C_{N_{\bar{\delta}_e}}$	100	30
$(C_{N_q} + C_{N_{\dot{\alpha}}})$	Over 200	Over 200
$C_{m_\alpha}$	10	5
$C_{m_{\bar{\delta}_e}}$	20	10
$(C_{m_q} + C_{m_{\dot{\alpha}}})$	40	30

On the basis of these results, only the derivatives  $C_{N_\alpha}$ ,  $C_{m_\alpha}$ ,  $(C_{m_q} + C_{m_{\dot{\alpha}}})$ , and  $C_{m_{\bar{\delta}_e}}$  were believed to be sufficiently accurate for further consideration.

The following maximum uncertainties were estimated for the lateral-directional derivatives:

Derivatives	Uncertainty, percent
$C_{n\beta}$	5
$C_{l\beta}$	15 (approximately $\pm 0.00005$ when $C_{l\beta} \approx 0$ )
$C_{y\beta}$	20
$C_{nr}$	30
$C_{np}$	20 to 100 (approximately $\pm 0.01$ when $C_{np} \approx 0$ )
$C_{lp}$	30
$C_{lr}$	50 (approximately 0.01 to 0.05 when $C_{lr} \approx 0$ )
$C_{n\delta_r}$	5
$C_{l\delta_a}$	15
$C_{n\delta_a}$	30 (approximately 0.000005 when $C_{n\delta_a} \approx 0$ )
$C_{l\delta_r}$	30 (approximately 0.000005 when $C_{l\delta_r} \approx 0$ )
$C_{y\delta_r}$	50
$C_{y\delta_a}$	100

All the derivatives except  $C_{y\delta_a}$  have been retained in this report.

## PREDICTED CHARACTERISTICS

Predicted rigid and flexible aircraft derivatives for 1g flight conditions were provided by the manufacturer (ref. 6) for each wing-tip configuration at a lightweight and a heavyweight condition with 0.222 $\bar{c}$  center of gravity and a midweight condition with 0.197 $\bar{c}$  center of gravity. The rigid aircraft static stability and control derivatives were obtained from wind-tunnel data based primarily on a 0.03-scale model. Some of these data were also obtained from an 0.008-scale model. The rigid-model data were not corrected for possible elastic distortions of the model. The manufacturer considered the elastic effects to be negligible for the low Reynolds numbers and corresponding low-dynamic pressures of most of the tests. Flexibility effects on the full-scale airplane were calculated by using the modal approach discussed in reference 7. As pointed out in the reference, the rigid-model aerodynamic data were linearized, and flexible-to-rigid ratios for the aerodynamic corrections were generated by using modal data. The rigid-aircraft rotary derivatives were calculated.

The predicted derivatives for any specific flight or flight-based condition in this report were obtained by interpolation of the manufacturer's predicted characteristics.

## RESULTS

The results of the investigation are presented in terms of the actual flight test conditions and the conditions along the flight-based hypothetical climbout profile. The stability and control derivatives and aircraft dynamics for both conditions are compared with predictions for the rigid and flexible aircraft wherever the predicted characteristics were available.

The longitudinal characteristics for actual flight-test conditions (table III) are summarized in figures 12 to 14. For the lateral-directional flight-test conditions (table IV) the results are summarized in figures 15 to 19.

The longitudinal characteristics for the flight-based midcorridor climbout conditions are summarized in figures 20 to 23 and the lateral-directional conditions in figures 24 to 30.

## DISCUSSION

As mentioned previously, this discussion is limited to the hypothetical midcorridor climbout conditions in order to provide a more consistent basis for comparison with predictions. Factors which could affect the correlation of the predicted and flight-determined characteristics include wind-tunnel techniques, the large difference in Reynolds number between flight and wind-tunnel tests (table V), and the adequacy of the theoretical correction to rigid-model data to account for aeroelastic effects. The wind-tunnel tests were made with no attempt to simulate pressure changes due to the inlet and exhaust flows; also, many of the tests were made with nonsegmented elevons.

The stability and control tests in flight were performed in such a manner that the separate effects of aeroelasticity and Reynolds number could not be determined.

## Longitudinal Characteristics

Stability and control derivatives. — Figures 20(a) and 20(b) compare the derivatives  $C_{N_\alpha}$ ,  $C_{m_\alpha}$ ,  $C_{m_{\delta_e}}$ , and  $(C_{m_q} + C_{m_{\dot{\alpha}}})$  for the midcorridor climbout conditions with predictions for a rigid and a flexible aircraft. In general, the flight-based and predicted (flexible aircraft) characteristics are in fairly good agreement for the three wing-tip deflections ( $0^\circ$ ,  $25^\circ$ ,  $65^\circ$ ) investigated. In most instances, the aeroelastic corrections are significant and, in general, bring the rigid-model data into improved agreement with the flight-based trends. Some notable discrepancies are evident in  $C_{N_\alpha}$  for  $\delta_T = 25^\circ$ ,  $C_{m_{\delta_e}}$  for  $\delta_T = 0^\circ$ , and  $(C_{m_q} + C_{m_{\dot{\alpha}}})$  for both  $\delta_T = 0^\circ$  and  $\delta_T = 25^\circ$ . These discrepancies are believed to be due in part to the large difference between the Reynolds numbers for the flight and wind-tunnel tests (approximately  $100$  to  $300 \times 10^6$  and  $2$  to  $27 \times 10^6$ , respectively). Duplication of flight Reynolds numbers for aircraft as large as the XB-70, however, is beyond the capability of existing wind tunnels. Figure 21 shows the results of a study performed in the 11- by 11-foot wind tunnel at the NASA Ames Research Center to assess the effect of Reynolds number in the range from  $9.4 \times 10^6$  to  $21.2 \times 10^6$  by varying the tunnel stagnation pressure at a Mach number of 1.2. Apparent reductions in both  $C_{m_\alpha}$  and  $C_{m_{\delta_e}}$  with increasing Reynolds number appear to be consistent with the trend of the flight data. The wind-tunnel results, however, are believed to be masked by aeroelastic distortions in the model as a result of the increased dynamic pressure (fig. 21) at the highest Reynolds number.

The flight-based pitch-damping derivatives  $(C_{m_q} + C_{m_{\dot{\alpha}}})$  in figure 20(b) appear to indicate a reasonable trend toward correlation with predictions for the flexible aircraft in the subsonic and supersonic regions. The lack of correlation in the transonic region implies rapid changes of the derivative in this region where wind-tunnel data were very limited between Mach numbers of 0.95 and 1.20.

The change in longitudinal characteristics as a result of a change in wing-tip configuration from  $0^\circ$  to  $25^\circ$  (fig. 20) could not be accurately determined from the flight-based data in the transonic region because of the sparsity and seeming scatter in the data for  $\delta_T = 25^\circ$ . The predictions, however, do indicate some decrease in  $C_{m_\alpha}$  as a result of deflection of the tips to  $25^\circ$ . The trend of the data indicates that changing the wing-tip deflection from  $25^\circ$  to  $65^\circ$  reduced  $C_{m_\alpha}$  significantly but otherwise had little effect on the longitudinal characteristics.

The zero-lift pitching-moment coefficient  $C_{m_0}$  for zero elevator and canard deflections was based on the following expression:

$$C_{m_0} = -C_{m_\alpha}(\alpha - \alpha_0) - C_{m_{\delta_e}}\delta_e - C_{m_{\delta_c}}\delta_c = -\frac{C_{m_\alpha}}{C_{N_\alpha}} \left[ C_N - C_{N_{\delta_e}}\delta_e - C_{N_{\delta_c}}(2.25) \right] - C_{m_{\delta_e}}\delta_e - 2.25C_{m_{\delta_c}}$$

Since it was not possible to determine  $C_{m\delta_c}$  and  $C_{N\delta_c}$  from the flight data, predicted values for the flexible aircraft were used in determining the zero-lift flight pitching-moment coefficient. The results are presented in figure 22, which shows the flight-based  $C_{m_0}$  to be generally larger than predicted.

Figure 22 also shows the flight-based neutral points to range from 27 percent to 29 percent of the mean aerodynamic chord at subsonic speeds ( $\delta_T = 0^\circ$ ) and approximately 30 percent of the mean aerodynamic chord with the tips at  $25^\circ$  and  $65^\circ$ , and to be slightly ahead of the predicted values. The effect of deflecting the wing tips from  $0^\circ$  to  $25^\circ$  is not clearly defined in the flight-based data; however, the predicted trends indicate a forward shift in neutral point with increasing tip deflection.

Short-period dynamics.— The unaugmented longitudinal short-period dynamics summarized in figure 23 indicate the flight-based and predicted periods to be generally in good agreement. The damping ratios show fairly heavy damping in the subsonic region and light damping in the supersonic region. Changes in tip configuration do not appear, in general, to have a significant effect on the longitudinal dynamics.

#### Lateral-Directional Characteristics

Control derivatives.— One of the more difficult characteristics to predict for a large flexible aircraft is the adverse yaw due to aileron. A comparison of flight-based and predicted characteristics in figure 24(a) shows the predicted  $C_{n\delta_a}$  to be positive (proverse), whereas the flight-based values are negative (adverse) from a Mach number of approximately 0.90 through the supersonic range. The strongest adverse-yaw effects due to aileron were encountered in flight at  $M = 0.95$  for  $\delta_T = 0^\circ$  and  $25^\circ$  and through the lower supersonic region for  $\delta_T = 65^\circ$ . It should be noted that in the subsonic region of figure 24(a) the predicted and flight-based trends are both positive (proverse), with the flight-based value lower in magnitude. Conversely, figure 15(a) shows the flight value of  $C_{n\delta_a}$  at  $M = 0.51$  for the gear-down and flaps-down configuration to be adverse. Corresponding predicted values for this configuration are not shown because of references 6, 8, 9, and 10 did not include gear- and flap-down data.

The major causes of the discrepancy between the flight-based and predicted  $C_{n\delta_a}$  are not known. However, three factors have been identified that account for a portion of the discrepancy: (1) the wind-tunnel data were limited and resulted in oversimplified approximations of the variation of  $C_{n\delta_a}$  with  $\delta_e$ , (2) more down elevator was required in flight for longitudinal trim than was predicted, and (3) large differences in Reynolds number existed between the predicted and flight data (table V). These three factors are illustrated in figure 25 for  $M \approx 0.95$ . The figure shows predicted data from references 6 and 8 for the XB-70-1 airplane and unpublished wind-tunnel data for the XB-70-2 configurations as well as a flight test point of the XB-70-1 airplane. Although the wind-tunnel data and the referenced data are for two different configurations, the correspondence is sufficiently close to provide a qualitative study of the tunnel and referenced data with flight. For this flight condition the difference between predicted and flight elevator trim settings was small (about  $1^\circ$ ) as compared with a difference of  $6^\circ$  or more at  $M = 1.2$  and at Mach numbers above 2.2. The comparisons shown in

figure 25 between the results from various wind-tunnel tests and flight test indicate a potential shift toward adverse yaw with increasing Reynolds number (Ames data) and decreasing angle of attack (Langley data). The flight data, it should be noted, were obtained at Reynolds numbers nearly an order of magnitude greater than those of the Ames tests. Also, a high sensitivity to small changes in Mach number at the critical Mach number of the figure is evident from a comparison of the Langley and Ames data for  $\alpha = 5^\circ$ . In general, however, the combined effects of the differences in elevator trim, Mach number, and angle of attack and the large difference in Reynolds number account for only a small part of the large discrepancy between the predicted and the flight data.

Another factor which may contribute significantly to the discrepancy between flight and predicted  $C_{n\delta_a}$  is the elastic deformation of the vertical tails due to inertial and aerodynamic loadings. The predictions consider only the static change in vertical-tail load due to change in flow field resulting from aileron inputs. The flight-determined derivatives, on the other hand, were obtained from dynamic measurements involving such factors as rolling accelerations and varying sideslip.

The predicted variations of  $C_{n\delta_r}$  in figure 24(a) correlate well with the flight-based trends. The effects of aeroelasticity on this derivative are estimated to be relatively small.

Flight-based roll-control effectiveness  $C_{l\delta_a}$  is shown in figure 24(b) to have approximately the same trend with Mach number as the predictions for the flexible aircraft. Most of the predicted data were based on nonsegmented elevons, with corrections applied for segmentation. Recently obtained unpublished model data for tests at  $M = 0.95$  and  $1.2$  at Reynolds numbers of  $9.4 \times 10^6$  and  $21.16 \times 10^6$  show an apparent decrease in  $C_{l\delta_a}$  with increasing Reynolds number.

The flight-based values for  $C_{l\delta_r}$  shown in figures 24(b) and 15(b) are negative in the subsonic and transonic regions for wing tips at  $0^\circ$  and  $25^\circ$ , whereas for most airplanes the value is normally positive. The negative value signifies a trailing-edge-left movement on the rudder (positive  $\delta_r$ ) produces a left-rolling-moment increment, which implies a strong interaction of the rudder pressure field on the wing. The predictions of references 6 and 8 indicate  $C_{l\delta_r}$  to be negligible; hence, the derivative was assumed to be zero, as shown in figure 24(b). The data of reference 9, however, show the rigid-model values for  $\delta_T = 0^\circ$  to be negative, which generally confirms flight data.

Figure 24(c) shows the predicted values for  $C_{y\delta_r}$  to be generally lower than determined from flight tests. Reliable estimates of  $C_{y\delta_a}$  could not be obtained from the flight data, so only the predicted trends are shown.

Stability derivatives. — The flight-based stability derivatives are compared with predictions in figure 26. There is relatively good agreement for some derivatives and large discrepancies in others.

The flight-determined derivatives, in general, are considered to be valid only for sideslip angles less than  $\pm 2^\circ$  because of a highly nonlinear trend in stability

characteristics beyond this range. Recent unpublished data for the XB-70-2 model obtained in the NASA Ames Research Center 11- by 11-foot wind tunnel for Mach numbers of 0.95 and 1.2,  $\delta_T = 30^\circ$ , and  $\alpha = 5^\circ$  revealed a sharp break in the variation of  $C_n$  with  $\beta$ , whereas  $C_l$  is only slightly affected. Figure 27 shows the wind-tunnel results for  $M = 1.2$ . Both the break and the difference in slope in the linear range are associated with the presence of the canard. Also, a variation in Reynolds number, which was accompanied by changes in dynamic pressure, affects the slopes but not the break points. Unpublished data obtained in the NASA Langley Research Center 7- by 10-foot wind tunnel indicate the break to be small or negligible at  $\alpha = 0^\circ$  and to increase rapidly with increasing angle of attack. The wind-tunnel data used by the manufacturer did not define the change in characteristics as clearly because of an insufficient number of sideslip test points.

The flight-based static directional-stability derivative  $C_{n\beta}$  is generally in good agreement with the predicted values (fig. 26(a)) except at subsonic conditions ( $\delta_T = 0^\circ$ ) where the flight-based values are higher. The general trend of the data for the different wing-tip positions indicates that deflecting the wing tips from  $0^\circ$  to  $25^\circ$  or from  $25^\circ$  to  $65^\circ$  did not significantly increase  $C_{n\beta}$ . Full tip deflection, however, was predicted to enhance substantially the directional stability at  $M = 1.4$ .

The variation of the flight-based effective dihedral parameter  $C_{l\beta}$  with Mach number in figure 26(a) shows the same trends as the predictions; however, the general level of the flight-based data suggests a possible overcorrection for aeroelastic effects. Each increase in tip deflection in figure 26(a) results in a significant reduction in dihedral effect. In the original design concept, neutral or slightly positive effective dihedral was intended. Later, after fabrication of the first aircraft was started, the effective dihedral with wing tips at  $65^\circ$  was found to be negative. The second aircraft, therefore, was constructed with  $5^\circ$  geometric dihedral in the outer wing panels to offset this trend. The first aircraft does not incorporate this feature and, as a result, exhibits adverse roll-off response characteristics with the tips at  $65^\circ$ . This tendency coupled with the adverse-aileron-yaw characteristics required careful coordination of controls to avoid pilot-induced oscillations in unaugmented flight.

The damping derivative  $C_{nr}$  (fig. 26(b)) generally proved to be much larger than predicted at Mach numbers greater than 1. The predicted values were calculated in the absence of dynamic model tests.

The flight-based values for the yawing-moment-due-to-roll derivative  $C_{np}$  (fig. 26(b)) are in fairly good agreement with the calculated values. This derivative has a significant effect on Dutch roll damping when the effective dihedral is high.

The damping-in-roll derivative  $C_{lp}$  is shown in figure 26(c) to be generally more negative than predicted. Large differences between flight and predictions are noted in the transonic region; however, the predictions in this region are generally unreliable.

The flight-based values for the derivative  $C_{lr}$  (fig. 26(c)) are more negative than predicted for  $25^\circ$  and  $65^\circ$  tip deflections in the lower supersonic region. Also, negative

rather than positive values (as predicted) were obtained in the subsonic region with tips at 0°. The more negative trend for the flight-based data tends to improve the spiral characteristics.

The flight-based values of  $C_{Y\beta}$  (fig. 26(d)) show a good correlation with the predictions for the flexible aircraft, considering the degree of uncertainty in these data.

Dutch roll dynamics.— The Dutch roll characteristics, as calculated from the flight-based data, are compared with predictions in figure 28 in terms of period and damping and in figure 29 in terms of amplitude ratios and phase angles. The flight-based and predicted periods in figure 28 correlate well for 0° and 25° tip deflections and show a fairly constant level of about 5 seconds. With the tips at 65°, the flight-based periods are longer than predicted, with the difference attributable in part to differences in  $C_{n\beta}$  and  $C_{l\beta}$ .

The damping characteristics in terms of the damping ratio (fig. 28) show moderately light damping ( $\zeta = 0.2$ ) with tips at 0°, light damping ( $\zeta = 0.1$ ) with tips at 25°, and light to moderately light damping with the tips at 65°, with damping increasing with Mach number. It is interesting to note that the damping with the tips at 65° is considerably higher than predicted, primarily as a result of underestimating the damping derivative  $C_{n_r}$  (fig. 26(b)). The pilots quickly noticed the difference between the damping of the actual aircraft and that observed on the XB-70 ground-based simulator when the predicted derivatives were used.

The  $\left|\frac{\varphi}{\beta}\right|$  ratios of the Dutch roll oscillations (fig. 29(a)) show the aircraft to have high oscillatory rolling characteristics for the 0° tip configuration. These characteristics reflect the high effective dihedral of this configuration (fig. 26(a)). Lowering the wing tips to 25° reduced the ratio significantly. The reduced roll oscillations in combination with the reduction of the roll-control effectiveness  $C_{l\delta_a}$  (due to deactivation of the two outboard segments) resulted in an improved roll response and was the basis for the pilot's decision to fly the airplane in the subsonic region with the tips at 25° instead of 0°.

With the tips at 65° the flight-based oscillatory roll characteristics are much higher than predicted. The ratio  $\left|\frac{\varphi}{\beta}\right|$  is governed mainly by the ratio  $\frac{C_{l\beta}}{C_{n\beta}}$  and, because  $C_{n\beta}$  showed generally good agreement with predictions, the correlation of flight-based  $\left|\frac{\varphi}{\beta}\right|$  with predictions is similar to that for  $C_{l\beta}$ . The negative dihedral with the tips at 65° is reflected in the phase angle  $\Phi_{\varphi\beta}$ . The maximum roll angle lags the maximum sideslip angle by about 160° when the effective dihedral is negative. When the effective dihedral is positive, the bank angle leads the sideslip angle by an angle of the order of 50° or less.

The  $\left|\frac{\psi}{\beta}\right|$  ratio of the Dutch roll oscillations (fig. 29(b)) is significantly less than 1.0 with the tips at 0° and generally near 1.0 with tips deflected. The heading change

about the body Z-axis during Dutch roll oscillations is not necessarily indicative of the amplitude of the sideslip. The phase angles, however, range between 170° to 180°.

The correlation of the flight-based values of  $\left| \frac{\psi}{\beta} \right|$  with predictions is reasonably good.

Spiral and roll stability.— The roll stability (roll convergence) of the airplane as calculated from the flight-based derivatives is shown in figure 30 to be more positive than predicted for  $\delta_T = 0^\circ$  and  $25^\circ$  and about the same as predicted for  $\delta_T = 65^\circ$ .

The spiral roots also were calculated from the flight-based derivatives and, although showing considerable scatter, appear to be generally higher than predicted for Mach numbers below approximately 2.0. Positive spiral stability (spiral convergence) is evident up to a Mach number of about 1.8, which compares favorably with the predicted Mach number of about 2.0.

## CONCLUSIONS

An evaluation of the unaugmented stability and control characteristics of the XB-70-1 airplane was made on the basis of data obtained during the first phase of the flight-test program. The evaluation showed that:

1. The airplane was characterized longitudinally by a fairly heavy damping ratio of the order of 0.5 at low subsonic speeds and a light damping ratio of the order of 0.1 at high supersonic speeds. The predicted characteristics tended generally to correspond with the flight results.

2. In the lateral-directional modes, the airplane was characterized by moderately light Dutch roll damping, with damping ratios of 0.2 or less throughout the Mach range. The damping was higher than predicted at supersonic conditions, primarily as a result of underestimating the variation of the yawing-moment coefficient due to yaw rate.

3. The neutral point was slightly more forward than predicted. For the  $25^\circ$  and  $65^\circ$  wing-tip configurations, the neutral point was approximately 30 percent of the mean aerodynamic chord, and 27 percent to 29 percent of the mean aerodynamic chord when the tips were up.

4. The airplane exhibited negative (adverse) values of the aileron-yaw parameter  $C_{n\delta_a}$  at Mach numbers above approximately 0.90, whereas proverse yaw values were predicted. Positive values were obtained at subsonic speeds, but the flight values were less than predicted. Although the major sources of the discrepancy have not been ascertained, contributing factors include differences between flight and predicted elevator trim settings, the sparsity of the wind-tunnel data, and, possibly, the large differences in Reynolds number between predicted and flight data.

5. Both the flight-measured and predicted effective dihedral were negative for the  $65^\circ$  wing-tip configuration, with flight showing a higher value. The predicted effects of elasticity appear to have been overestimated.

6. The negative effective dihedral in the supersonic region with wing tips at  $65^\circ$  and the unpredicted adverse aileron yaw made the airplane very susceptible to divergent pilot-induced oscillations.

7. The flight-determined derivatives indicated the airplane to be spirally stable at Mach numbers below approximately 1.8.

8. A significant reduction in directional stability was evident at sideslip angles beyond approximately  $2^\circ$ . Wind-tunnel studies showed this to be a canard-interference effect.

9. Comparisons of the flight results with rigid-model wind-tunnel data and the predictions for the flexible aircraft generally indicated that the aeroelastic effects were significant for the static pitch stability, pitch-control effectiveness, roll-control effectiveness, static directional stability, and effective dihedral derivatives.

Flight Research Center,  
National Aeronautics and Space Administration,  
Edwards, Calif., October 12, 1967,  
732-01-00-01-24.

## APPENDIX A

### DETERMINATION OF THE STABILITY AND CONTROL DERIVATIVES FROM FLIGHT DATA

This appendix considers limitations of the flight data and provides details of the analog-matching technique used.

#### Inadequacy of Data for Simplified Techniques

In many of the pullup and release maneuvers, the transient short-period oscillations were accompanied by elevator movements, whereas accurate determination of the derivatives by simplified techniques requires the controls to be fixed. Also in the subsonic region, the oscillations were heavily damped. As a result, the simplified techniques (ref. 4) for determining the longitudinal stability and control derivatives were not in general adequate. Also, the lack of pitch-acceleration sensors prevented a satisfactory determination of pitch-control effectiveness by the simplified methods. Accuracy of the angle-of-attack data was questioned because the  $\alpha$ -vane was mounted on a short nose boom and thus was subject to upwash effects. In addition, elasticity of the forebody of the fuselage affected the indicated reading.

The lateral-directional derivatives were determined mainly from release-from-sideslip maneuvers. In general, however, the lateral-directional controls were moving during these maneuvers. Also, the output from the  $\beta$ -vane was questionable because of its location on the short nose boom, and the transverse acceleration was noisy.

In view of these problems, the technique of analog matching was considered to be the most suitable method for determining the longitudinal and lateral-directional stability and control derivatives.

#### Analog Matching of the Flight Data

A high-speed repetitive operation (Rep-op) was used to match the flight time histories on the analog computer. The technique was a refinement of the method of reference 5 in that a precision recorder was used in addition to the Rep-op scope. Also, a smaller-scale overlay was used with the precision recorder.

The general procedure used to determine the derivatives was to adjust the derivatives of the mathematical (analog) model until a close match was obtained on the Rep-op scope. At this point, a record was taken on the precision recorder and compared with its overlay. If adjustments were required, the Rep-op scope was used to observe the direction and magnitude of response to additional adjustments in the derivatives. The process was repeated until an accurate match of the flight histories was obtained on the precision recorder. Although there was always some question regarding the accuracy of the flight time histories of angle of attack (in longitudinal maneuvers) and  $\beta$  (in lateral-directional maneuvers), the analog match of each of these two quantities was reasonably good for about half the maneuvers analyzed. The attitude parameters  $\theta$  and  $\varphi$  were found to be more reliable than  $\alpha$  and  $\beta$ , respectively.

The mathematical models incorporated in the analog for longitudinal and lateral-directional derivative matching are summarized in appendix B. The models were linearized, small-perturbation equations of a rigid airplane except that large changes in roll angles were permitted. The derivatives include the effects of aeroelasticity and power, since the equations do not contain terms for these effects.

Initially, control inputs were programed into the analog by using digital diode function generators (DDFG). However, because of the time span of the lateral-directional maneuvers being analyzed and the high repetitive speed of the analog, the DDFG would not reset to the same voltage and the break points programed into the DDFG would wander. To alleviate these problems, the control input signals were put on magnetic tape which was programed into the analog. The use of magnetic tape improved the operations; however, the wander problem was replaced by a noise problem which made the recordings hashy. The noise problem was caused by the low voltage output from the tape recorder which had to be amplified by a factor of 50 in order to drive the analog. The noise problem, although a nuisance, was tolerable.

## APPENDIX B

### MATHEMATICAL RELATIONS USED IN ANALYSIS OF FLIGHT DATA

#### Analog Matching For Derivative Determination

The equations used in the analog to determine the stability and control derivatives by analog matching of flight time histories are summarized in this appendix. Because the flight-time histories were given as indicated values (not corrected to the center of gravity), the output of the analog was expressed in terms of indicated values. In the absence of angular accelerometers, the perturbed Euler angles were important factors in the matching operations.

Longitudinal derivatives. – The following small-perturbation equations were used in the analysis of the pullup and release maneuvers:

$$\Delta a_n = \frac{\bar{q}_0 S}{mg} \left[ C_{N_\alpha} \Delta \alpha + C_{N_{\delta_e}} \Delta \delta_e + \left( C_{N_q} + C_{N_{\dot{\alpha}}} \right) \frac{\Delta q \bar{c}}{2V_0} \right]$$

$$\Delta \dot{\alpha} = \left[ \Delta q - \left( \frac{g}{V_0} \sin \theta_0 \right) \frac{\Delta \theta}{57.3} - \frac{g \Delta a_n}{V_0} \right]$$

$$\Delta \dot{q} = \frac{\bar{q}_0 S \bar{c}}{I_Y} \left[ C_{m_\alpha} \Delta \alpha + C_{m_{\delta_e}} \Delta \delta_e + \left( C_{m_q} + C_{m_{\dot{\alpha}}} \right) \frac{\Delta q \bar{c}}{2V_0} \right]$$

The rate of change of perturbed pitch attitude was based on the simplified transformation

$$\Delta \dot{\theta} \approx \Delta q$$

Perturbed values of  $\alpha$  and  $a_n$  were converted to indicated values, to correspond to flight time histories, by using the expressions

$$\Delta \alpha_i = \Delta \alpha - 57.3 \frac{x_\alpha}{V_0} \Delta q$$

$$\Delta a_{ni} = \Delta a_n + \frac{x_{a_n}}{g} \Delta \dot{q}$$

The following four outputs of the analog were used in matching the indicated flight time histories:

$$a_{n_i} = a_{n_{i_0}} + \Delta a_{n_i}$$

$$\alpha_i = \alpha_{i_0} + \Delta \alpha_i$$

$$q = 57.3(q_0 + \Delta q) \text{ deg/sec}$$

$$\theta = \theta_0 + 57.3 \int \Delta q dt$$

Lateral-directional derivatives. – The analysis of the release-from-sideslip maneuvers was based on the following three equations:

$$\Delta \dot{\beta} = \left[ \frac{g}{V_0} \sin(\varphi_0 + \Delta \varphi) - \Delta r + \frac{\alpha_0 \Delta p}{57.3} + \frac{\bar{q}_0 S}{m V_0} \left( C_{y_\beta} \Delta \beta + C_{y_{\delta_r}} \Delta \delta_r + C_{y_{\delta_a}} \Delta \delta_a \right) - \frac{g}{V_0} \sin \varphi_0 \right]$$

$$\Delta \dot{p} = \Delta \dot{r} \left( \frac{I_{XZ}}{I_X} \right) + \frac{\bar{q}_0 S b}{I_X} \left[ C_{l_\beta} \Delta \beta + C_{l_{\delta_r}} \Delta \delta_r + C_{l_{\delta_a}} \Delta \delta_a + \left( C_{l_p} \Delta p + C_{l_r} \Delta r \right) \frac{b}{2V_0} \right]$$

$$\Delta \dot{r} = \Delta \dot{p} \left( \frac{I_{XZ}}{I_Z} \right) + \frac{\bar{q}_0 S b}{I_Z} \left[ C_{n_\beta} \Delta \beta + C_{n_{\delta_r}} \Delta \delta_r + C_{n_{\delta_a}} \Delta \delta_a + \left( C_{n_p} \Delta p + C_{n_r} \Delta r \right) \frac{b}{2V_0} \right]$$

The rate of change of perturbed roll attitude was based on the following relation:

$$\Delta \dot{\varphi} = \left[ \Delta p + (r_0 + \Delta r) \frac{\theta_0}{57.3} \cos(\varphi_0 + \Delta \varphi) - \frac{r_0 \theta_0}{57.3} \cos \varphi_0 \right]$$

Perturbated values of  $\beta$  and  $a_t$  were converted to indicated values, to correspond to flight time histories, by using the expressions

$$\Delta \beta_i = \Delta \beta + 57.3 \left( \frac{x_\beta}{V_0} \Delta r - \frac{z_\beta}{V_0} \Delta p \right)$$

$$\Delta a_{t_i} = -\sin(\varphi_0 + \Delta \varphi) + \sin \varphi_0 + \frac{V_0}{g} \left( \Delta \dot{\beta} + \Delta r - \frac{\alpha_0}{57.3} \Delta p \right) + x_{at} \frac{\Delta \dot{r}}{g} - z_{at} \frac{\Delta \dot{p}}{g}$$

The following five outputs of the analog were used in matching the indicated flight time histories:

$$a_{t_i} = a_{t_{i_0}} + \Delta a_{t_i}$$

$$\beta_i = \beta_{i_0} + \Delta \beta_i$$

$$\varphi = \varphi_0 + \Delta \varphi$$

$$p = 57.3(p_0 + \Delta p) \text{ deg/sec}$$

$$r = 57.3(r_0 + \Delta r) \text{ deg/sec}$$

### Dynamic Characteristics

Longitudinal short-period characteristics were determined from the following relations:

$$\omega_n^2 = -\frac{57.3\bar{q}_0 S \bar{c}}{I_Y} \left\{ C_{m_\alpha} + \frac{\bar{q}_0 S \bar{c}}{2mV_0^2} \left[ (C_{m_q} + C_{m_{\dot{\alpha}}}) C_{N_\alpha} - C_{m_\alpha} C_{N_q} \right] \right\}$$

$$\zeta \omega_n = -\frac{\bar{q}_0 S \bar{c}^2}{4V_0 I_Y} (C_{m_q} + C_{m_{\dot{\alpha}}}) + \frac{57.3\bar{q}_0 S}{2mV_0} C_{N_\alpha}$$

$$\zeta = \frac{\zeta \omega_n}{\omega_n}$$

$$P = \frac{2\pi}{\omega_n \sqrt{1 - \zeta^2}}$$

The lateral-directional characteristics were determined by substituting the derivatives into the linearized lateral-directional equations of motion and solving for the Dutch roll, spiral, and roll-subsidence roots by using a digital program.

## REFERENCES

1. Mechtly, E. A.: The International System of Units - Physical Constants and Conversion Factors. NASA SP-7012, 1964.
2. Control Systems Group: Flight Control Systems, XB-70 Air Vehicle. Rep. No. NA-60-2, North American Aviation, Inc., Jan. 4, 1960.
3. Aero-Thermo Design, B-70 Division: Analysis of External Aerodynamic Effect of Inlet Operation on the XB-70 at Mach Numbers of 1.2 to 3.5 in the North American Aviation Trisonic Wind Tunnel and the Ames  $8 \times 7$  Supersonic Wind Tunnel. Rep. No. NA-62-575, North American Aviation, Inc., June 1, 1962.
4. Wolowicz, Chester H.: Considerations in the Determination of Stability and Control Derivatives and Dynamic Characteristics From Flight Data. AGARD Rep. 549-Part 1, 1966.
5. Rampy, John M.; and Berry, Donald T.: Determination of Stability Derivatives From Flight Test Data by Means of High Speed Repetitive Operation Analog Matching. FTC-TDR-64-8, Air Force Flight Test Center, May 1964.
6. Aerodynamics Group: Estimated Rigid and Flexible Aerodynamic Derivatives for XB-70 Air Vehicle No. 1. Rep. No. TFD-65-396, North American Aviation, Inc., June 21, 1965 (rev. Oct. 6, 1966).
7. Wykes, John H.; and Lawrence, Robert E.: Aerothermoelasticity - Some Recent Studies of the Impact on Stability and Control of Winged Aerospace Vehicles. Paper No. 64-489, AIAA, July 1964.
8. Aerodynamics Group: Aerodynamic Characteristics for Structural Analysis. XB-70 Air Vehicles #1 and 2. Vol. I. Rep. No. NA-64-973, North American Aviation, Inc., Oct. 1, 1964.
9. Aero-Thermo Design, B-70 Project Group: Analysis of Aerodynamic Characteristics of the .03-Scale XB-70 Airframe Model V at Mach Numbers of 0.23 to 3.5 in the Ames  $8 \times 7$  Supersonic Wind Tunnel, North American Low-Speed Wind Tunnel, North American Trisonic Wind Tunnel and Cornell 8-Foot Transonic Wind Tunnel. Rep. No. NA-61-43, North American Aviation, Inc., June 1, 1962.
10. Aero-Thermo Design, B-70 Project Group: Analysis of Aerodynamic Characteristics of the .03-Scale B-70 Airframe Model V at Mach Numbers of .2 to 3.5 in the Ames  $8 \times 7$ , Southern California Cooperative, and North American Low-Speed Wind Tunnel. Rep. No. NA-60-457-SST, North American Aviation, Inc., Apr. 13, 1960.

TABLE I. -- GEOMETRIC CHARACTERISTICS OF THE XB-70-1 AIRPLANE

## Wing --

Total area, includes 2482.34 ft <sup>2</sup> (230.62 m <sup>2</sup> ) covered by fuselage but not 33.53 ft <sup>2</sup> (3.12 m <sup>2</sup> ) of the wing ramp area, ft <sup>2</sup> (m <sup>2</sup> ) . . . . .	6297.8 (585.07)
Span, ft (m) . . . . .	105 (32)
Aspect ratio . . . . .	1.751
Taper ratio . . . . .	0.019
Dihedral angle, deg . . . . .	0
Root chord (wing station 0), ft (m) . . . . .	117.76 (35.89)
Tip chord (wing station 630 in. (16 m)), ft (m) . . . . .	2.19 (0.67)
Mean aerodynamic chord, in. (m) . . . . .	942.38 (23.94)
Wing station, in. (m) . . . . .	213.85 (5.43)
Fuselage station of 25-percent wing mean aerodynamic chord, in. (m) . . . . .	1621.22 (41.18)
Sweepback angle, deg:	
Leading edge . . . . .	65.57
25-percent element . . . . .	58.79
Trailing edge . . . . .	0
Airfoil section . . . . .	0.30 to 0.70 HEX (MOD)
Thickness, percent chord:	
Wing station --	
Root to 186 in. (4.72 m) . . . . .	2.0
460 in. to 630 in. (11.68 m to 16 m) . . . . .	2.5

## Folding wing tip (data for one tip only) --

Area, ft <sup>2</sup> (m <sup>2</sup> ) . . . . .	520.90 (48.39)
Span, ft (m) . . . . .	20.78 (6.33)
Aspect ratio . . . . .	0.829
Taper ratio . . . . .	0.046
Root chord, wing station 380.62 in. (9.67 m), ft (m) . . . . .	47.94 (14.61)
Tip chord, wing station 630 in. (16 m), ft (m) . . . . .	2.19 (0.67)
Mean aerodynamic chord (wing station 467.37 in. (11.87 m)), in. (m) . . . . .	384.25 (9.76)
Down deflection from inboard wing, deg . . . . .	0, 25, 65

## Elevons (data for one side) --

Total effective area aft of hinge line, includes 3.33 ft <sup>2</sup> (0.31 m <sup>2</sup> ) air gap at wing-tip fold line, ft <sup>2</sup> (m <sup>2</sup> ) . . . . .	197.7 (18.37)
Span, ft (m):	
Wing tips up . . . . .	20.44 (6.23)
Wing tips down . . . . .	13.98 (4.26)
Chord, in. (m) . . . . .	116 (2.95)
Sweepback of hinge line, deg . . . . .	0

## Canard --

Area, includes 150.31 ft <sup>2</sup> (13.96 m <sup>2</sup> ) covered by fuselage, ft <sup>2</sup> (m <sup>2</sup> ) . . . . .	415.59 (38.61)
Span, ft (m) . . . . .	28.81 (8.78)
Aspect ratio . . . . .	1.997
Taper ratio . . . . .	0.388
Dihedral angle, deg . . . . .	0
Root chord (canard station 0), ft (m) . . . . .	20.79 (6.34)

TABLE I - GEOMETRIC CHARACTERISTICS OF THE XB-70-1 AIRPLANE - Concluded

Tip chord (canard station 172.86 in. (4.39 m)), ft (m) . . . . .	8.06 (2.46)
Mean aerodynamic chord, in. (m): . . . . .	184.3 (4.68)
Canard station, in. (m) . . . . .	73.71 (1.87)
Fuselage station of 25-percent chord, in. (m) . . . . .	553.73 (14.06)
Sweepback angle, deg:	
Leading edge . . . . .	31.70
25-percent element . . . . .	21.64
Trailing edge . . . . .	-14.91
Airfoil section . . . . .	0.34 to 0.66 HEX (MOD)
Thickness chord ratio, percent:	
Root . . . . .	2.5
Tip . . . . .	2.52
Ratio of canard area to wing area . . . . .	0.066
Canard flap (data for one side) -	
Area (aft of hinge line), ft <sup>2</sup> (m <sup>2</sup> ) . . . . .	54.69 (5.08)
Inboard chord canard station 47.93 in. (1.22 m), ft (m) . . . . .	7.16 (2.18)
Outboard chord canard station 172.86 in. (4.39 m), ft (m) . . . . .	3.34 (1.02)
Ratio of flap area to canard semiarea . . . . .	0.263
Vertical tail (one of two) -	
Area (includes 8.96 ft <sup>2</sup> (0.83 m <sup>2</sup> ) blanketed area), ft <sup>2</sup> (m <sup>2</sup> ) . . . . .	233.96 (21.74)
Span, ft (m) . . . . .	15 (4.57)
Aspect ratio . . . . .	1
Root chord (vertical-tail station 0), ft (m): . . . . .	23.08 (7.03)
Tip chord (vertical-tail station 180 in. (4.57 m)), ft (m) . . . . .	6.92 (2.11)
Taper ratio . . . . .	0.30
Mean aerodynamic chord, in. (m): . . . . .	197.40 (5.01)
Vertical-tail station, in. (m) . . . . .	73.85 (1.88)
Fuselage station of 25-percent chord . . . . .	2188.50 (55.59)
Sweepback angle, deg:	
Leading edge . . . . .	51.77
25-percent element . . . . .	45
Trailing edge . . . . .	10.89
Airfoil section . . . . .	0.30 to 0.70 HEX (MOD)
Thickness chord ratio, percent:	
Root . . . . .	3.75
Tip . . . . .	2.50
Cant angle, deg . . . . .	0
Ratio of vertical tail to wing area . . . . .	0.037
Rudder -	
Area, includes 8.66 ft <sup>2</sup> (0.81 m <sup>2</sup> ) blanketed area, ft <sup>2</sup> (m <sup>2</sup> ) . . . . .	191.11 (17.76)
Span, ft (m) . . . . .	15.00 (4.57)
Root chord, vertical-tail station 0, ft (m) . . . . .	9.16 (2.79)
Tip chord, vertical-tail station 180 in. (4.57 m), ft (m) . . . . .	6.92 (2.11)
Sweepback of hinge line . . . . .	-45.0
Ratio of rudder area to vertical-tail area . . . . .	0.82
Fuselage (includes canopy) -	
Length, ft (m) . . . . .	185.75 (56.62)
Maximum depth (fuselage station 878 in. (22.30 m)), in. (m) . . . . .	106.92 (2.72)
Maximum breadth (fuselage station 855 in. (21.72 m)), in. (m) . . . . .	100 (2.54)
Side area, ft <sup>2</sup> (m <sup>2</sup> ) . . . . .	939.72 (87.30)
Planform area, ft <sup>2</sup> (m <sup>2</sup> ) . . . . .	1184.78 (110.07)

TABLE II. - XB-70 INSTRUMENTATION PERTINENT TO STABILITY AND CONTROL INVESTIGATION

Parameter	Sensor location			Accuracy, percent full range	Transducer range	Sampling rate, per sec
	X, fuselage station, in. (m)	Y, buttock plane, in. (m)	Z, water plane, in. (m)			
Central air-data system altitude (coarse)	80 (2.03)	0 (0)	14 (0.36)	2.0	-1,000 to 100,000 ft (-305 to 30,480 m)	4
Central air-data system altitude (fine)	80 (2.03)	0 (0)	14 (.36)	1.0	5,000 ft/rev (152.4 m/rev)	40
Central air-data system Mach number (coarse)	80 (2.03)	0 (0)	14 (.36)	2.0	0.5 to 3.2	4
Central air-data system Mach number (fine)	80 (2.03)	0 (0)	14 (.36)	2.0	0.3 M/rev	40
Angle of attack	92 (2.34)	6 (0.15)	20 (.51)	.8	-10° to 30°	20
Angle of sideslip	121 (3.07)	0 (0)	13 (.33)	.8	±20°	20
Pitch attitude	1415 (35.94)	16 (.41)	-64 (-1.63)	2.0	-10° to 40°	20
Bank attitude	1415 (35.94)	16 (.41)	-64 (-1.63)	2.0	±45°	20
Pitch rate	1404 (35.66)	16 (.41)	-64 (-1.63)	2.0	±10 deg/sec	4
Roll rate	1404 (35.66)	16 (.41)	-64 (-1.63)	2.0	±100 deg/sec	4
Yaw rate	1404 (35.66)	16 (.41)	-64 (-1.63)	2.0	±10 deg/sec	4
Normal acceleration	1485 (37.72)	11 (.28)	-71 (-1.80)	2.0	±2g	20
Transverse acceleration	1486 (37.74)	0 (0)	-37 (-.94)	2.0	±1g	20
Left-hand wing-tip position	-----	-- -----	-----	2.0	0° to 65°	4
Right-hand wing-tip position	-----	-- -----	-----	2.0	0° to 65°	4
Left-hand canard position	-----	-- -----	-----	2.0	0° to 6°	20
Left-hand vertical-stabilizer position	-----	-- -----	-----	1.0	±12°	20
Right-hand vertical-stabilizer position	-----	-- -----	-----	1.0	±12°	20
Position of individual elevon segment	-----	-- -----	-----	1.2	±30°	20

TABLE III. - XB-70-1 LONGITUDINAL BASIC FLIGHT DATA

Test point	$\delta T$ , deg	M	$h_p$ , feet (meters)	Weight, lb (kg)	Center of gravity, percent $\bar{c}$	$\alpha_{trim}$ , deg	$\delta_{trim}$ , deg	$I_y$ , slug-ft <sup>2</sup> (kg-m <sup>2</sup> )
1*	0	0.49	10.2×10 <sup>3</sup>	0.398×10 <sup>6</sup>	21.1	7.0	10.3	20.7×10 <sup>6</sup>
2*	0	.49	(3.11)	(.1800)	21.2	6.8	10.2	(28.0×10 <sup>6</sup> )
3	0	.60	(3.38)	.425	21.9	6.3	3.3	(27.9)
4	0	.61	(5.79)	.429	21.9	8.2	21.1	(28.6)
5	0	.79	(7.62)	.380	21.8	5.5	.2	(28.7)
6	0	1.03	(10.39)	.358	22.6	4.2	2.8	(26.0)
7	0	1.11	(10.76)	.343	23.1	4.2	6.8	(23.4)
8	25	.80	(3.17)	.475	21.8	4.4	8.0	(23.0)
9	25	.80	(3.29)	.474	21.7	4.2	8.0	(29.2)
10	25	.95	(7.62)	.352	20.8	3.6	4.6	(29.2)
11	25	.95	(10.79)	.383	21.1	5.8	2.0	(24.6)
12	25	1.20	(12.65)	.311	21.4	5.1	17.3	(23.4)
13	25	1.40	(12.44)	.361	19.7	4.4	4.8	(22.9)
14	25	1.40	(12.56)	.360	19.7	4.2	4.8	(23.7)
15	65	1.61	(13.72)	.369	19.8	3.6	5.2	(23.7)
16	65	1.79	(16.52)	.312	22.0	4.5	5.9	(25.3)
17	65	1.81	(13.72)	.400	21.6	3.5	6.0	(22.8)
18	65	2.11	(16.70)	.364	20.7	4.0	6.1	(28.4)
19	65	2.12	(15.24)	.391	21.2	4.0	3.1	(26.7)
20	65	2.24	(17.56)	.343	20.0	4.7	5.9	(27.4)
21	65	2.33	(16.67)	.413	20.8	4.4	-1.1	(25.7)
22	65	2.51	(18.35)	.381	21.9	4.1	3.3	(28.4)
23	65	2.56	(19.72)	.331	23.9	5.0	5.7	(27.1)
							6.9	(23.0)

\*Gear and flaps down.

TABLE IV. - XB-70-1 LATERAL-DIRECTIONAL BASIC FLIGHT DATA

Test point	$\delta T$ , deg	M	$h_p$ , feet (meters)	Weight, lb (kg)	Center of gravity, percent $\bar{c}$	$\alpha_{trim}$ , deg	$\delta_{trim}$ , deg	$I_X$ , slug-ft <sup>2</sup> (kg-m <sup>2</sup> )	$I_Z$ , slug-ft <sup>2</sup> (kg-m <sup>2</sup> )	$I_{XZ}$ , slug-ft <sup>2</sup> (kg-m <sup>2</sup> )
1*	0	0.51	15.4×10 <sup>3</sup> (4.69×10 <sup>3</sup> )	0.319×10 <sup>6</sup> (0.1446×10 <sup>6</sup> )	22.1	5.5	10.4	1.50×10 <sup>6</sup> (2.03×10 <sup>6</sup> )	17.9×10 <sup>6</sup> (24.2×10 <sup>6</sup> )	-0.62×10 <sup>6</sup> (-0.84×10 <sup>6</sup> )
2	0	.61	19.8 (6.04)	.443 (.2009)	19.8	8.6	0	2.16 (2.92)	23.3 (31.6)	-.93 (-1.26)
3	0	.79	25.0 (7.62)	.378 (.1715)	21.8	5.2	2.5	1.98 (2.68)	22.0 (29.8)	-.78 (-1.06)
4	0	.95	35.0 (10.67)	.380 (.1724)	22.5	4.8	1.1	1.46 (1.97)	18.6 (25.2)	-.775 (-1.05)
5	0	1.07	35.3 (10.76)	.344 (.1560)	24.0	3.6	7.9	1.35 (1.83)	18.2 (24.7)	-.708 (-.959)
6	25	.80	10.1 (3.08)	.302 (.1370)	23.2	1.9	6.2	1.34 (1.82)	16.8 (22.8)	-.59 (-.798)
7	25	.95	25.7 (7.83)	.348 (.1579)	20.3	3.7	4.5	1.57 (2.12)	19.8 (26.7)	-.73 (-.98)
8	25	1.20	40.0 (12.19)	.393 (.1783)	20.0	4.3	3.8	1.95 (2.53)	22.3 (30.2)	-.85 (-1.15)
9	65	1.41	42.3 (12.89)	.377 (.1710)	19.7	4.2	7.1	1.66 (2.25)	20.4 (27.5)	-.781 (-1.06)
10	65	1.64	44.5 (13.56)	.365 (.1656)	20.5	3.3	6.8	1.66 (2.25)	20.1 (27.2)	-.743 (-1.01)
11	65	1.84	49.4 (15.06)	.350 (.1587)	21.1	3.4	3.7	1.52 (2.06)	18.2 (24.7)	-.748 (-1.01)
12	65	2.10	49.1 (14.97)	.383 (.1737)	20.3	4.2	4.9	1.83 (2.48)	21.4 (29.0)	-.800 (-1.08)
13	65	2.35	55.5 (16.92)	.390 (.1769)	21.9	4.4	4.7	1.88 (2.54)	22.4 (30.2)	-.881 (-1.19)

\* Gear and flaps down.

TABLE V. – COMPARISON OF FLIGHT AND  
WIND-TUNNEL REYNOLDS NUMBERS

M	Condition	$h_p$ , ft (m)	$N_{Re}$
0.23	Flight Wind tunnel	Sea level -----	$129 \times 10^6$ 3.88
.80	Flight Flight Wind tunnel	15,000 (4,572) 30,000 (9,144) -----	291 175 3.55 to 14.93
.95	Flight Flight Wind tunnel Wind tunnel Wind tunnel	25,000 (7,620) 35,000 (10,668) ----- ----- -----	250 200 3.83 to 5.48 9.41 21.16
1.20	Flight Flight Wind tunnel Wind tunnel Wind tunnel Wind tunnel	35,000 (10,668) 45,000 (13,716) ----- ----- ----- -----	227 142 4.10 to 5.76 9.41 18.2 21.16
2.00	Flight Flight Wind tunnel	45,000 (13,716) 60,000 (18,288) -----	237 115.5 24.0
2.50	Flight Flight Wind tunnel	50,000 (15,240) 60,000 (18,288) -----	233 144 3.0 to 7.5
3.00	Flight Wind tunnel Wind tunnel	70,000 (21,336) ----- -----	107.5 2.0 to 8.0 27.0

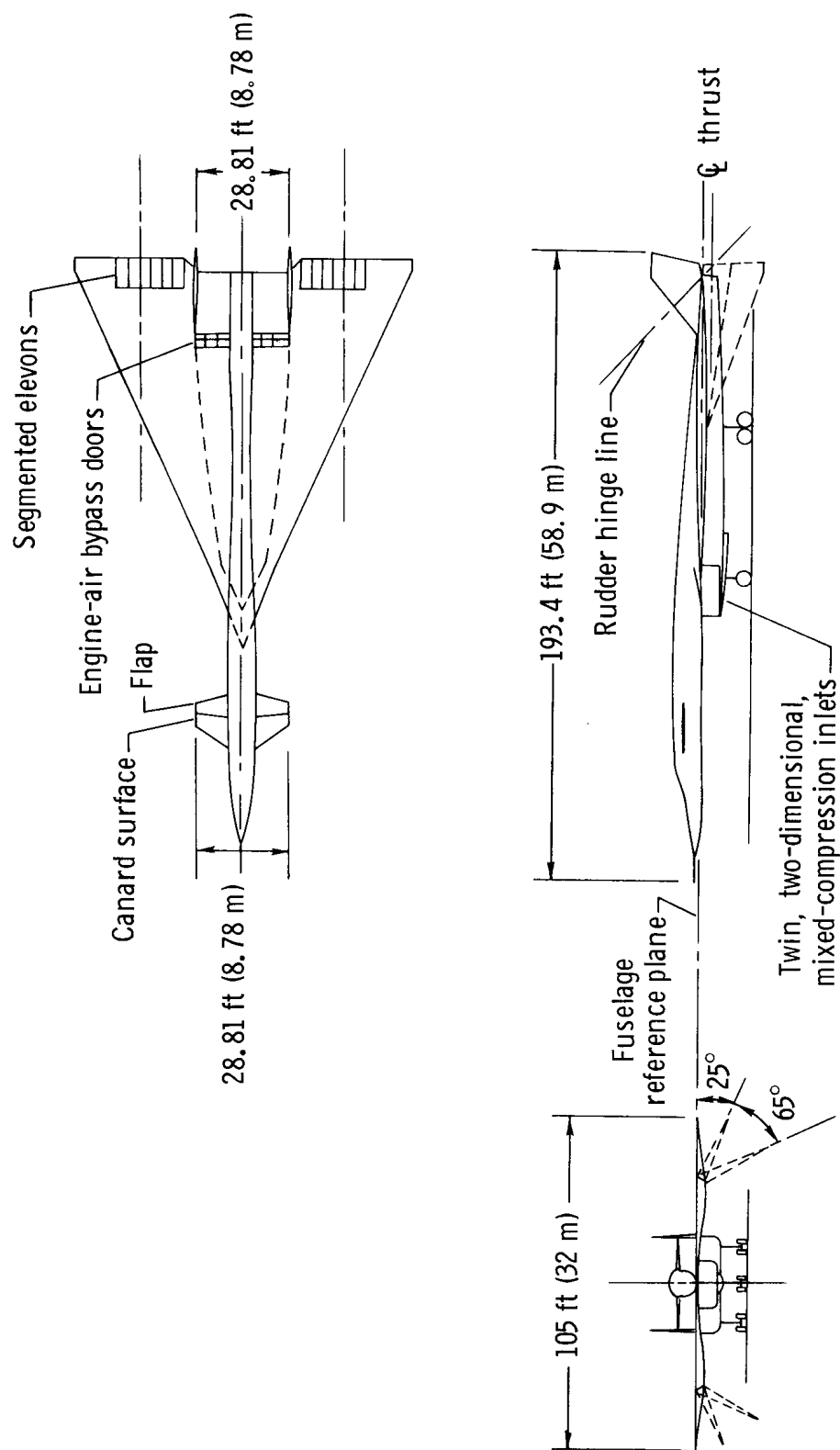


Figure 1. — XB-70-1 airplane.

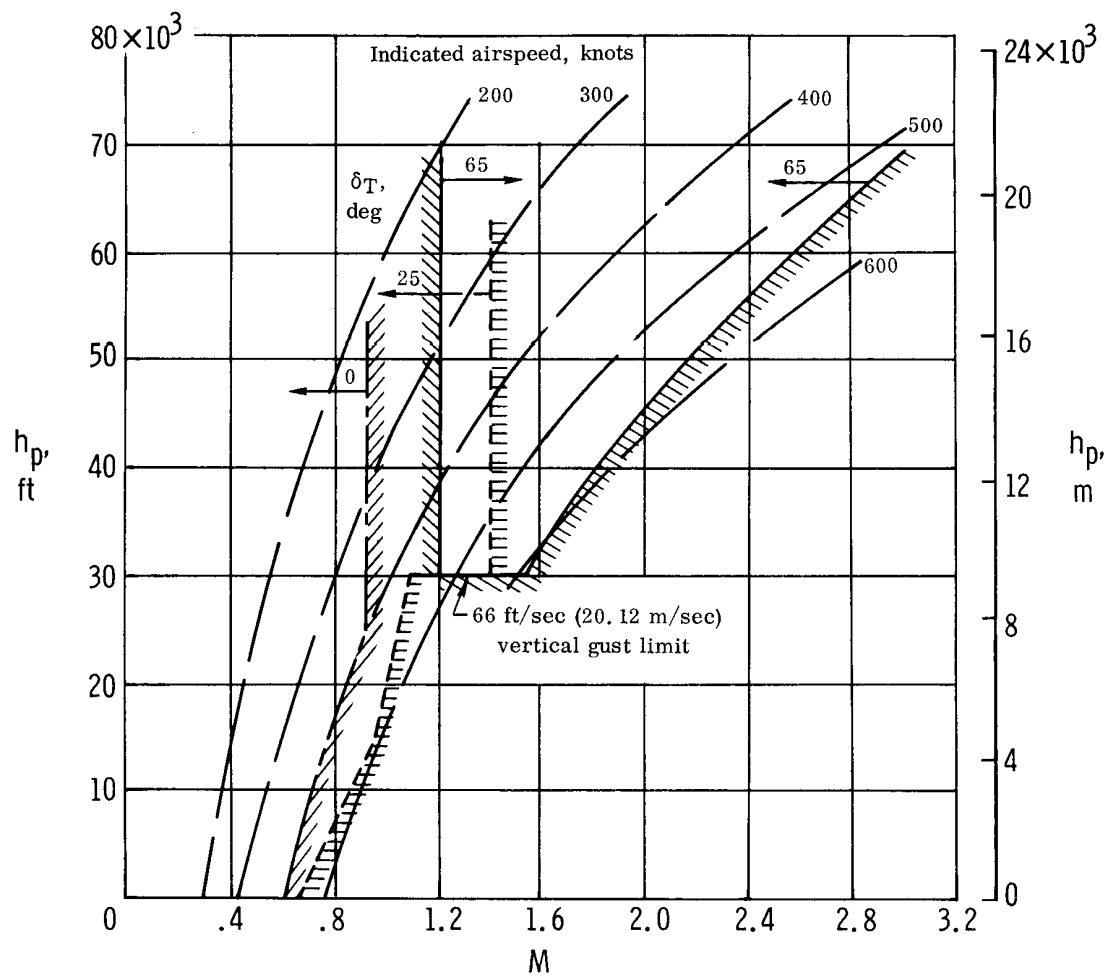


Figure 2.— Operational limits of the three wing-tip configurations of the XB-70-1.

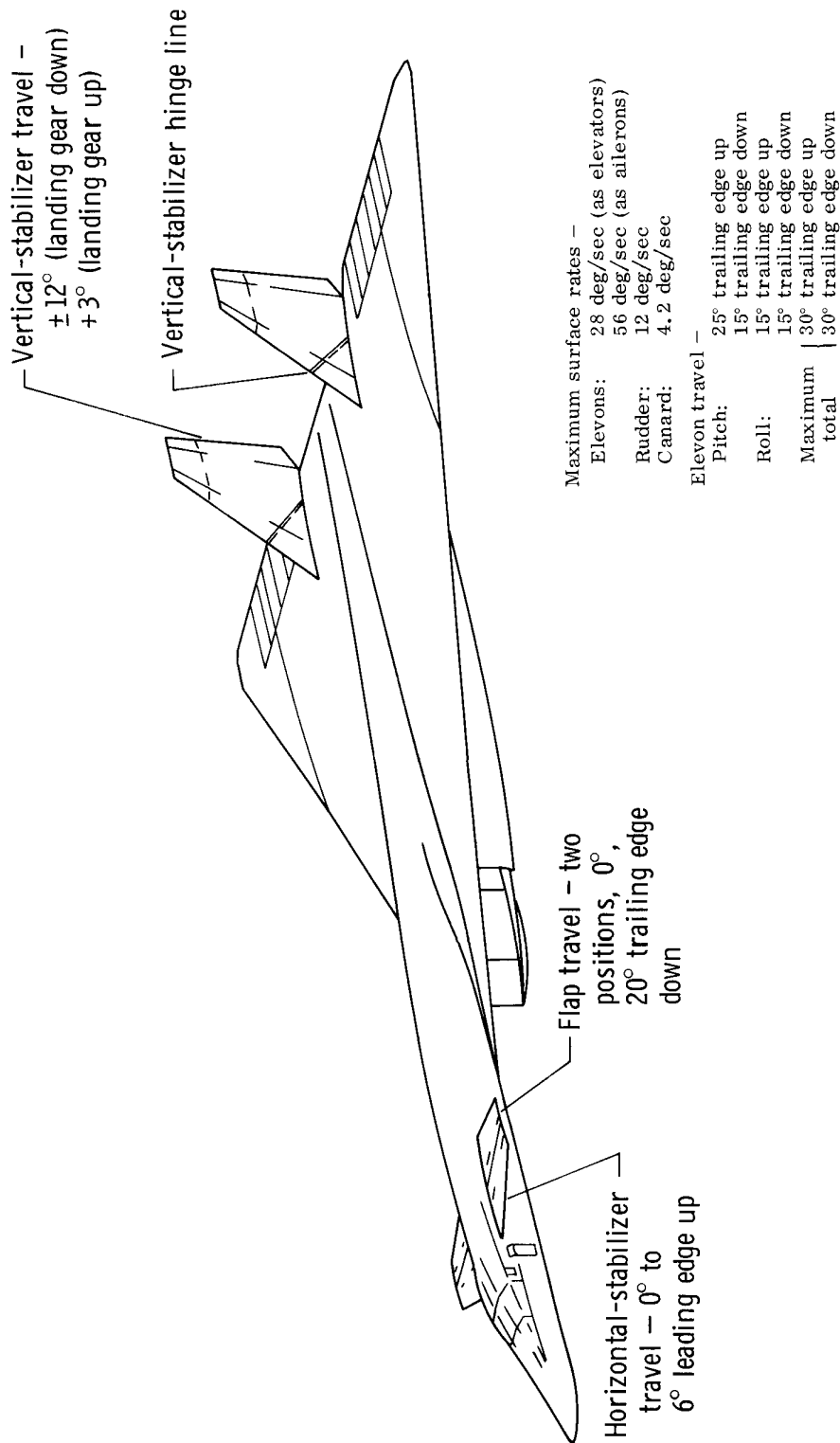


Figure 3. - XB-70-1 control-surface movements.

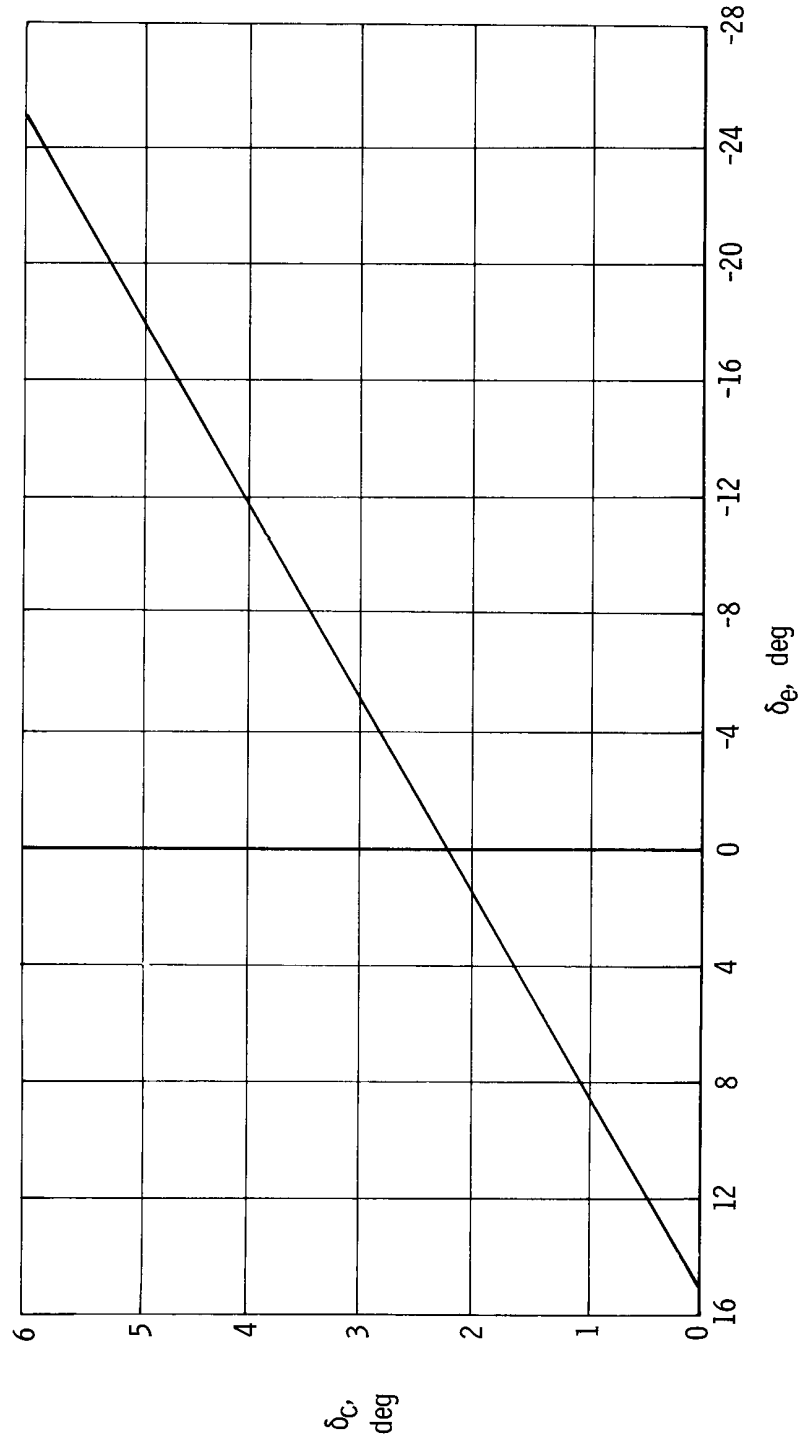


Figure 4. — Variation of XB-70-1 canard deflection with elevon deflection.  $\delta_c = 2.25^\circ - 0.15\delta_e$ .

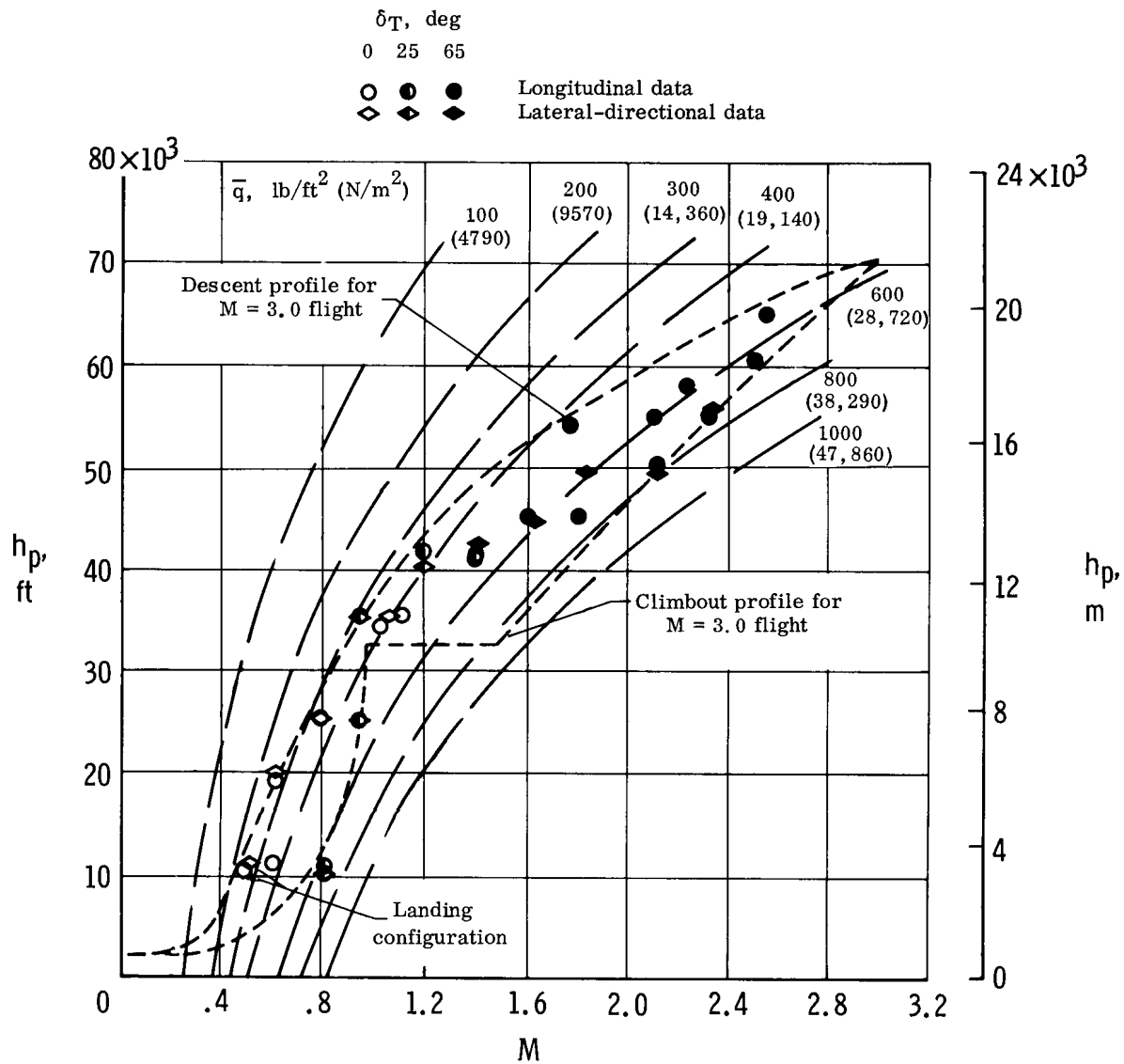


Figure 5.—XB-70-1 stability and control data points. (See tables III and IV for flight conditions.)

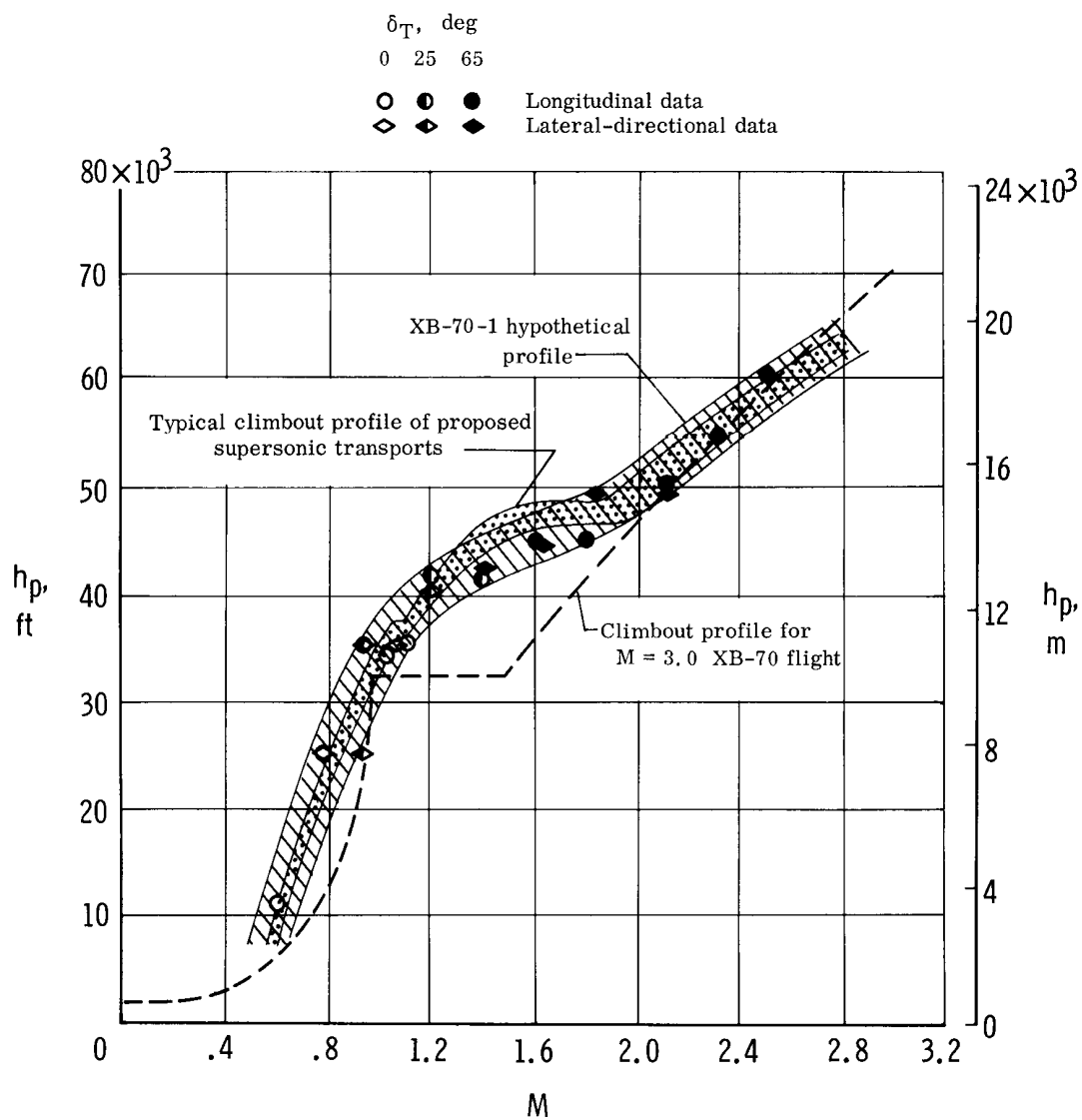


Figure 6.— Comparison of typical climbout profile of proposed supersonic transports with hypothetical climbout profile and flight data of the XB-70-1.

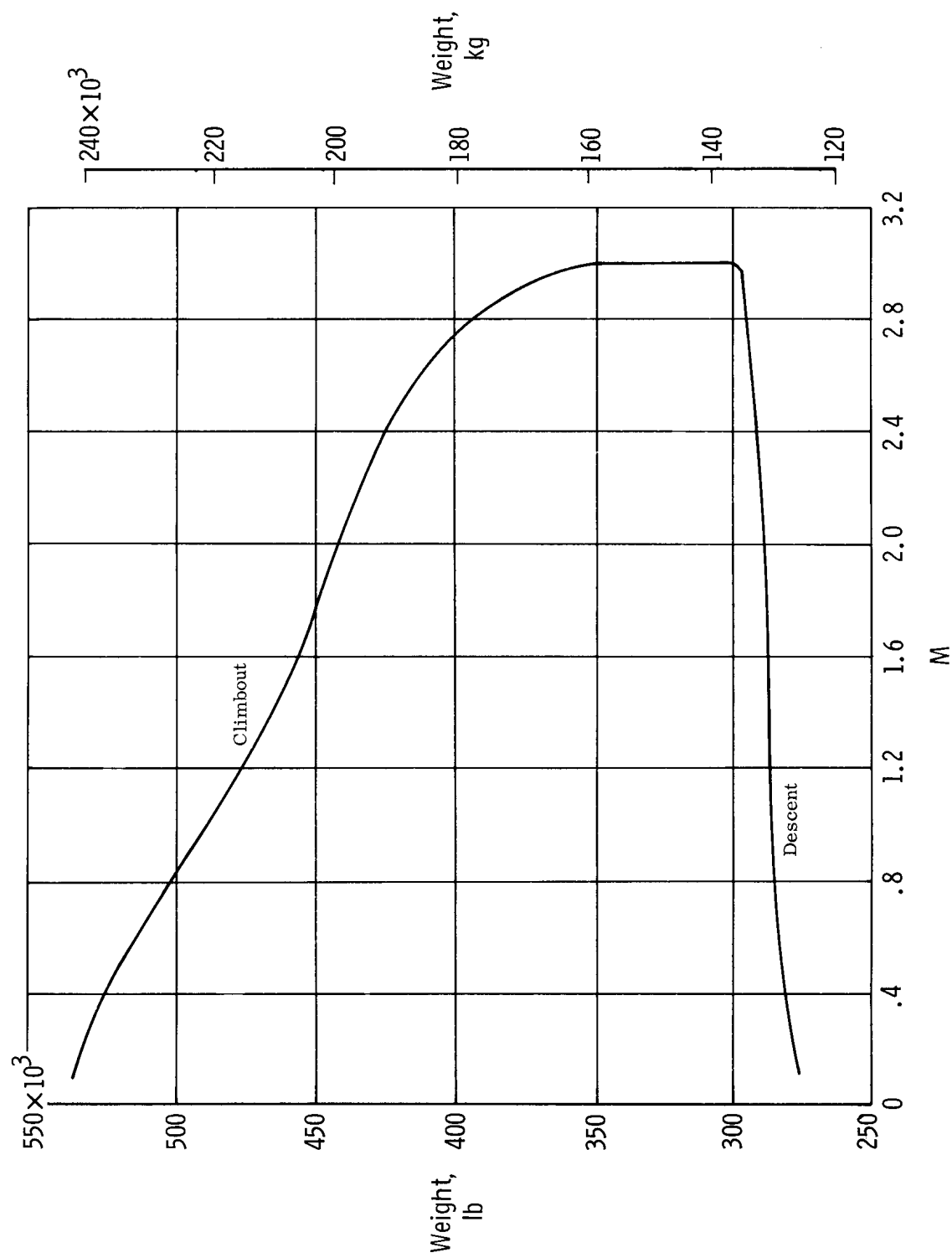


Figure 7. — Variation of XB-70-2 weight with Mach number during  $M = 3.0$  flight.

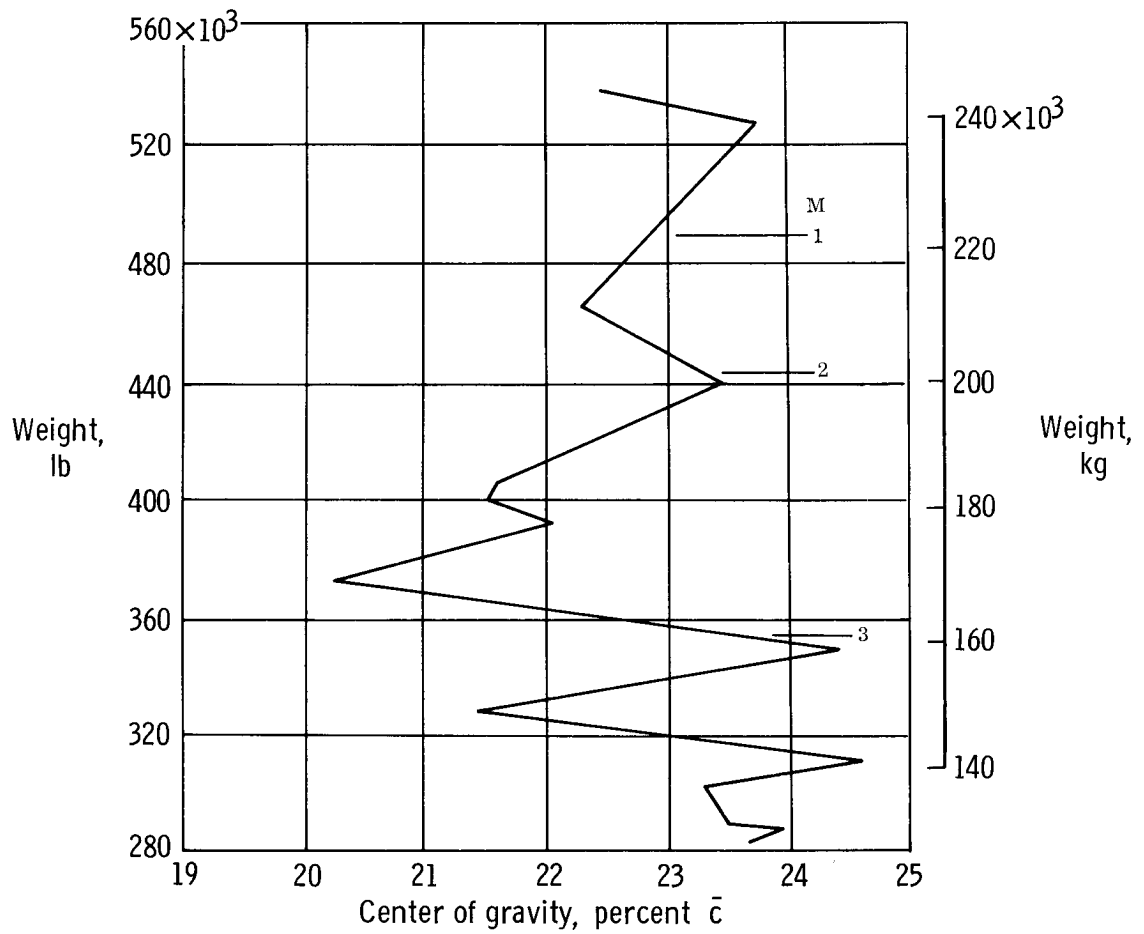


Figure 8. — Variation of center of gravity of XB-70-2 with weight during Mach 3.0 flight.

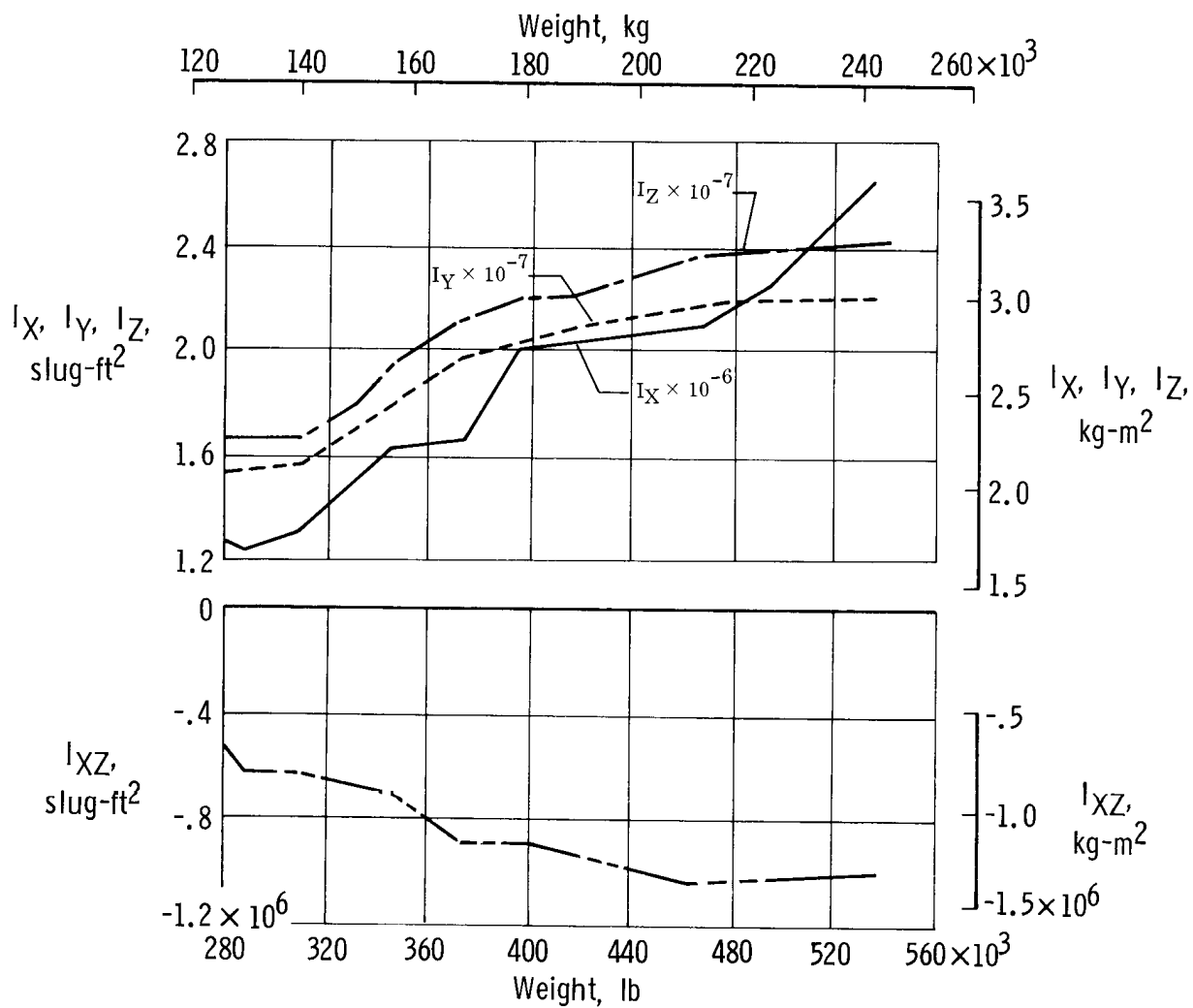
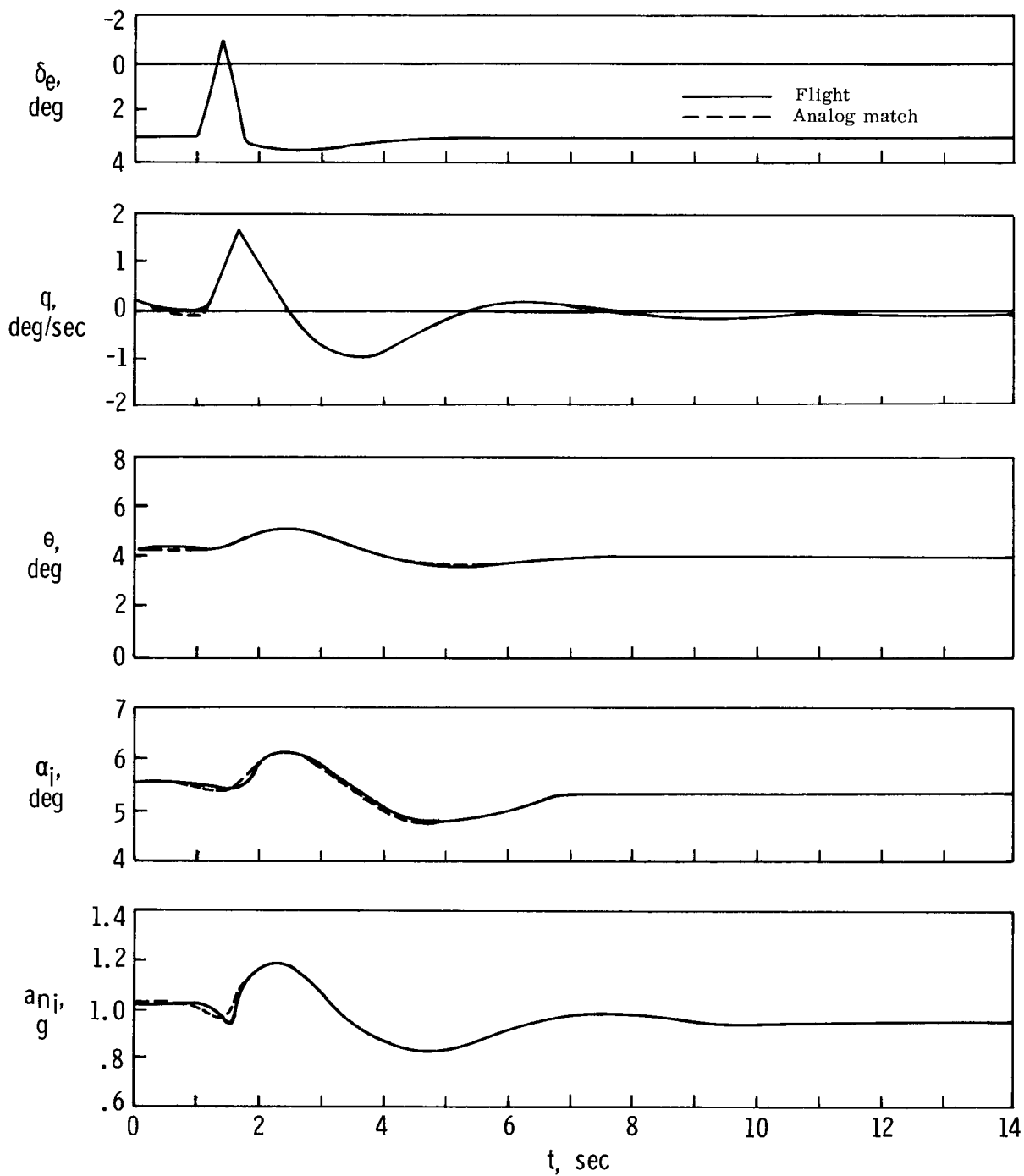
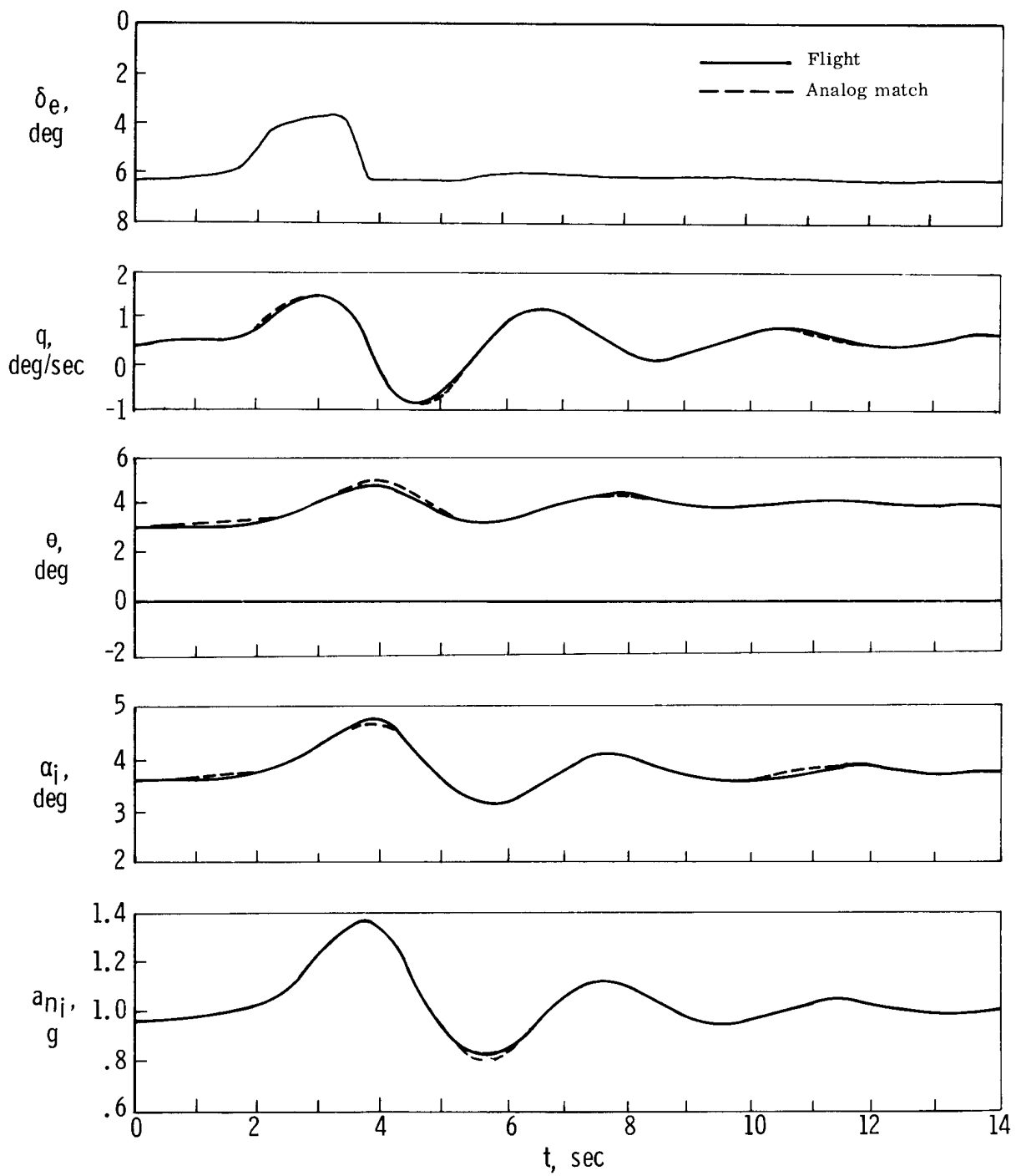


Figure 9. — Variation of moments and product of inertia of XB-70-2 with gross weight during Mach 3.0 flight.



(a)  $M = 0.79$ ,  $h_p = 25,000$  ft (7,620 m),  $\delta_T = 0^\circ$ .

Figure 10.— Typical analog matches of pull-up and release maneuvers.



(b)  $M = 1.81$ ,  $h_p = 45,000$  ft (13,720 m),  $\delta_T = 65^\circ$ .

Figure 10.— Concluded.

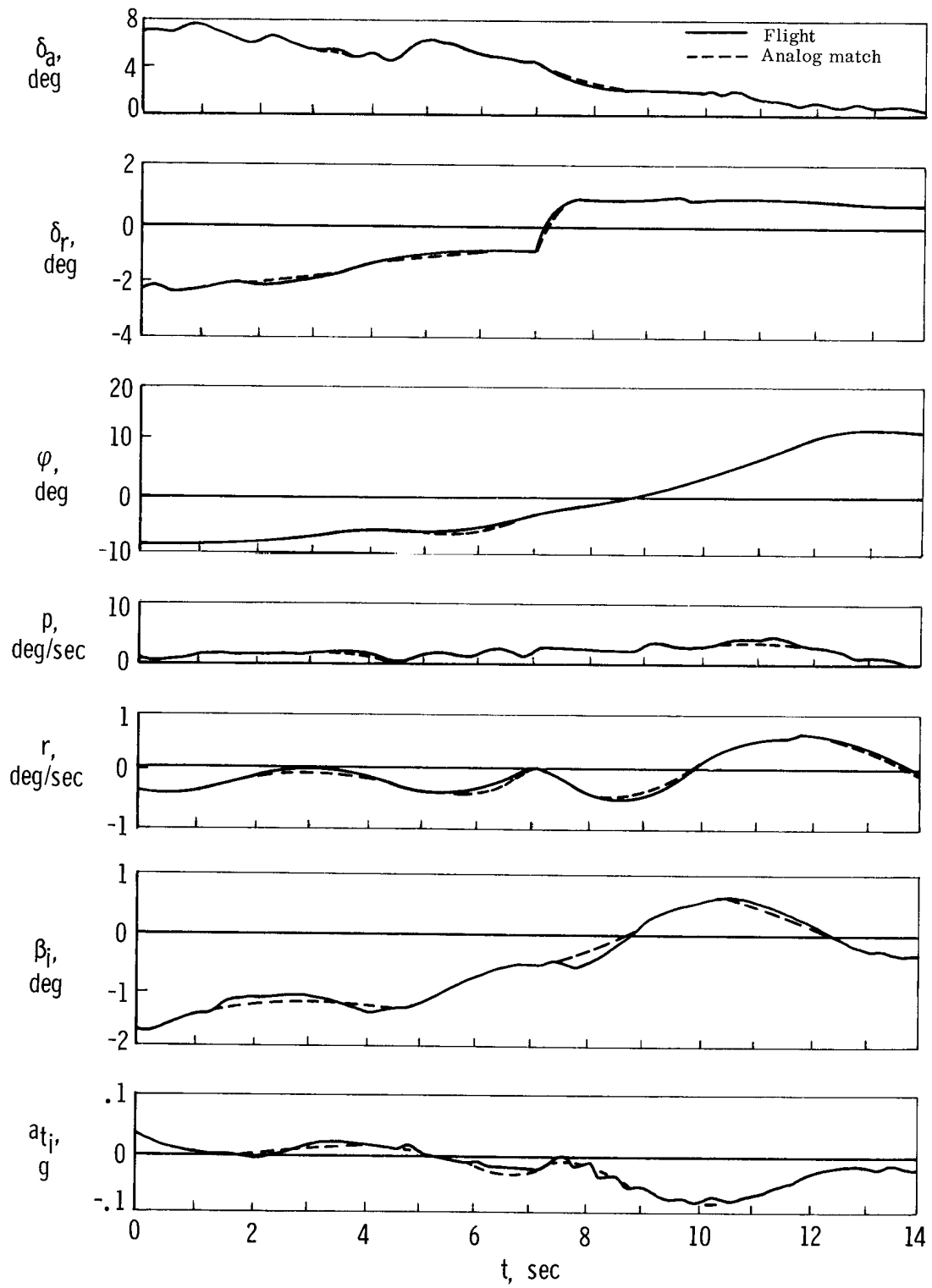


Figure 11.—Analog match of a well-conditioned release-from-sideslip maneuver.  $M = 1.84$ ;  $h_p = 49,400$  ft (15,060 m);  $\delta_T = 65^\circ$ .

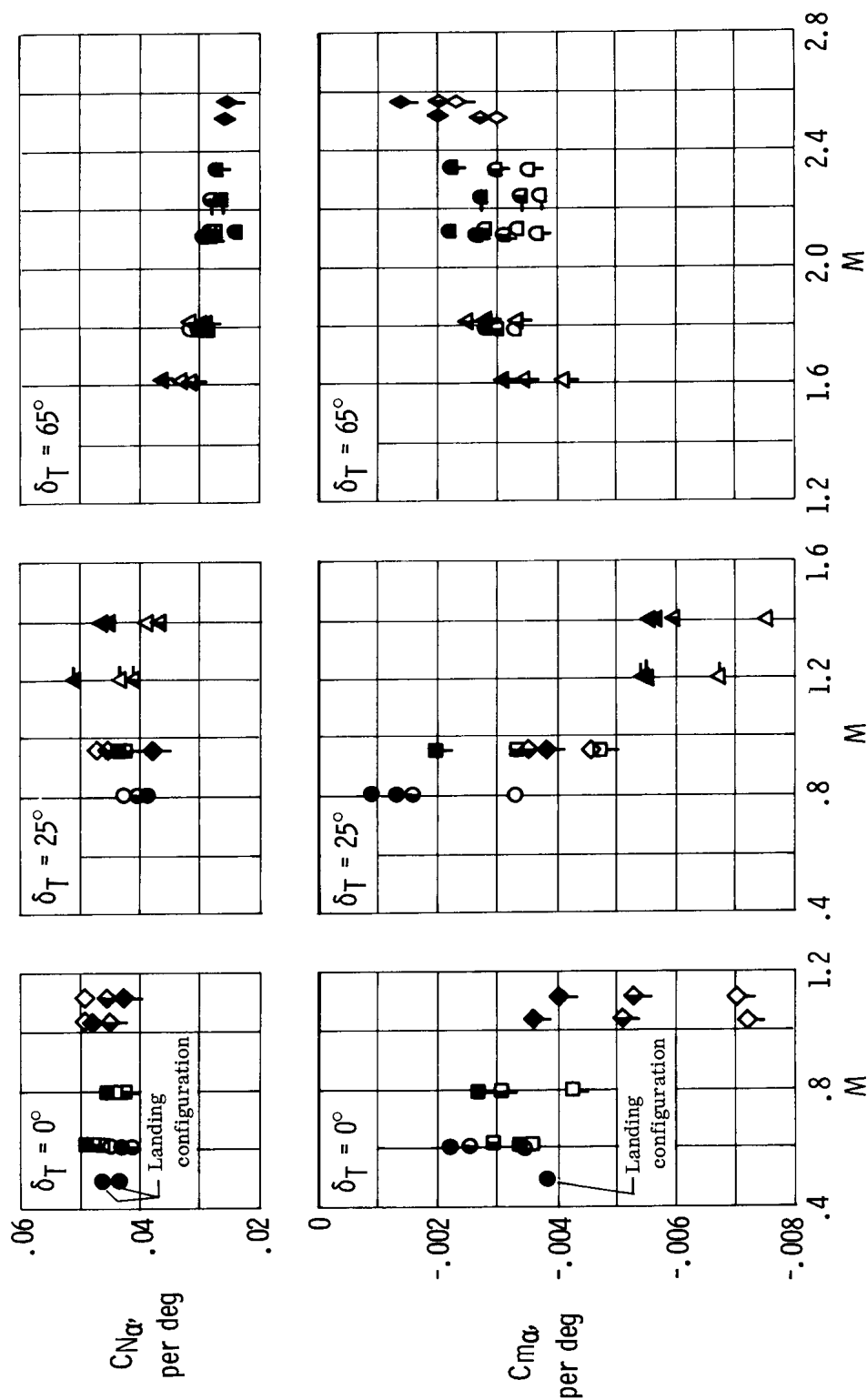
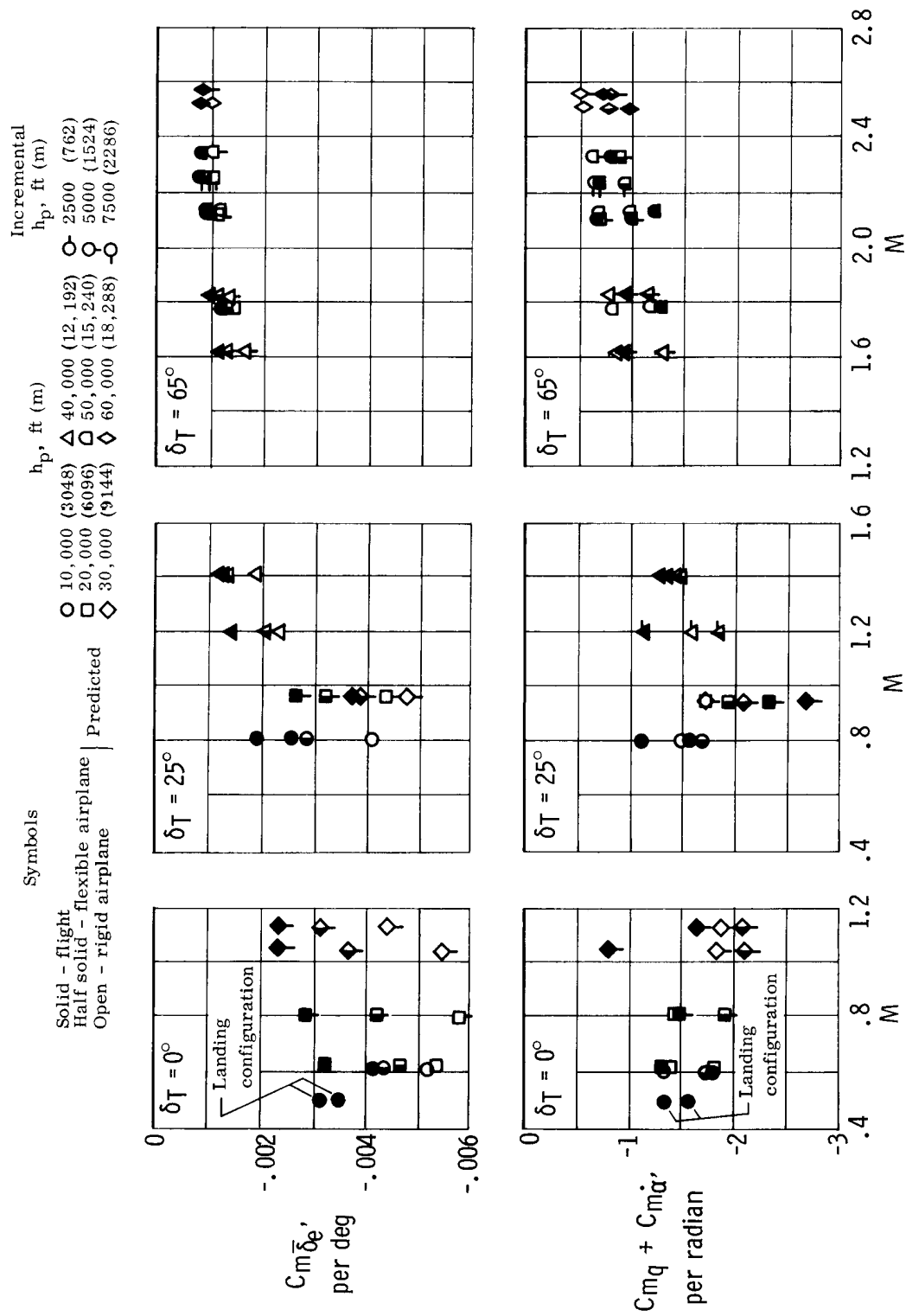


Figure 12. - Comparison of XB-70-1 flight-determined and predicted longitudinal derivatives. Weight and center of gravity for individual data points listed in table III.



(b)  $C_m \ddot{\delta}_e$ ,  $(C_{mq} + C_m \ddot{\alpha})$ .

Figure 12. — Concluded.

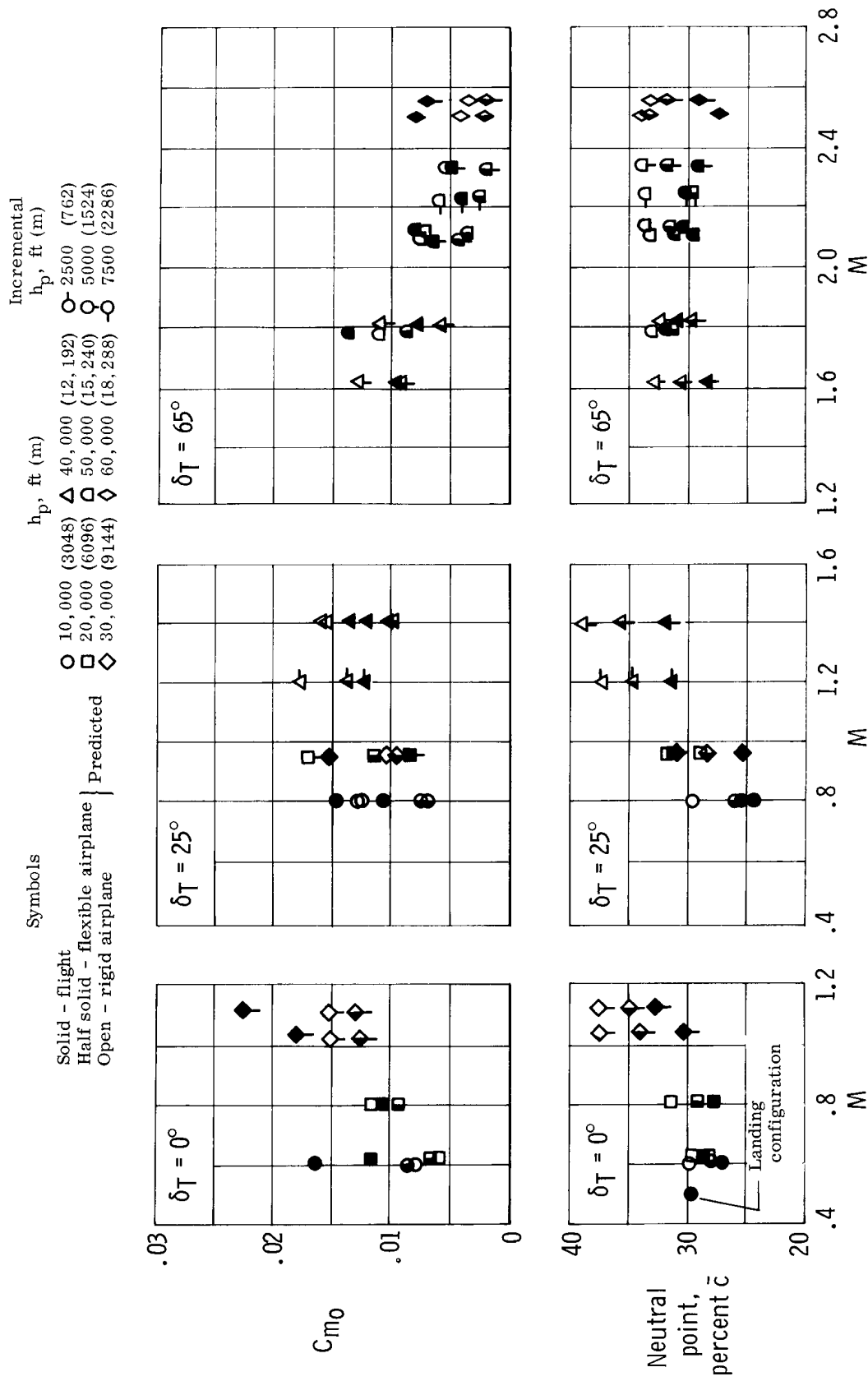


Figure 13. - Comparison of XB-70-1 flight-determined and predicted pitching-moment coefficient at zero lift ( $\delta_c = \delta_e = 0$ ) and neutral point. Weight and center of gravity for individual data points listed in table III.

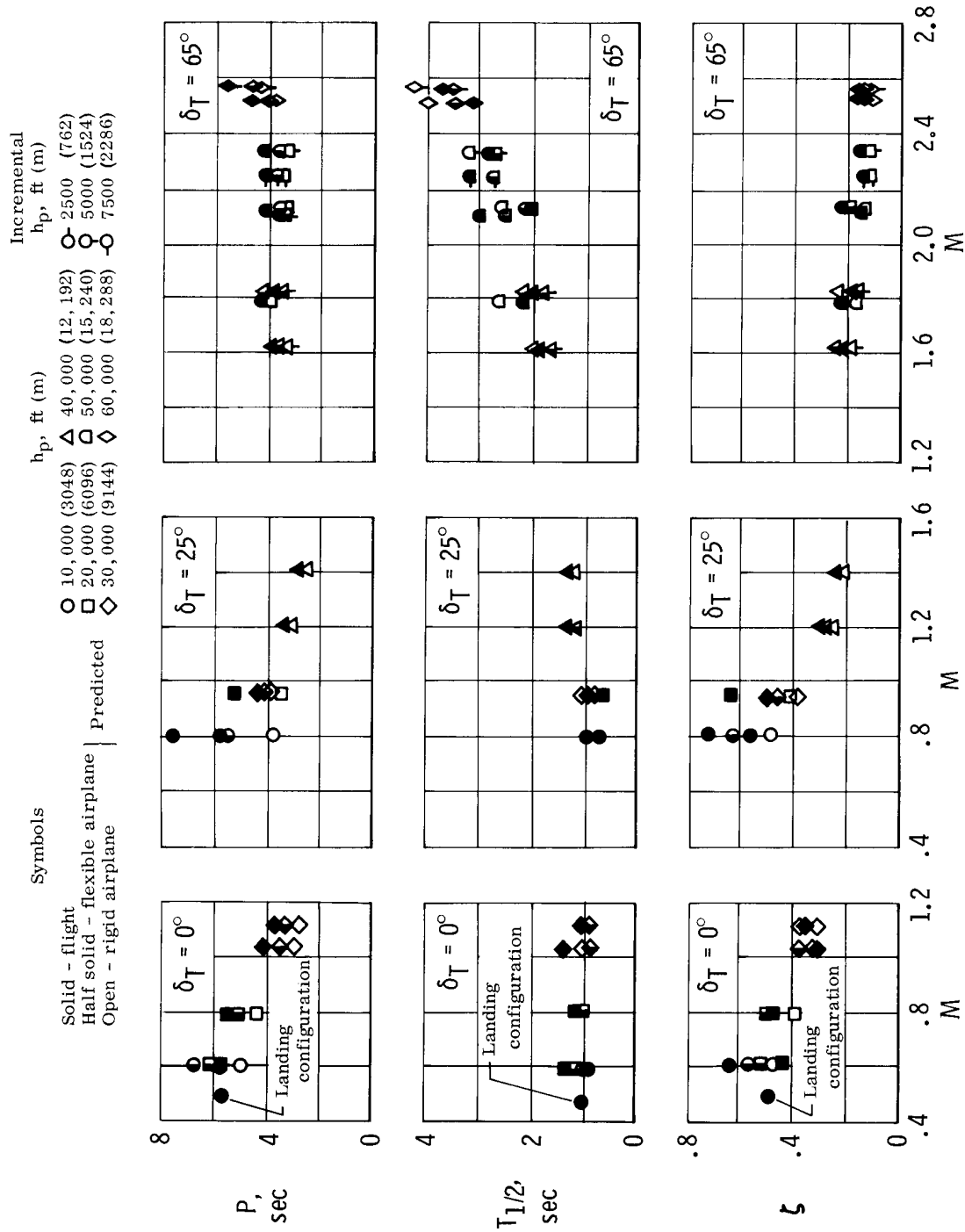


Figure 14.— Comparison of XB-70-1 flight-determined and predicted longitudinal short period and damping. Weight and center of gravity for individual data points listed in table III.

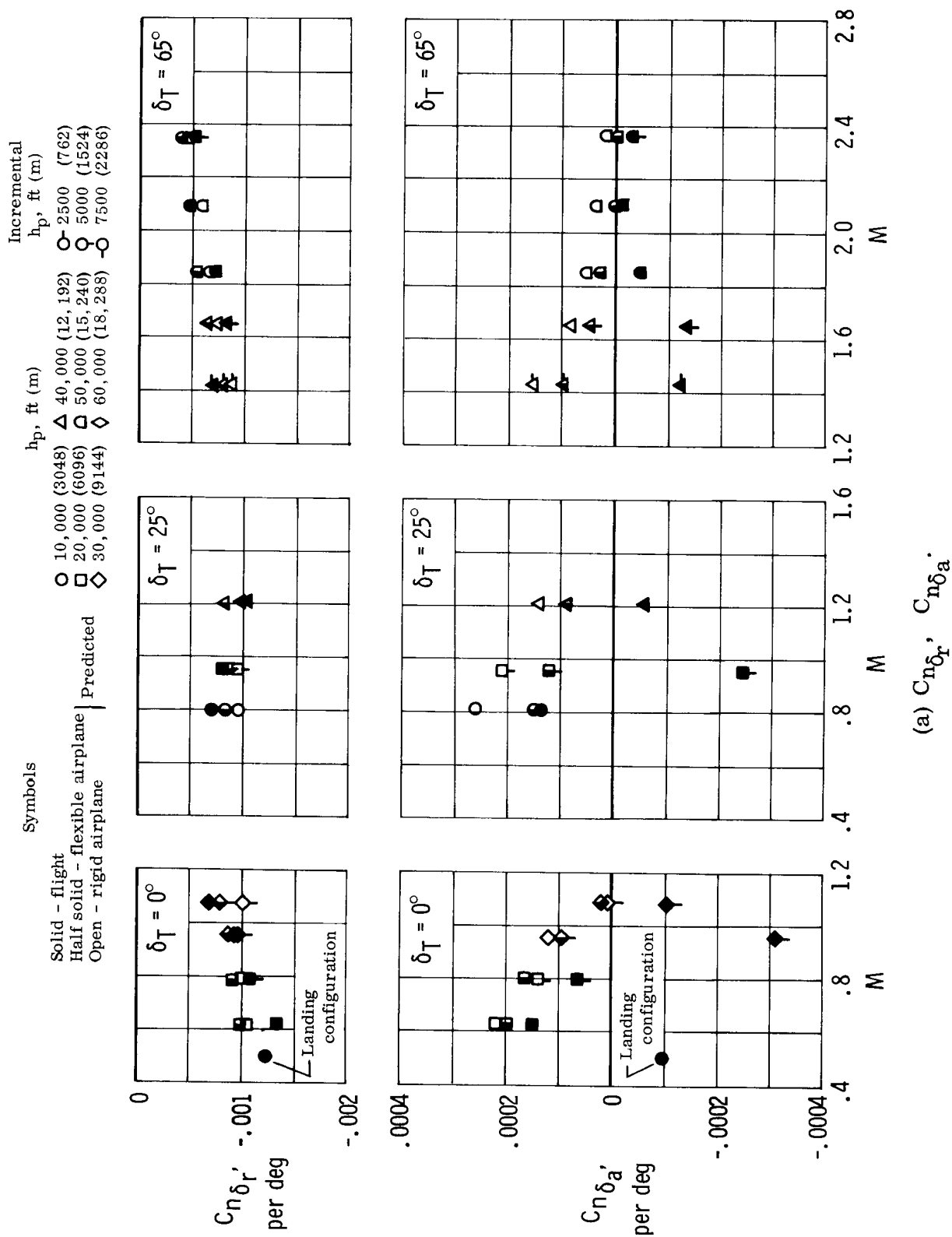
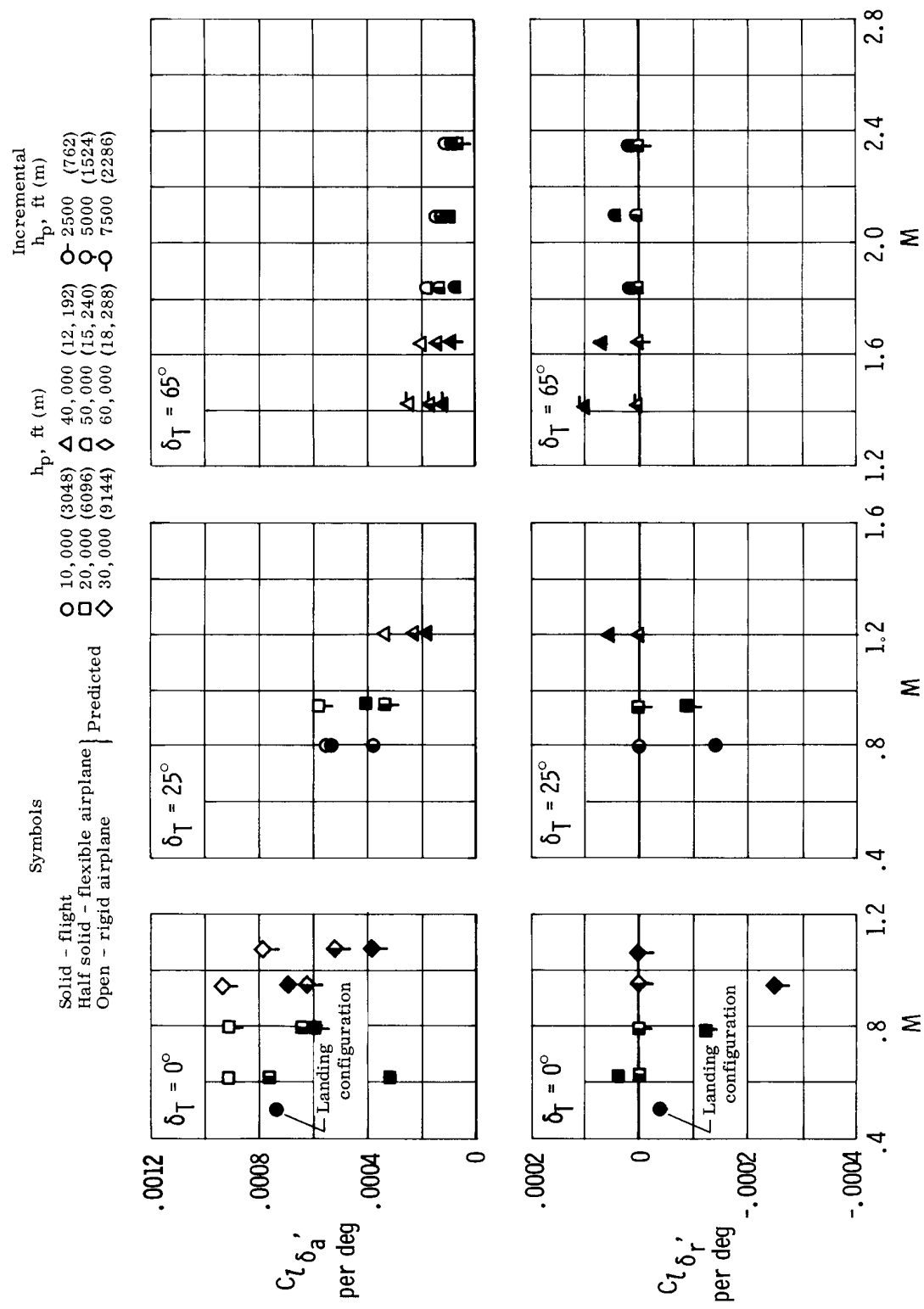


Figure 15. -- Comparison of XB-70-1 flight-determined and predicted lateral-directional control derivatives. (See table IV for weight and center of gravity for individual data points.)



(b)  $C_{l\delta_a}$ ,  $C_{l\delta_r}$

Figure 15. - Continued.

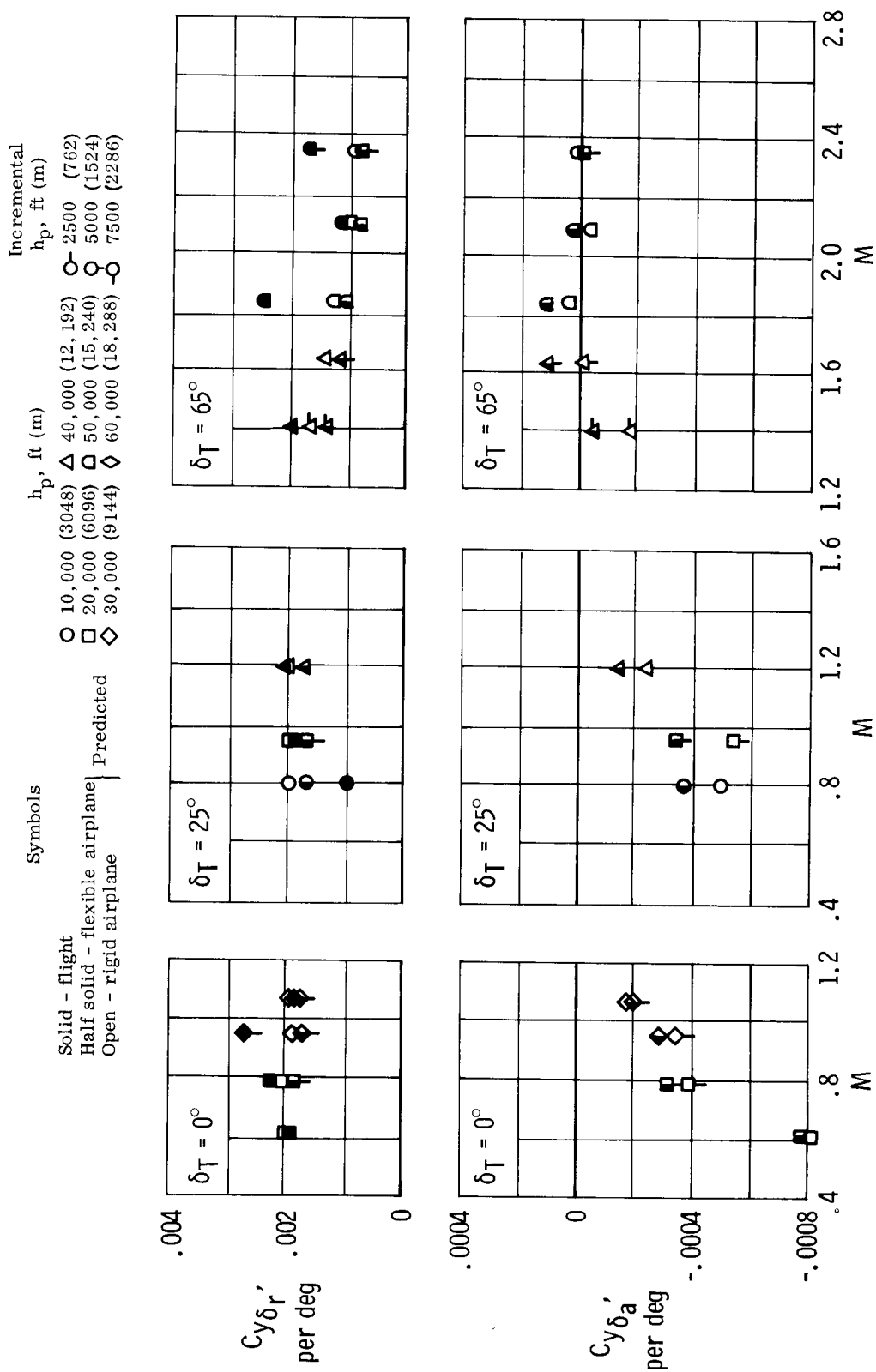
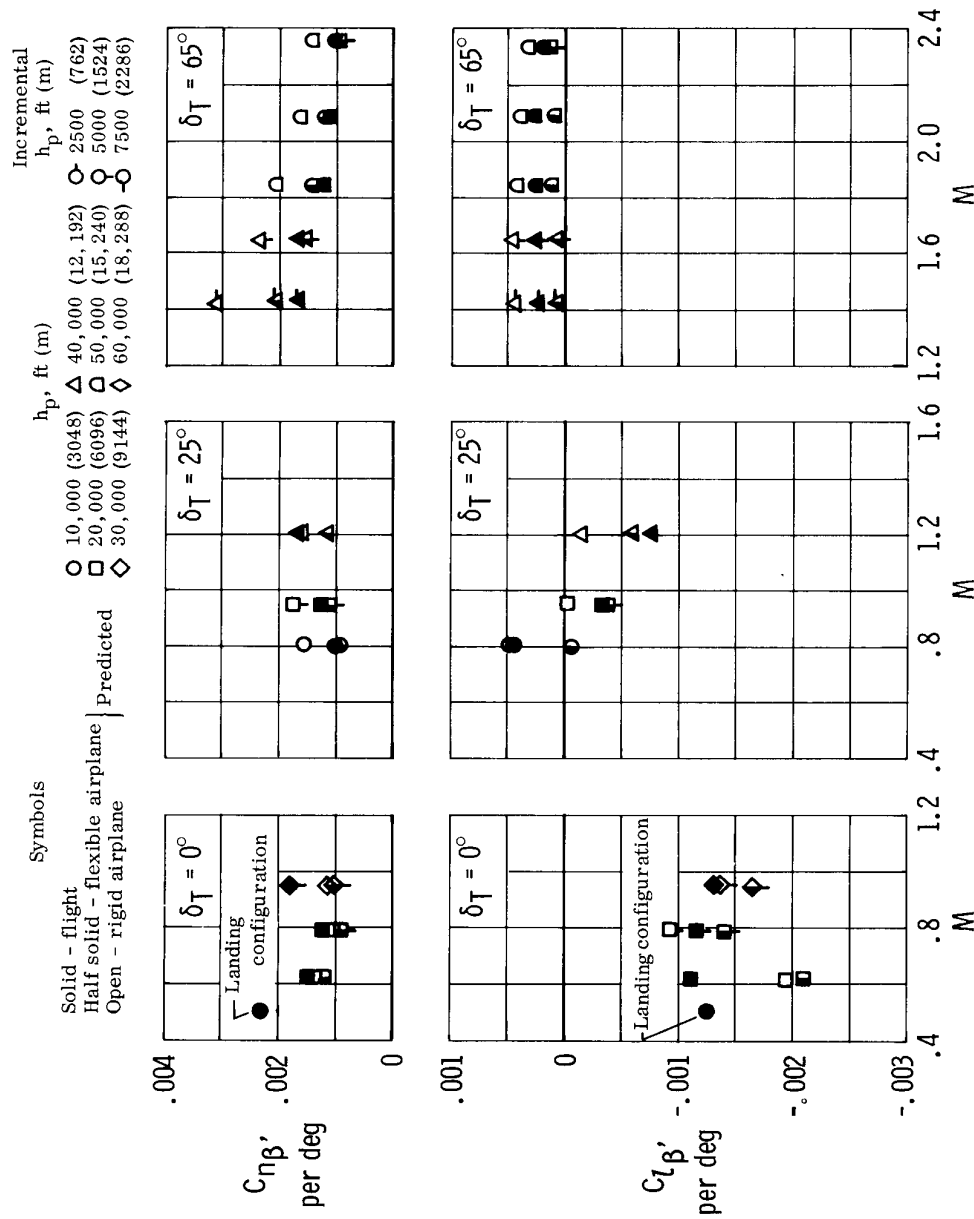


Figure 15. - Concluded.



(a)  $C_{n\beta}$ ,  $C_{l\beta}$ .

Figure 16. - Comparison of XB-70-1 flight-determined and predicted lateral-directional stability derivatives. (See table IV for weight and center of gravity of individual data points.)

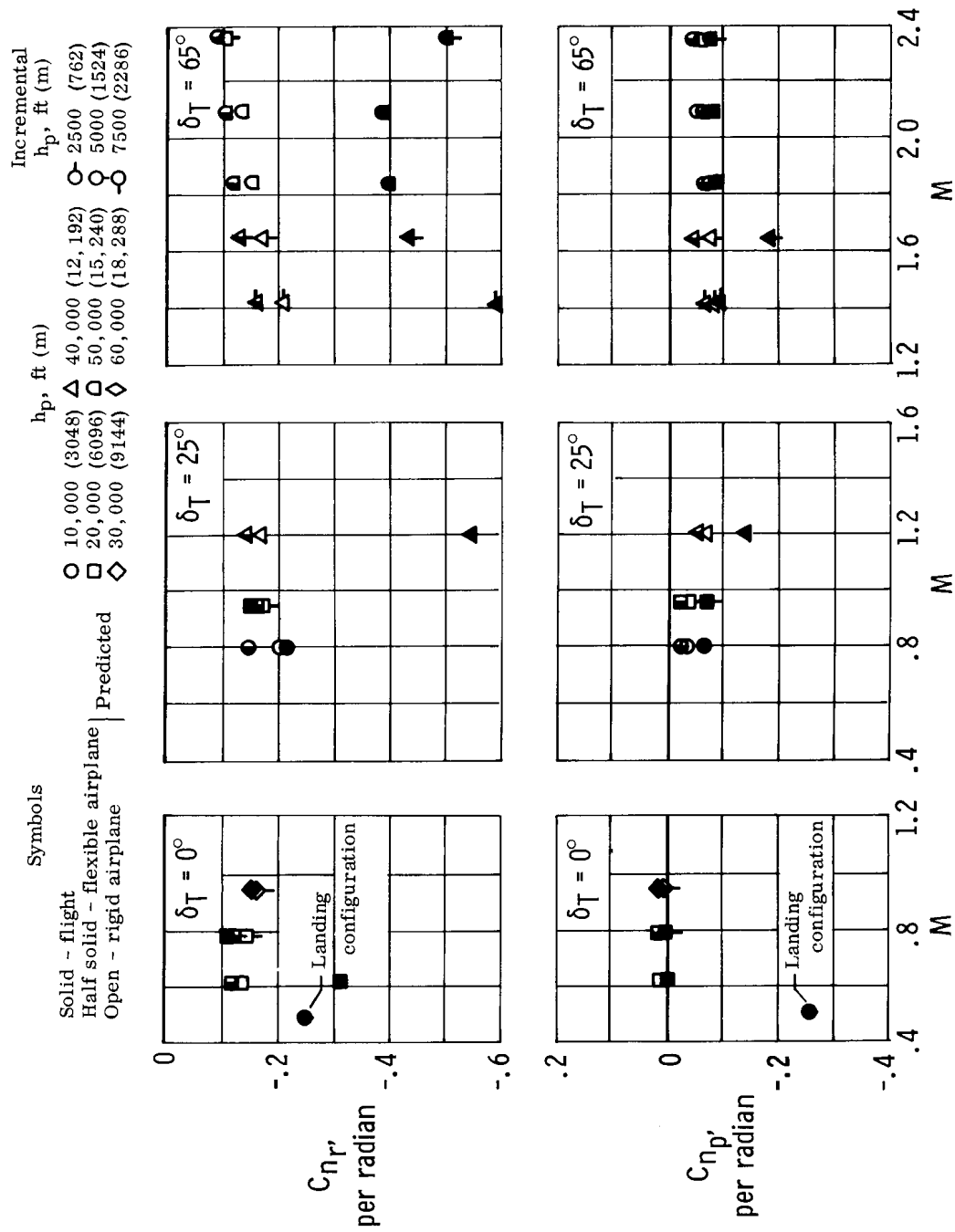
(b)  $C_{nr}$ ,  $C_{np}$ .

Figure 16. - Continued.

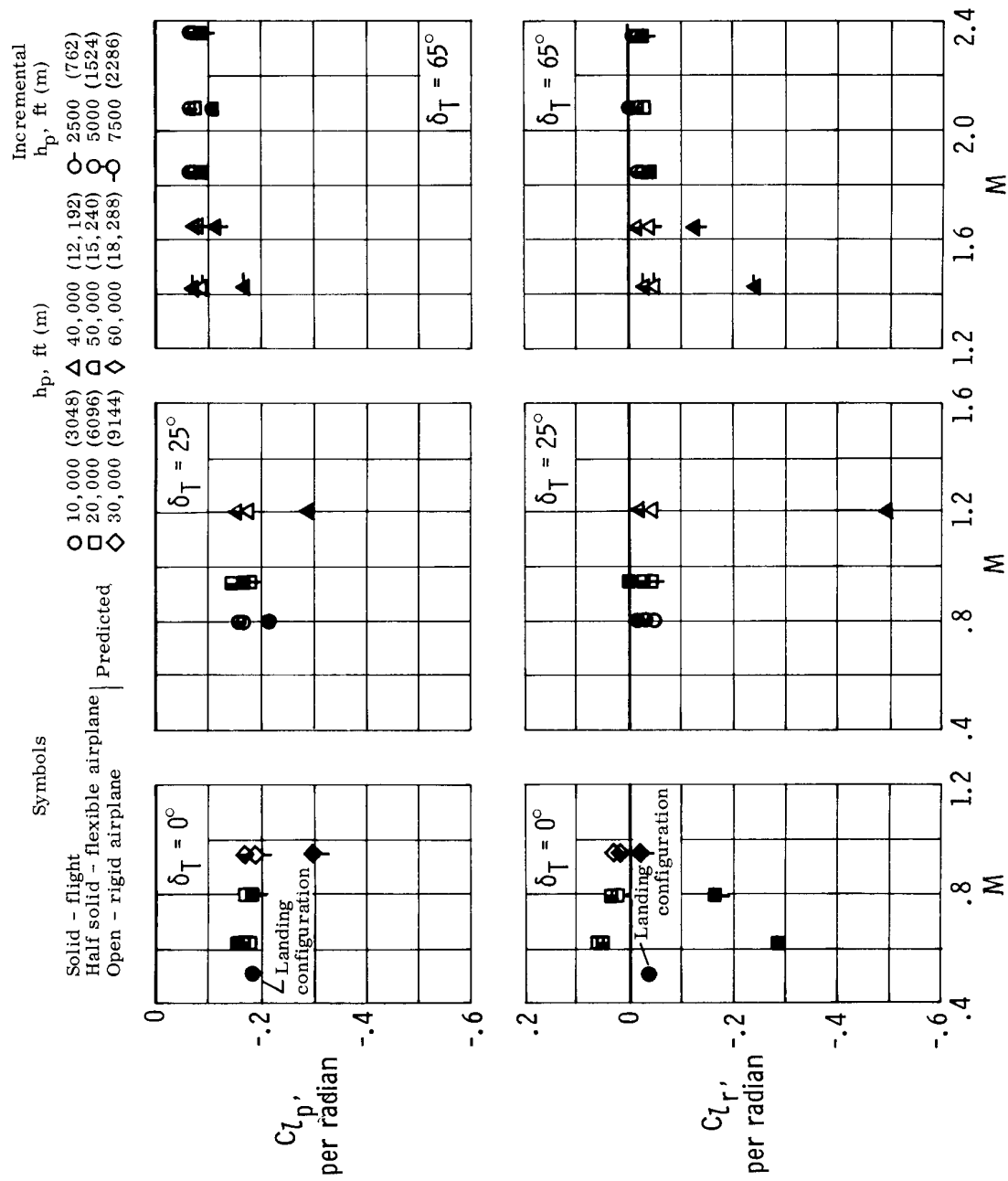
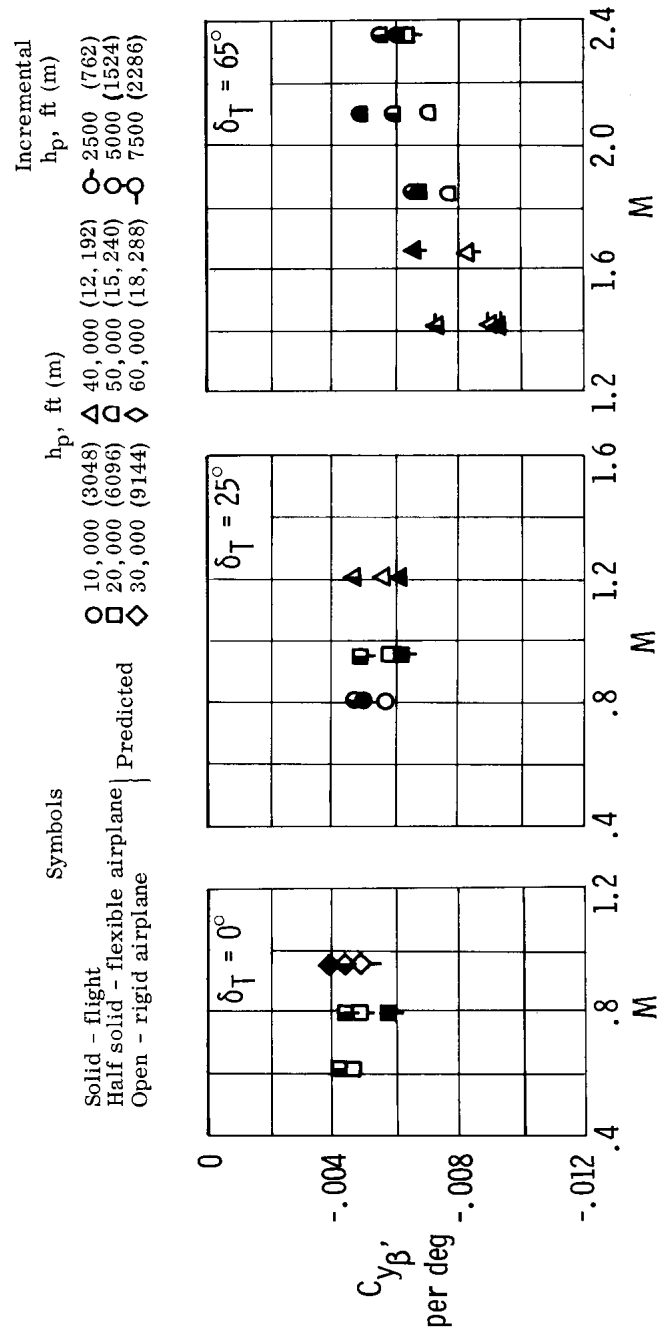


Figure 16. - Continued.



(d)  $C_{y\beta}$ .

Figure 16. - Concluded.

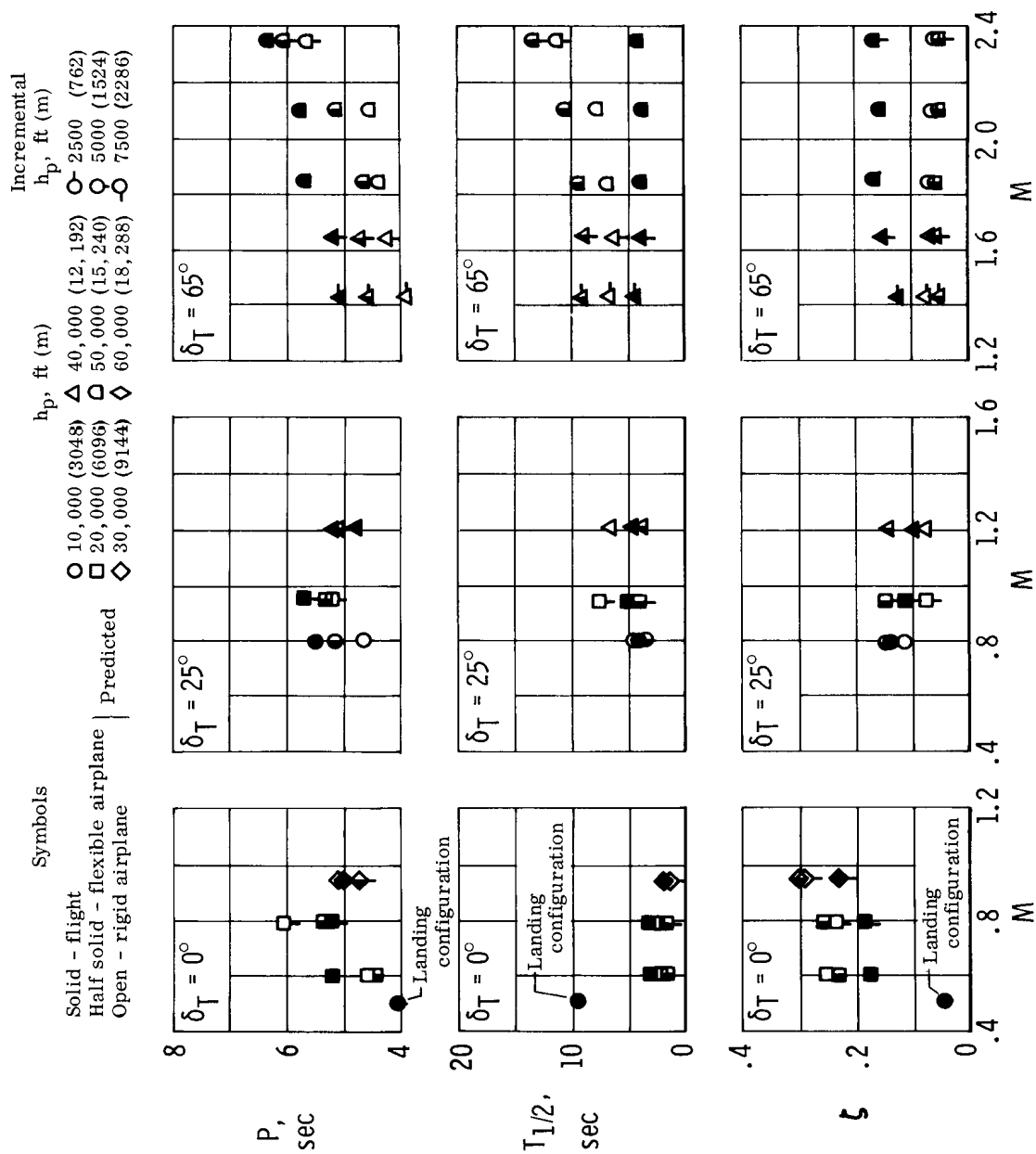


Figure 17. -- Comparison of XB-70-1 flight-determined and predicted Dutch roll period and damping. (See table IV for weight and center of gravity of individual data points.)

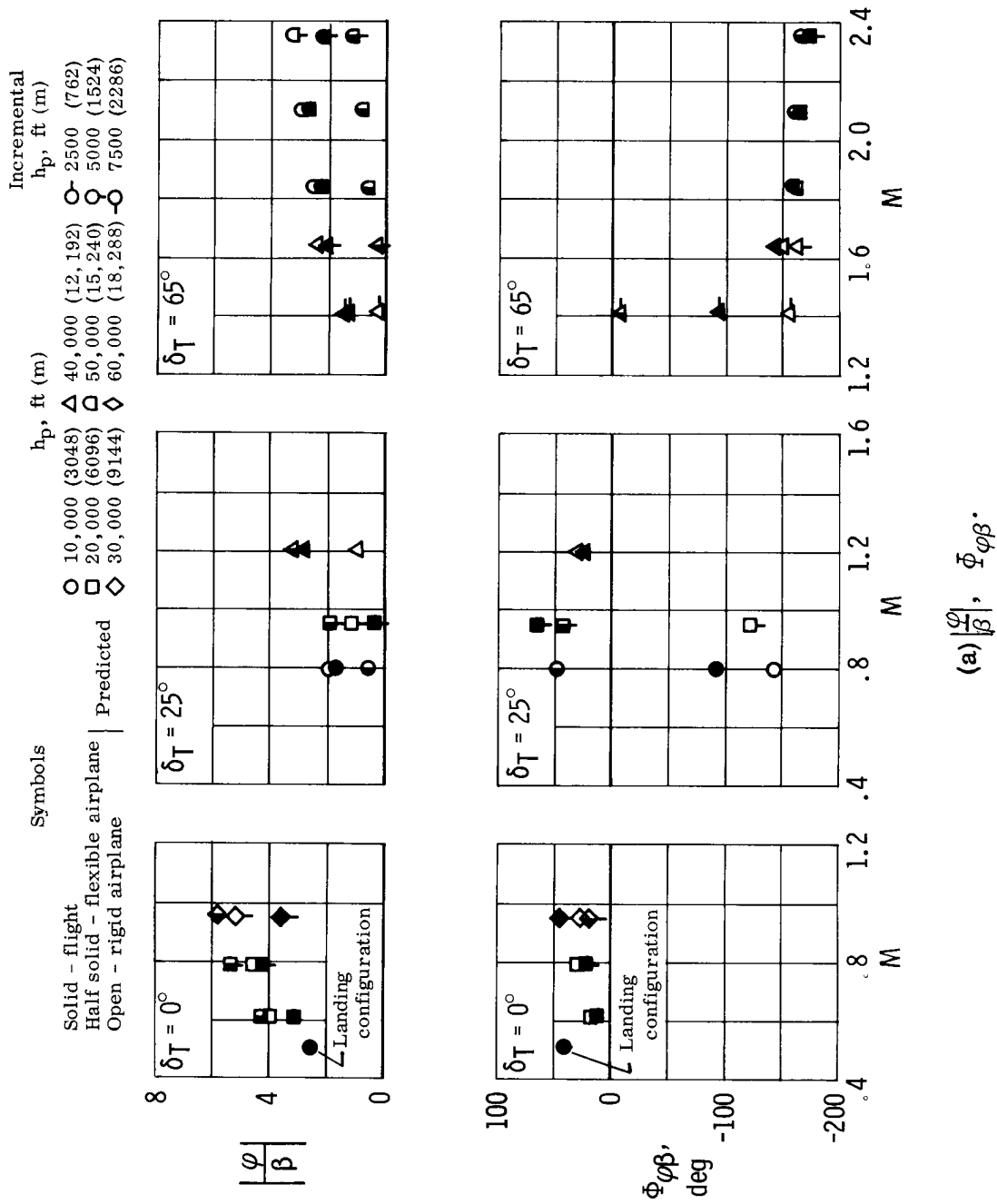
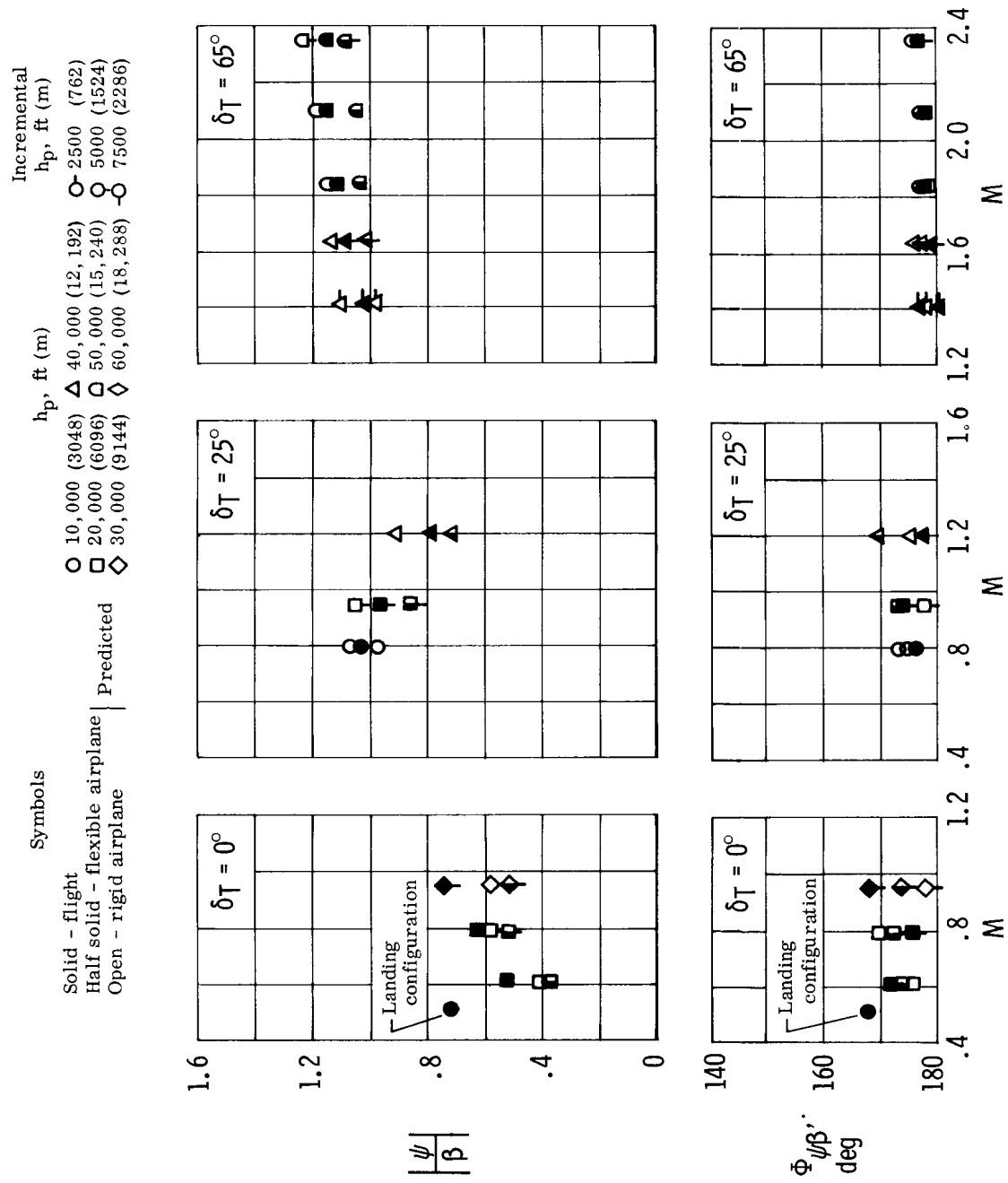


Figure 18. - Comparison of XB-70-1 flight and predicted Dutch roll amplitude ratios and phase angles. (See table IV for weight and center of gravity of individual points.)



(b)  $|\frac{\psi}{\beta}|$ ,  $\Phi_{\psi\beta}$ .

Figure 18. — Concluded.

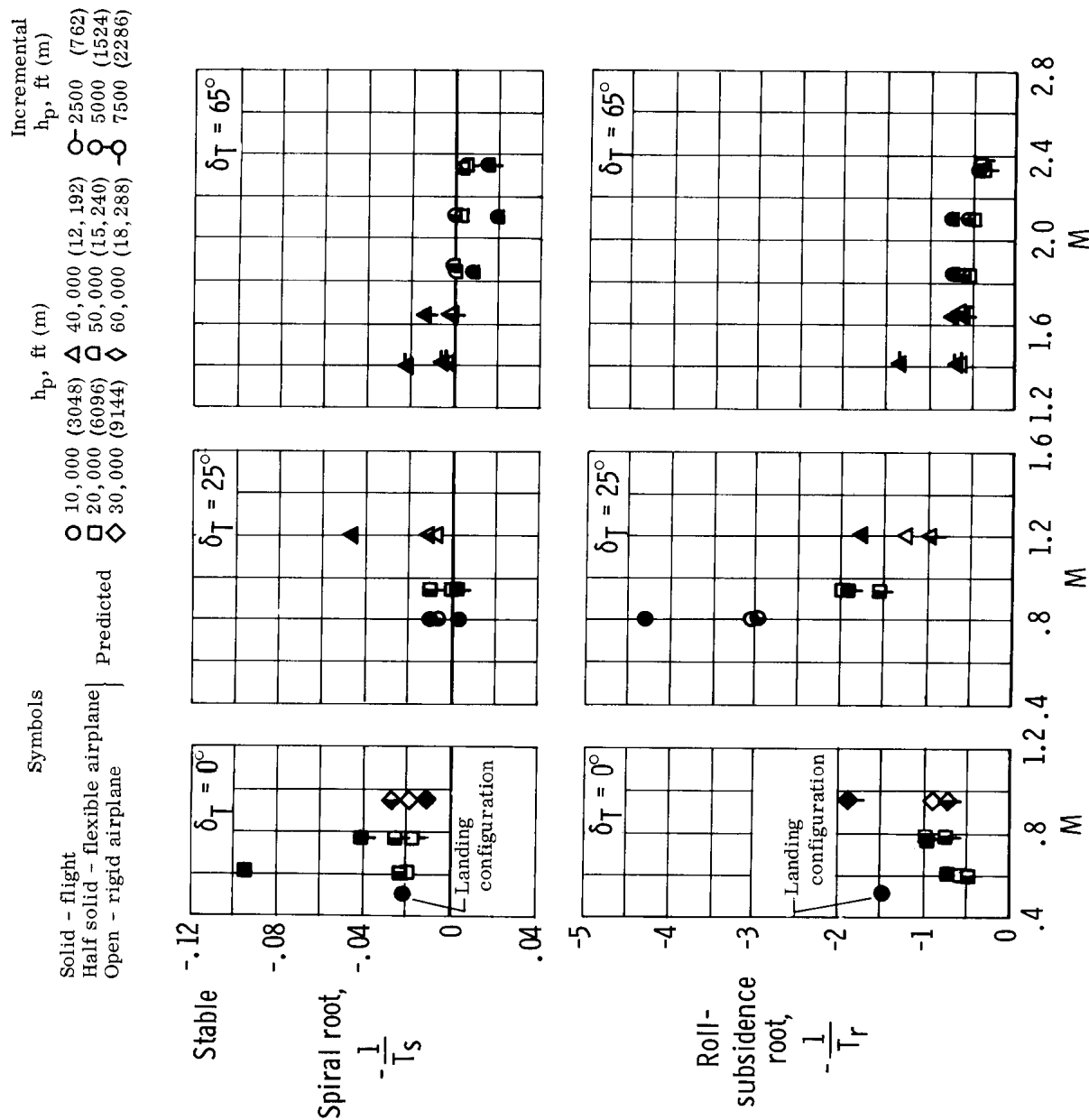
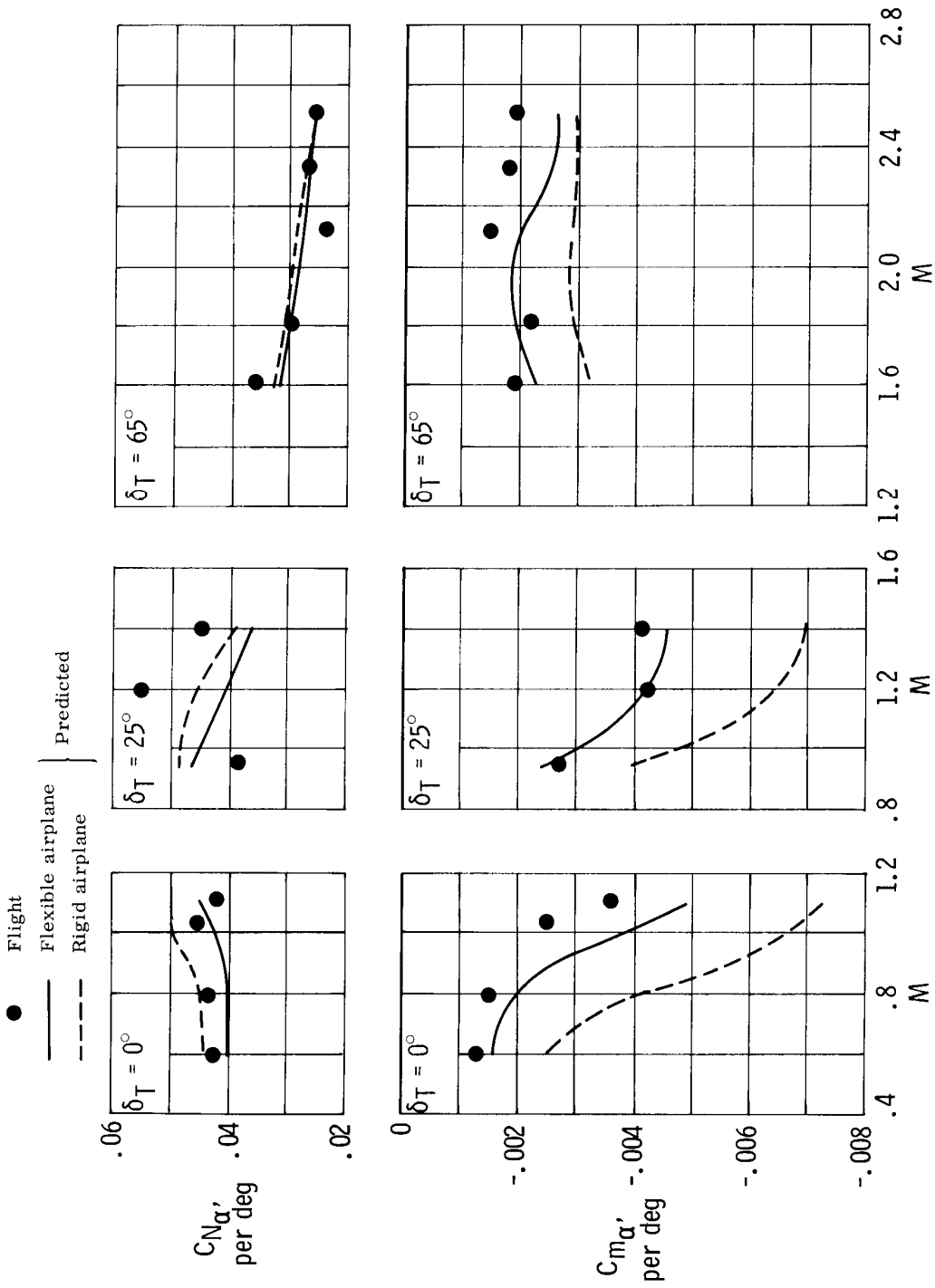
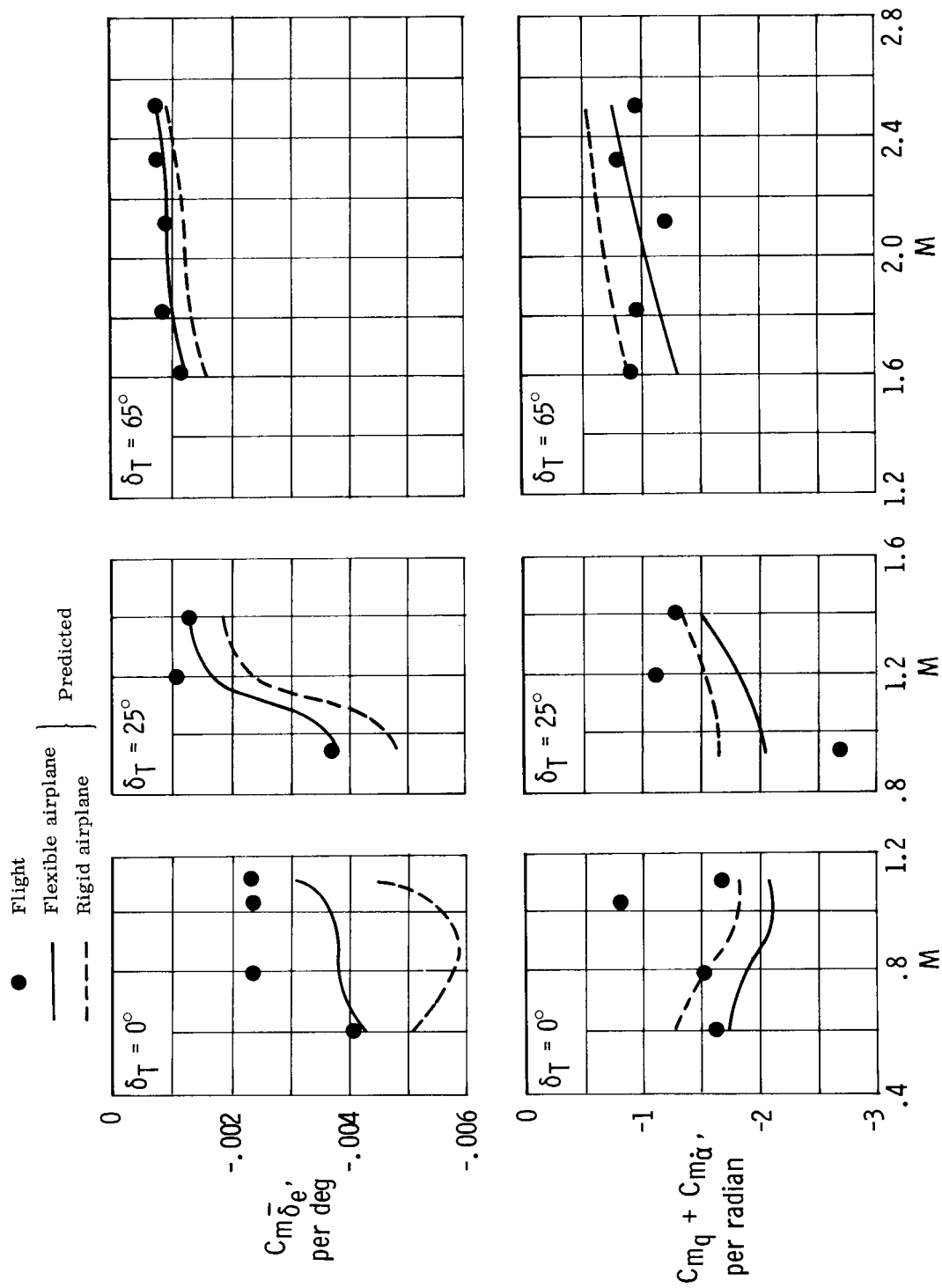


Figure 19. - Comparison of XB-70-1 flight and predicted spiral- and roll-subsubidence roots. (See table IV for weight and center of gravity of individual data points.)



(a)  $CN_{\alpha}$ ,  $Cm_{\alpha}$ .

Figure 20.— Variation of XB-70-1 flight-based and predicted longitudinal derivatives with Mach number in hypothetical climbout profile.



(b)  $Cm\bar{\delta}_e$ ,  $(Cm\delta_e + Cm\ddot{\alpha})$ .

Figure 20. — Concluded.

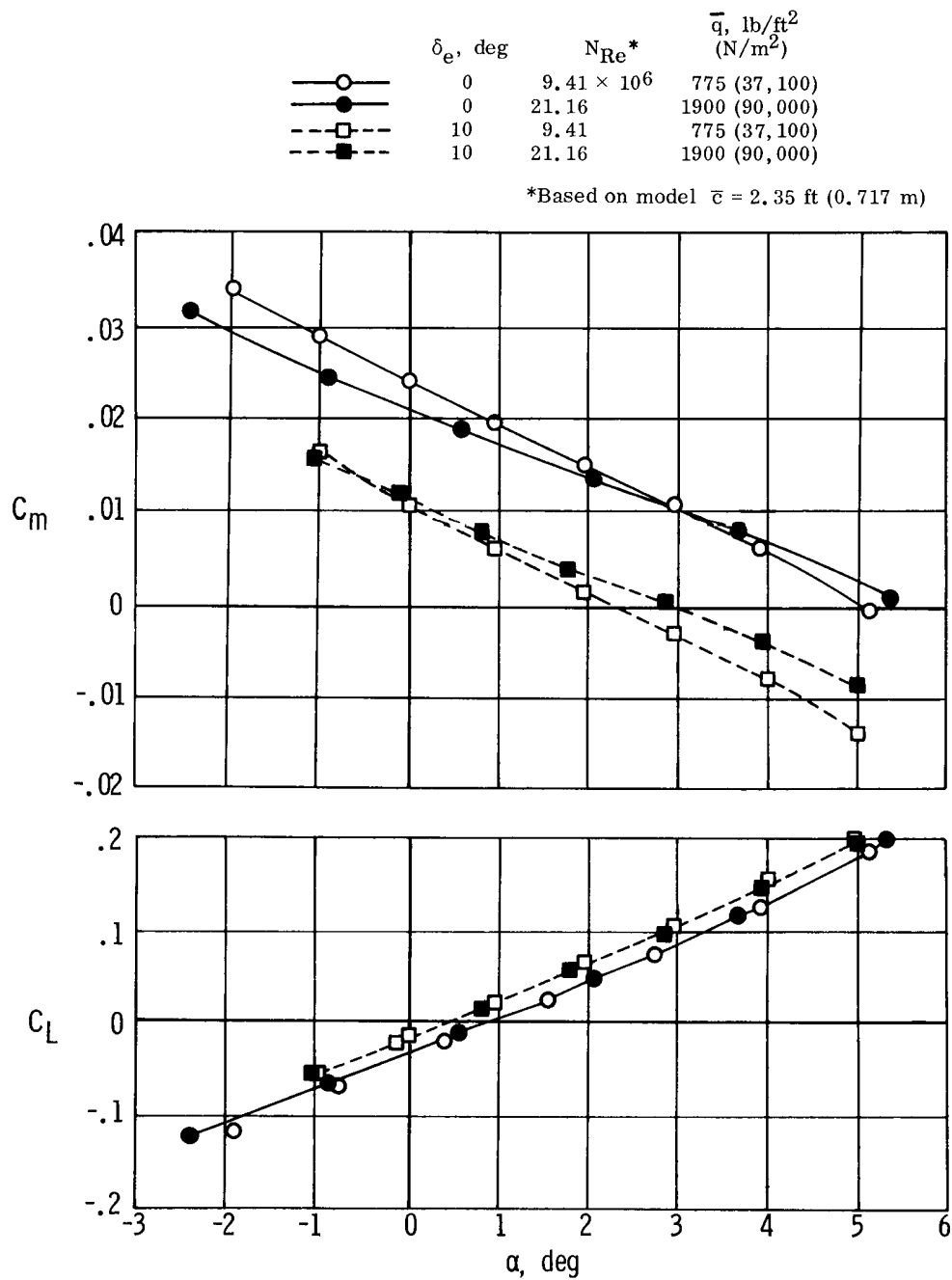


Figure 21. — Apparent effect of Reynolds number on longitudinal characteristics of 0.03-scale rigid model of XB-70-2 from tests in Ames 11- by 11-foot wind tunnel.  $M = 1.2$ ;  $\delta_T = 30^\circ$ ;  $\delta_C = 0^\circ$ .

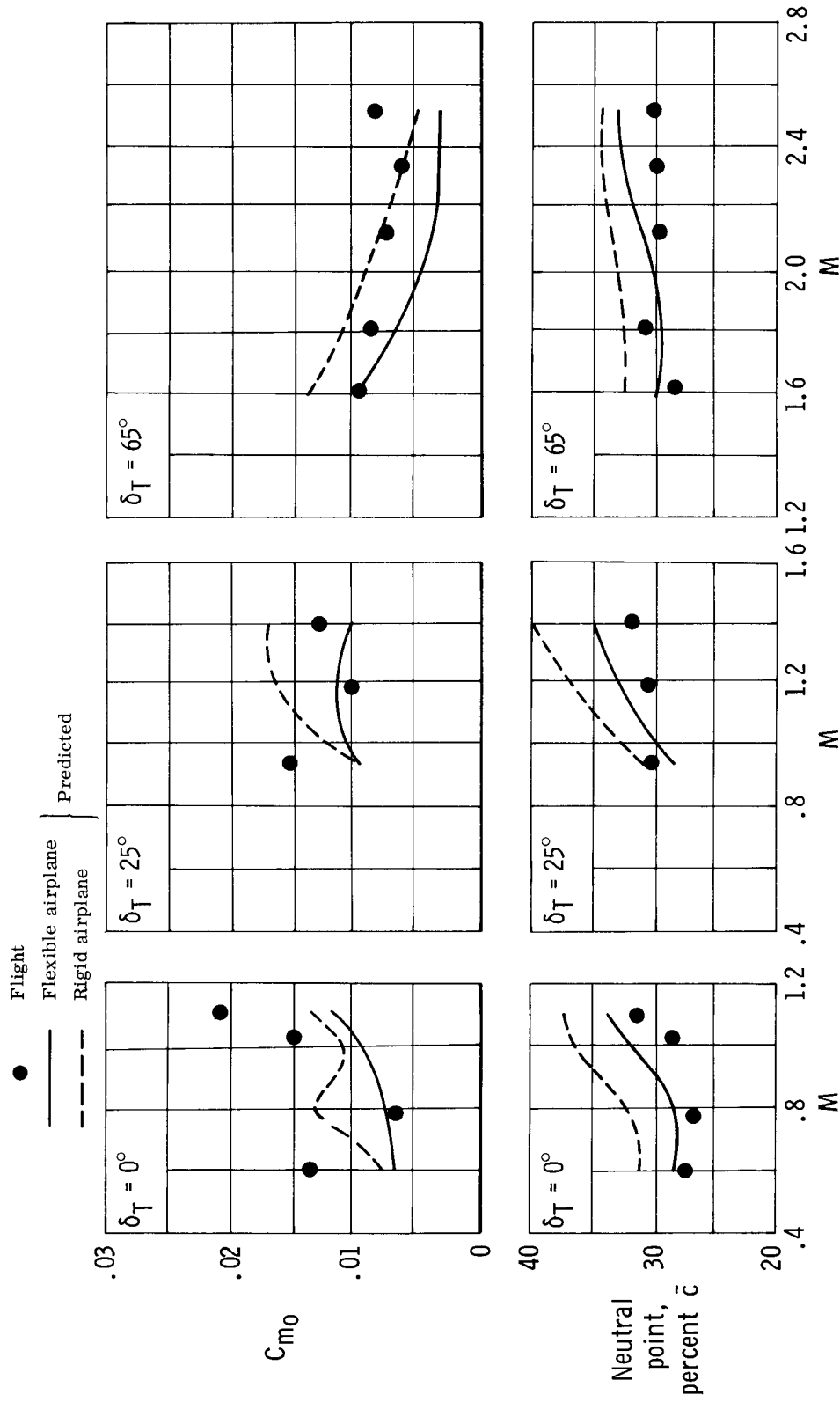


Figure 22. – Variation of XB-70-1 flight-based and predicted neutral point and pitching-moment coefficient at zero lift ( $\delta_c = \delta_e = 0$ ) with Mach number in hypothetical climbout profile.

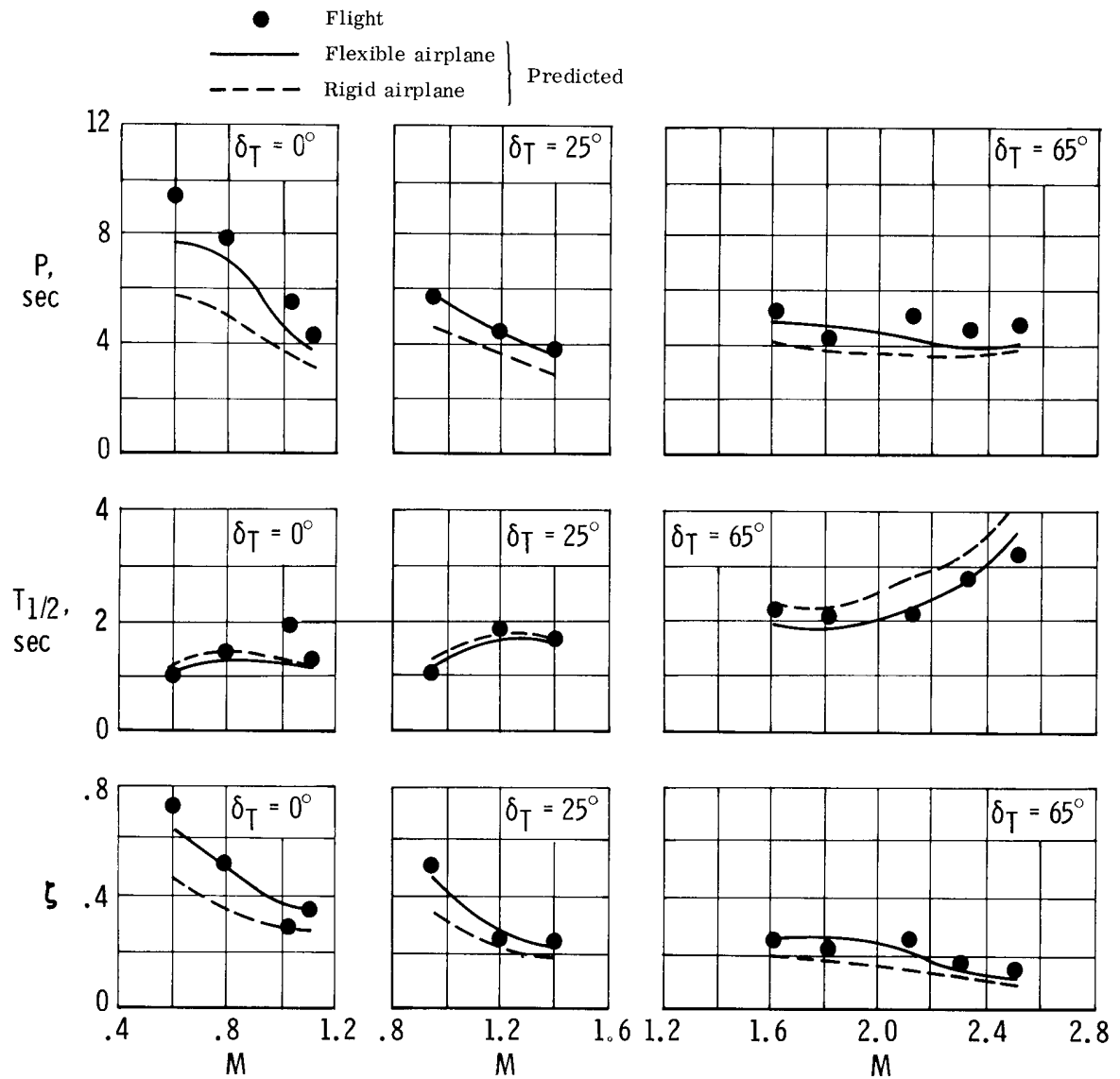


Figure 23.— Variation of XB-70-1 flight-based and predicted longitudinal period and damping with Mach number in hypothetical climbout profile.

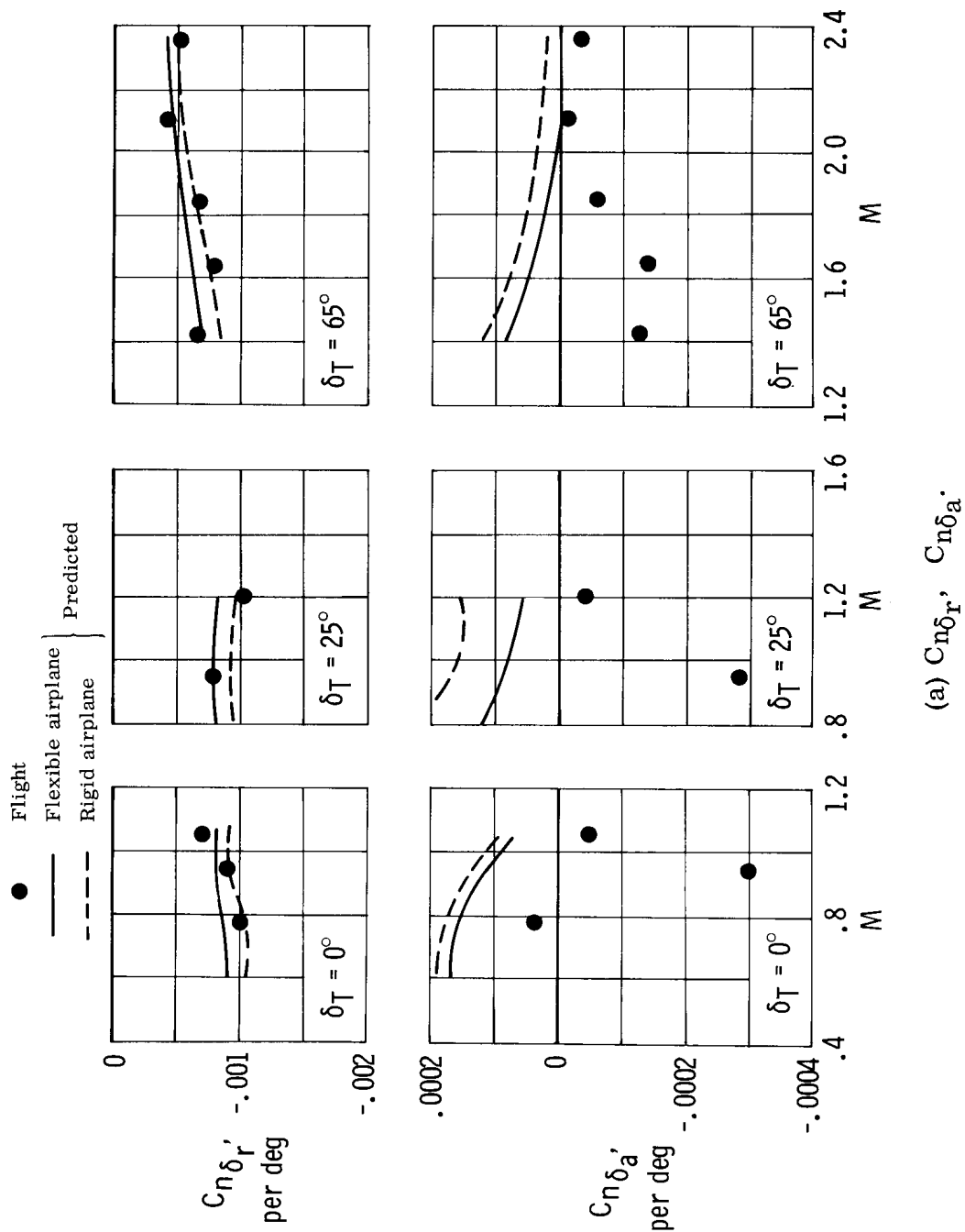
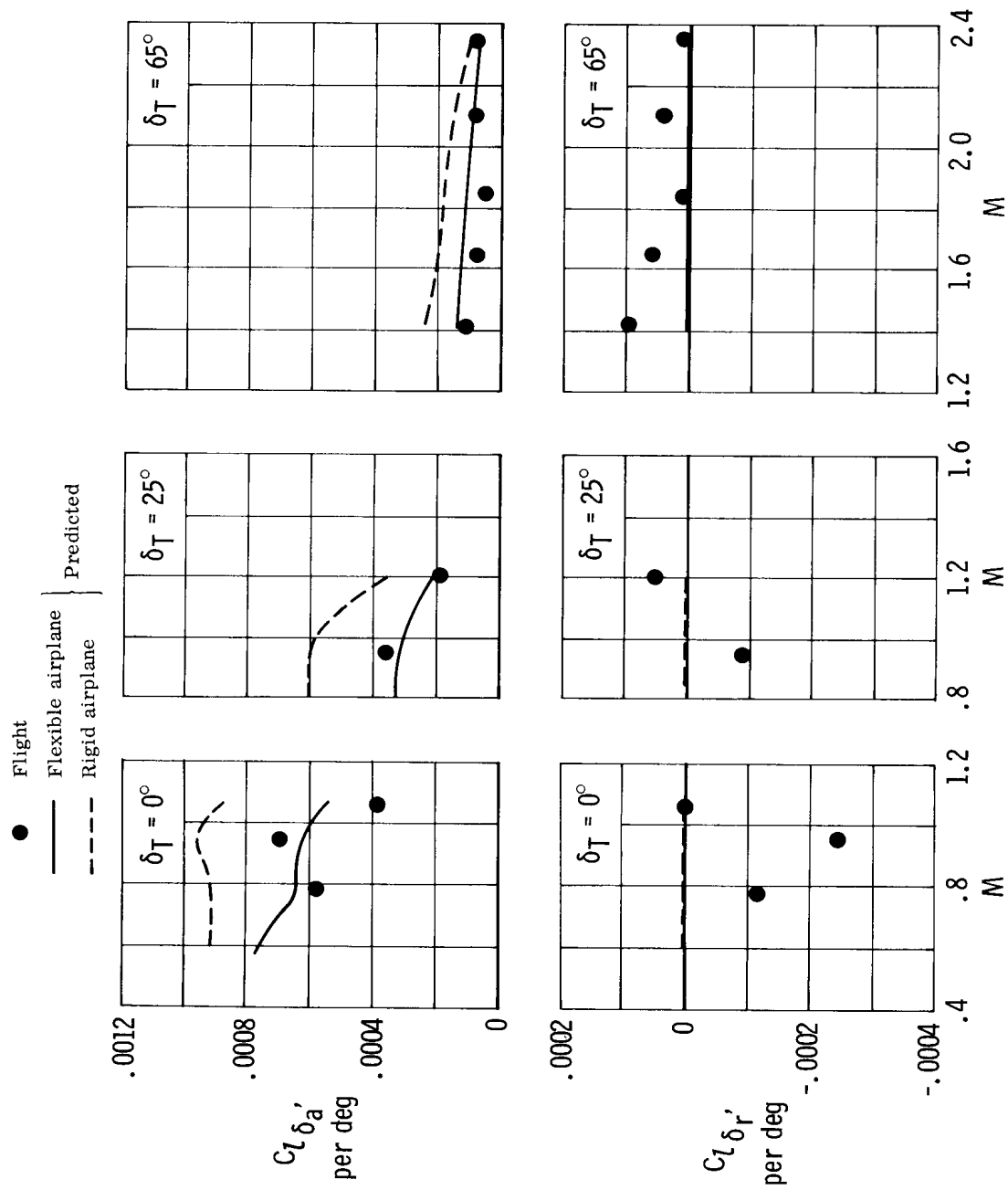
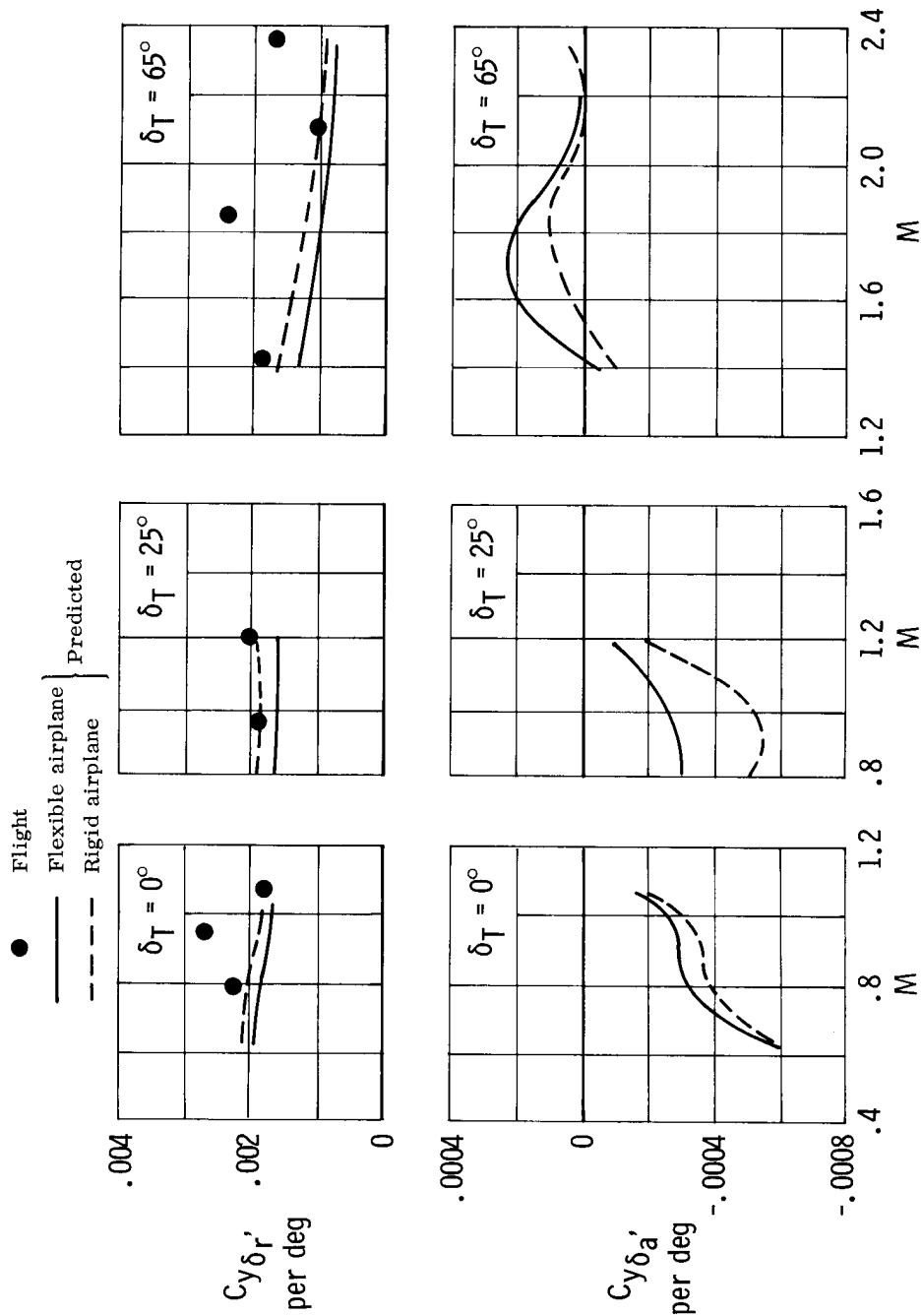


Figure 24. — Variation of XB-70-1 flight-based and predicted lateral-directional control derivatives with Mach number in hypothetical climbout profile.



(b)  $C_L \delta_a'$ ,  $C_L \delta_r'$

Figure 24. — Continued.



(c)  $C_{y\delta_r}$ ,  $C_{y\delta_a}$ .

Figure 24. — Concluded.

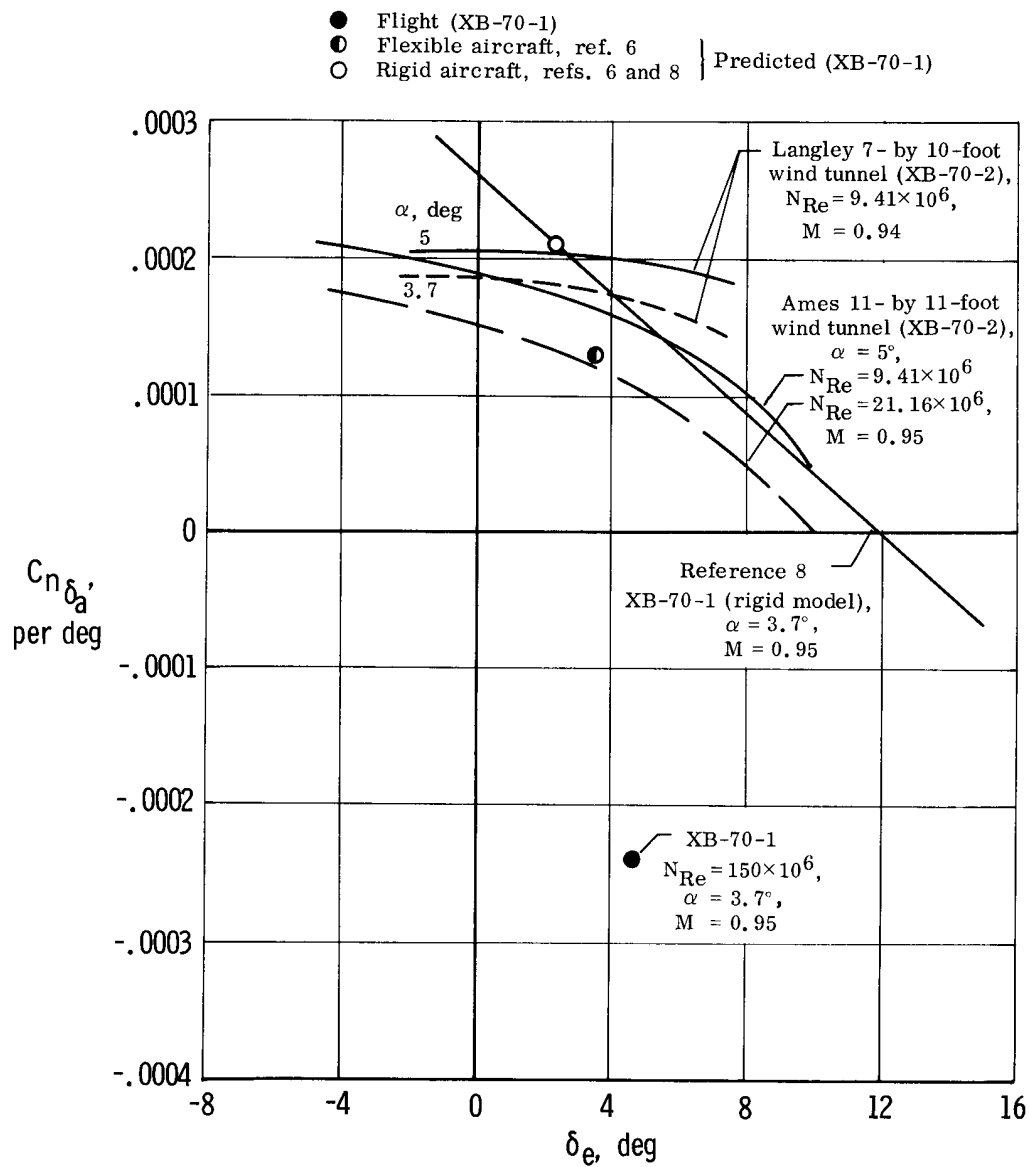


Figure 25.— Influence of Reynolds number, angle of attack, and elevator position on  $C_{n\delta_a}$  at  $M \approx 0.95$  with wing tips at half-deflected position. Included are flight-determined and corresponding predicted values of  $C_{n\delta_a}$  for one flight test point.

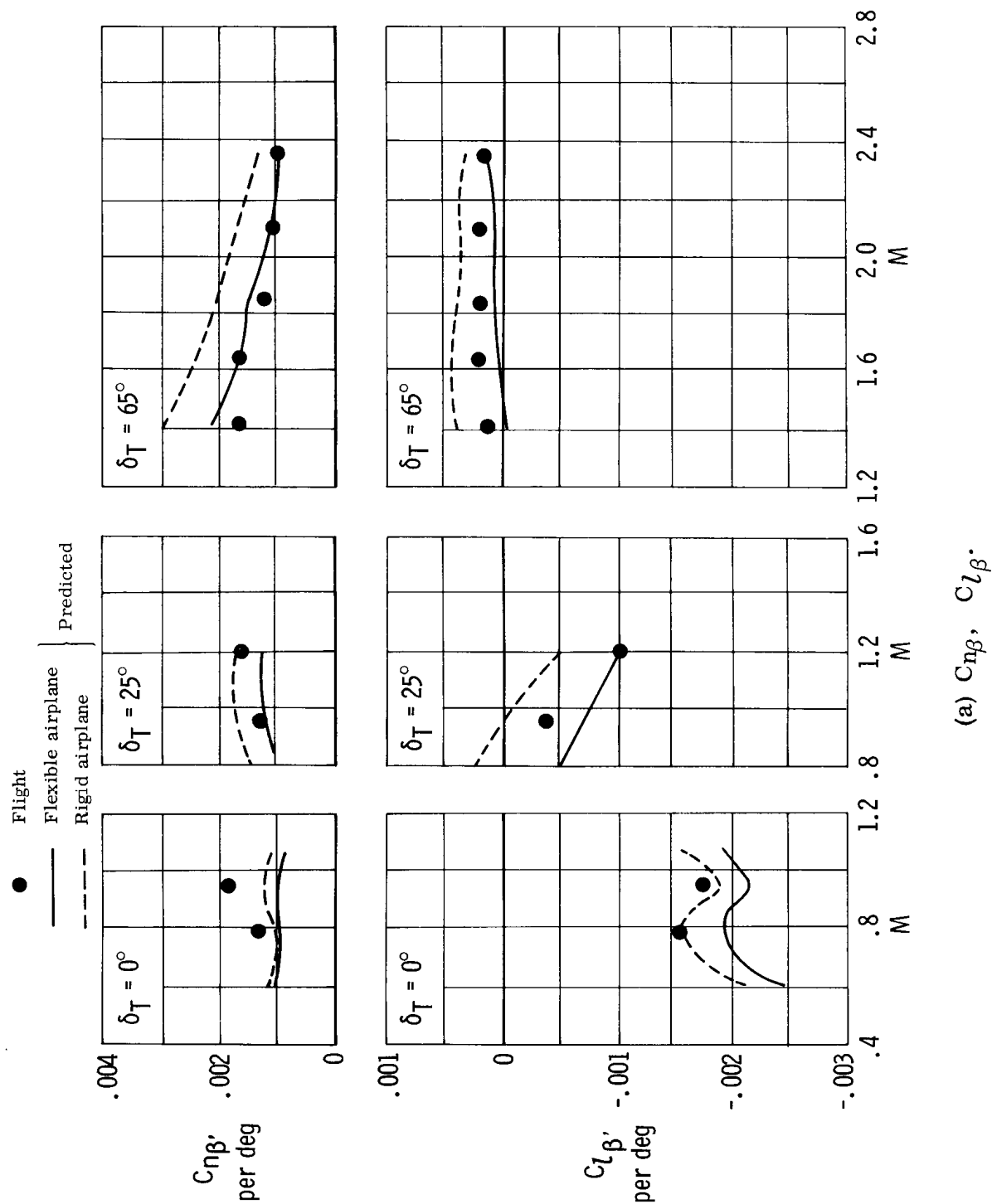
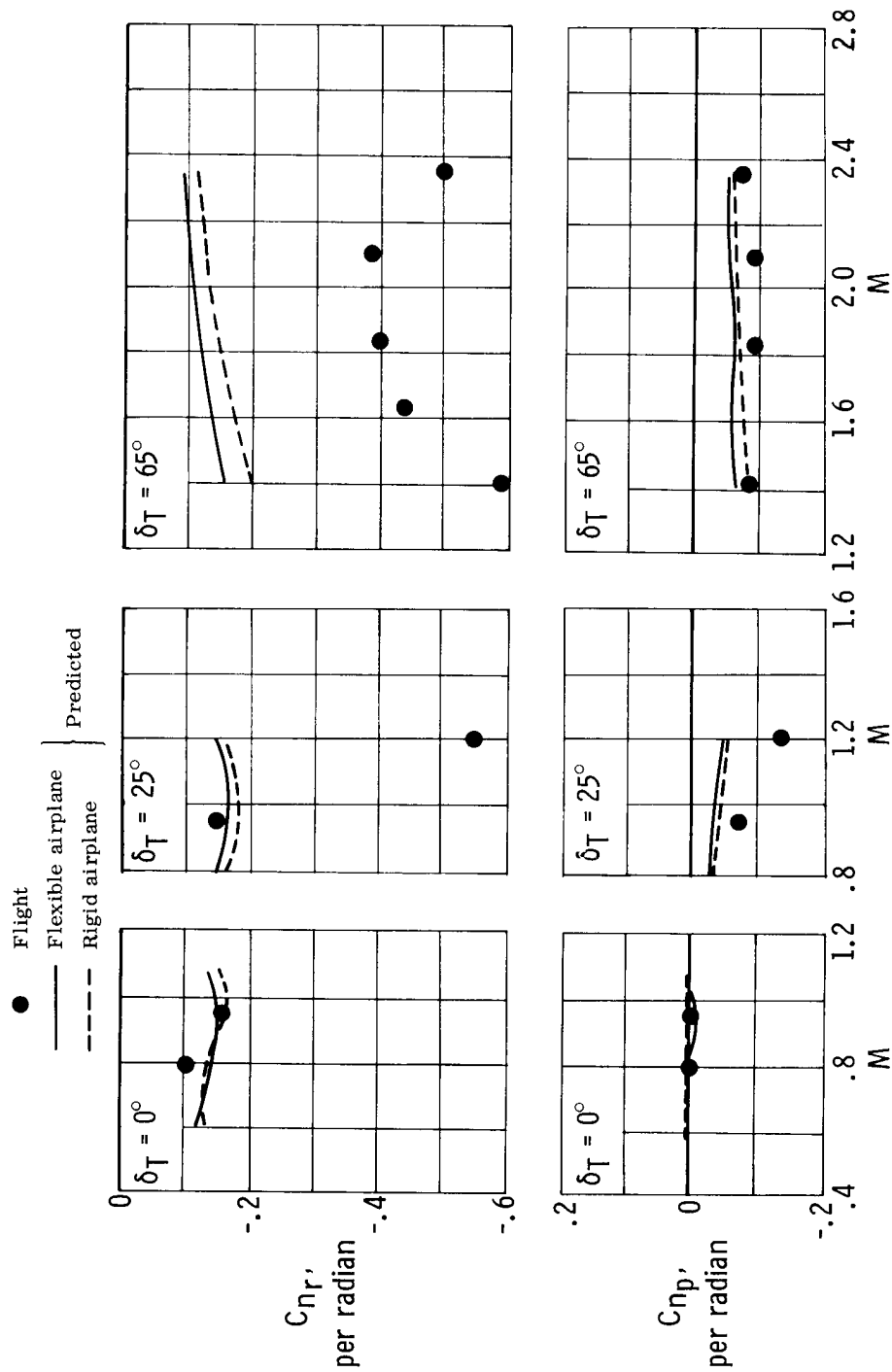
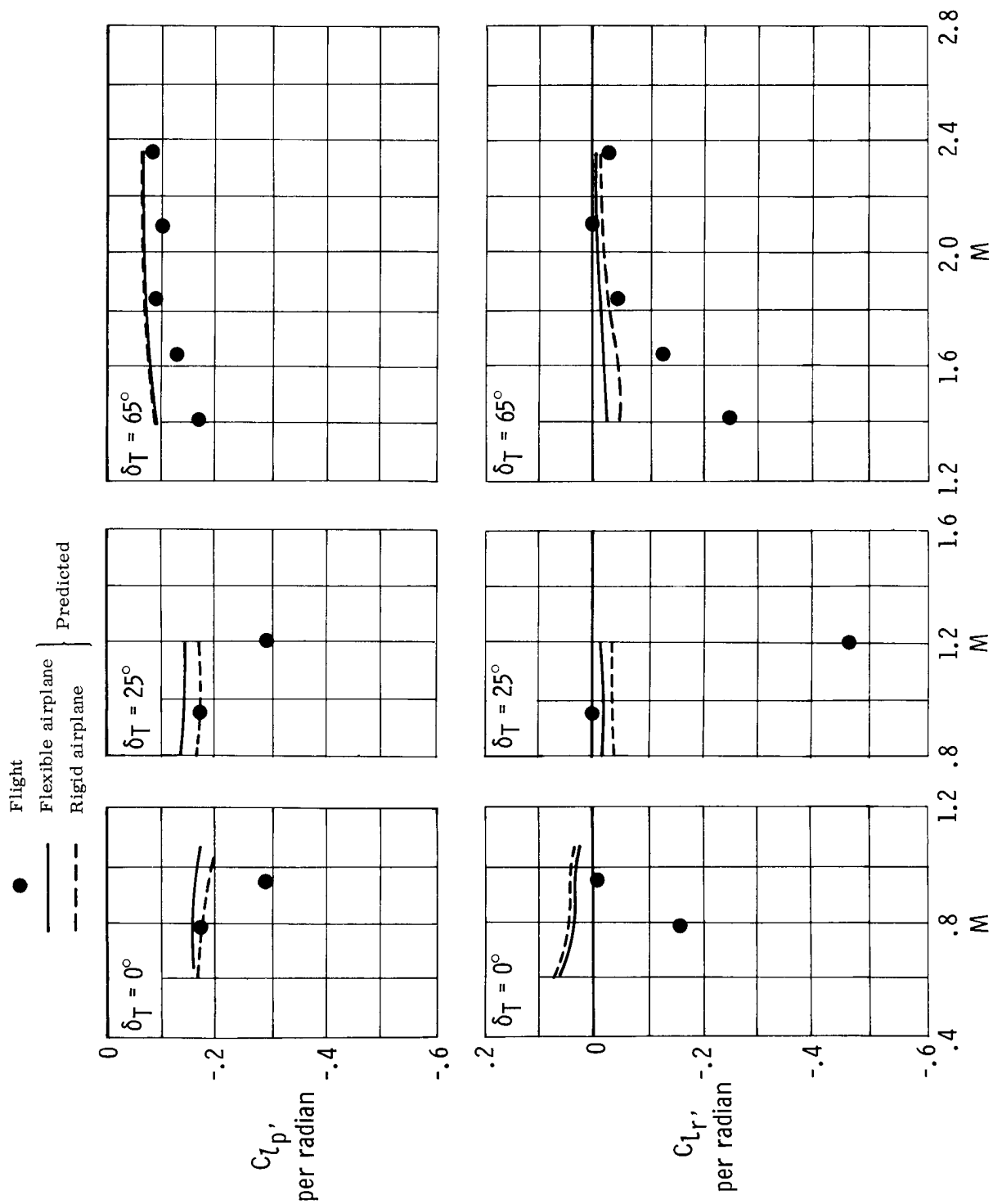


Figure 26. — Variation of XB-70-1 flight-based and predicted lateral-directional stability derivatives with Mach number in hypothetical climbout profile.



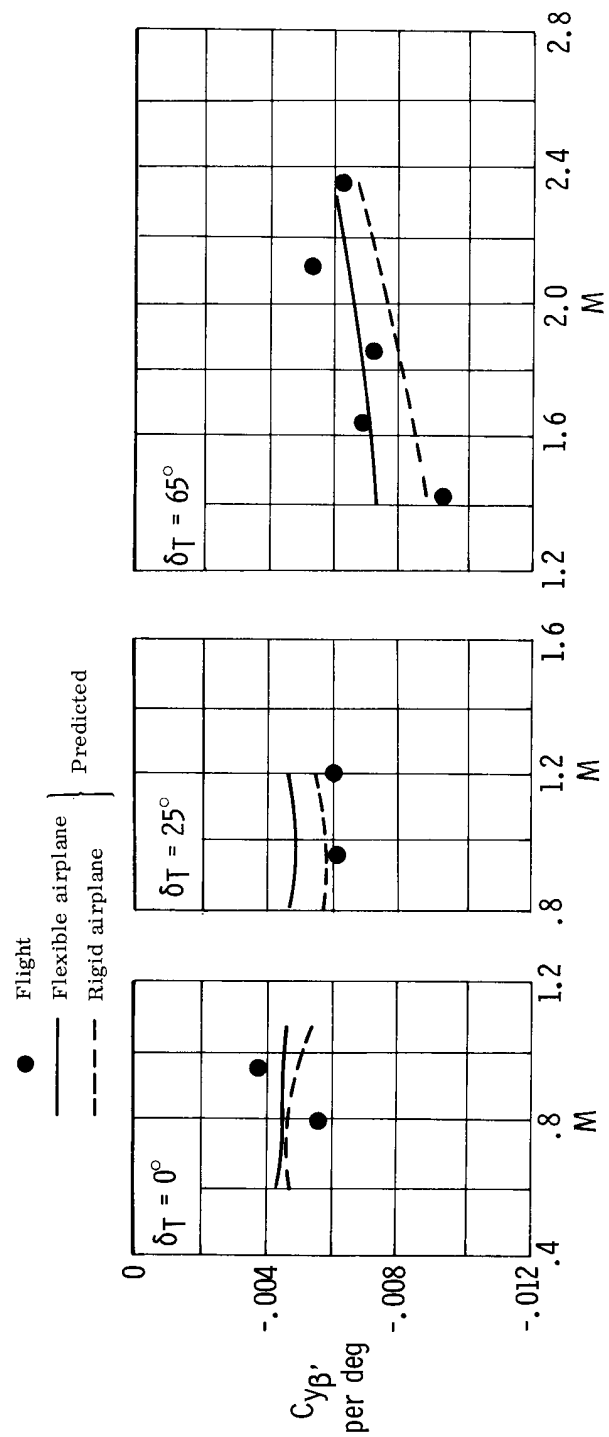
(b)  $C_{nr}$ ,  $C_{np}$ .

Figure 26. — Continued.



(c)  $C_{l_p}'$ ,  $C_{l_r}'$ .

Figure 26. — Continued.



(d)  $C_{y\beta'}$ .

Figure 26. — Concluded.

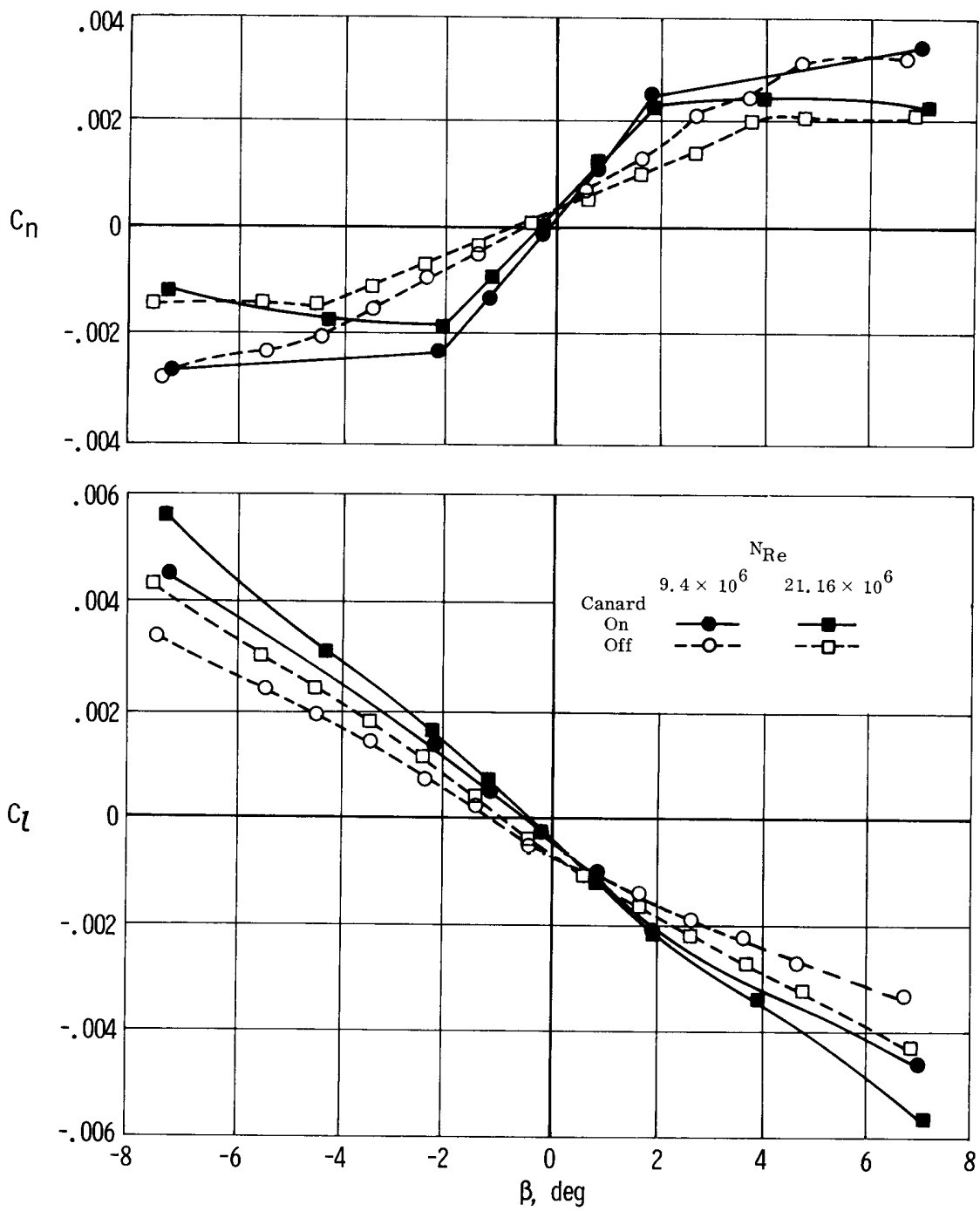


Figure 27.— Effect of canard on yawing- and rolling-moment coefficients as a function of angle of sideslip and Reynolds number from tests in Ames 11- by 11-foot tunnel. XB-70-2;  $\delta_T = 30^\circ$ ;  $\delta_C = 0^\circ$ ;  $\delta_e = 0^\circ$ ;  $\delta_a = 0^\circ$ ;  $M = 1.2$ ;  $\alpha = 5^\circ$ .

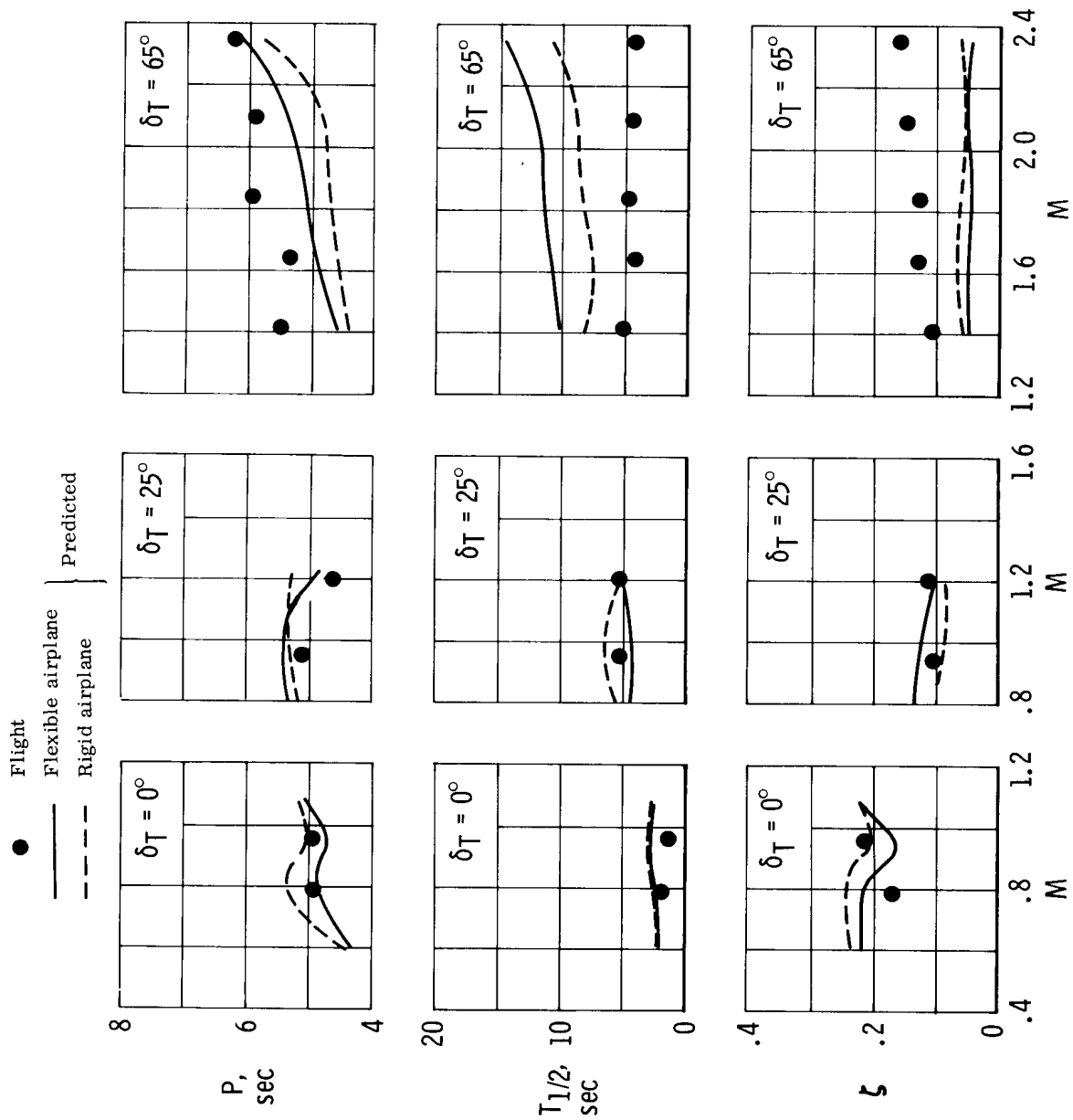


Figure 28. — Variation of XB-70-1 flight-based and predicted Dutch roll period and damping with Mach number in hypothetical climbout profile.

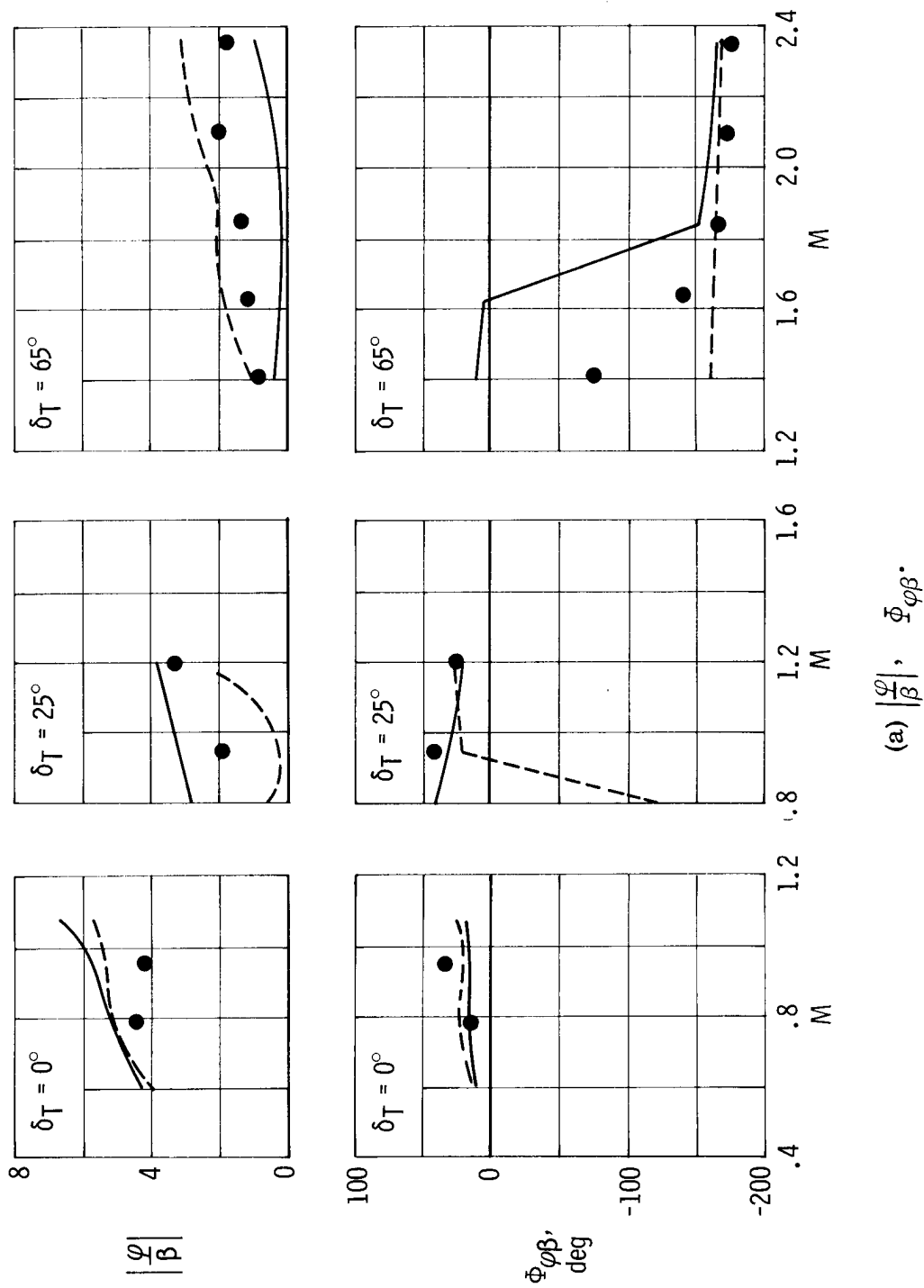
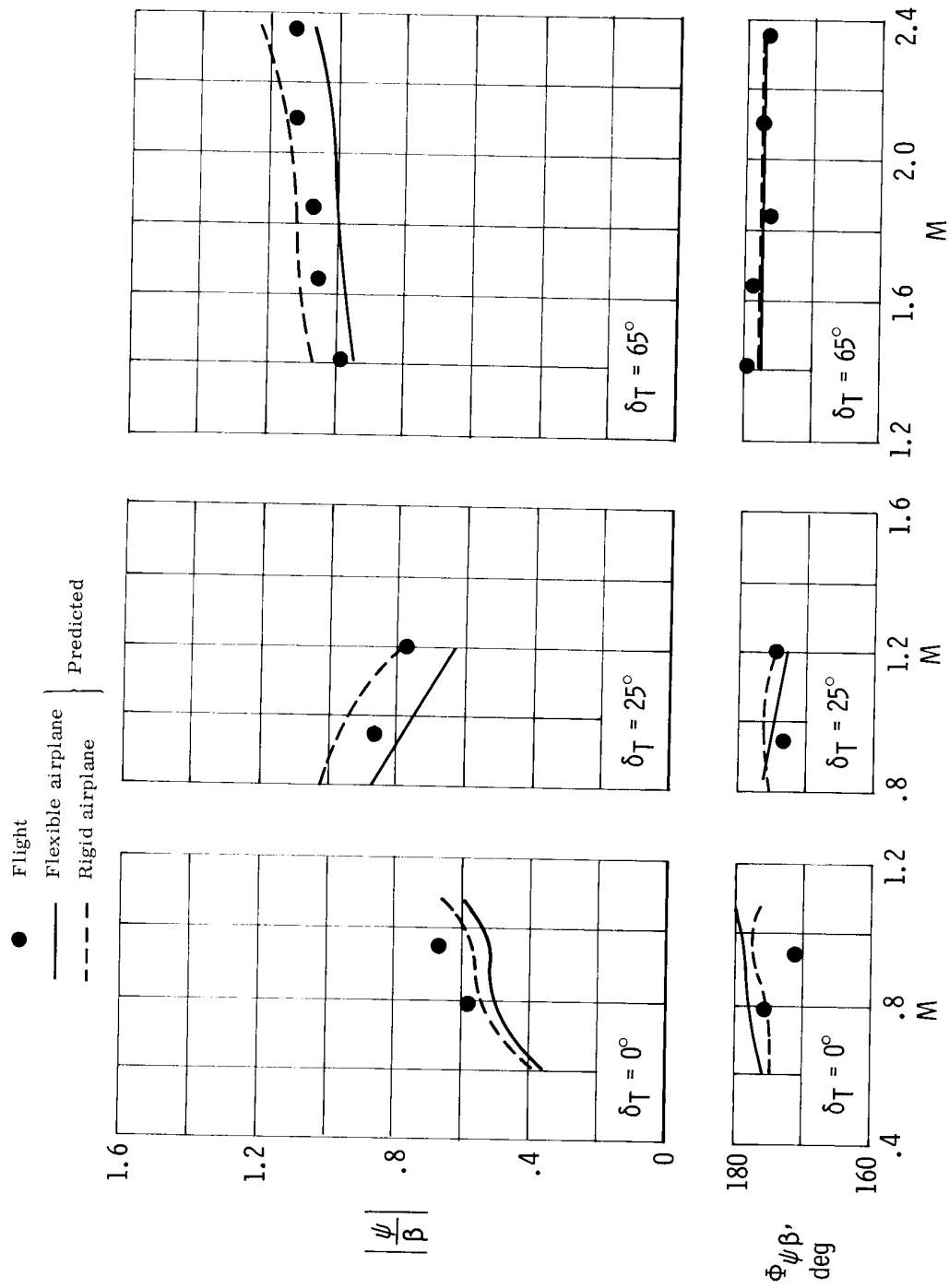


Figure 29. — Variation of XB-70-1 flight-based and predicted Dutch roll amplitude ratios and phase angles with Mach number in hypothetical climbout profile.



(b)  $\left| \frac{\psi}{\beta} \right|, \Phi_{\psi\beta}$ .

Figure 29. — Concluded.

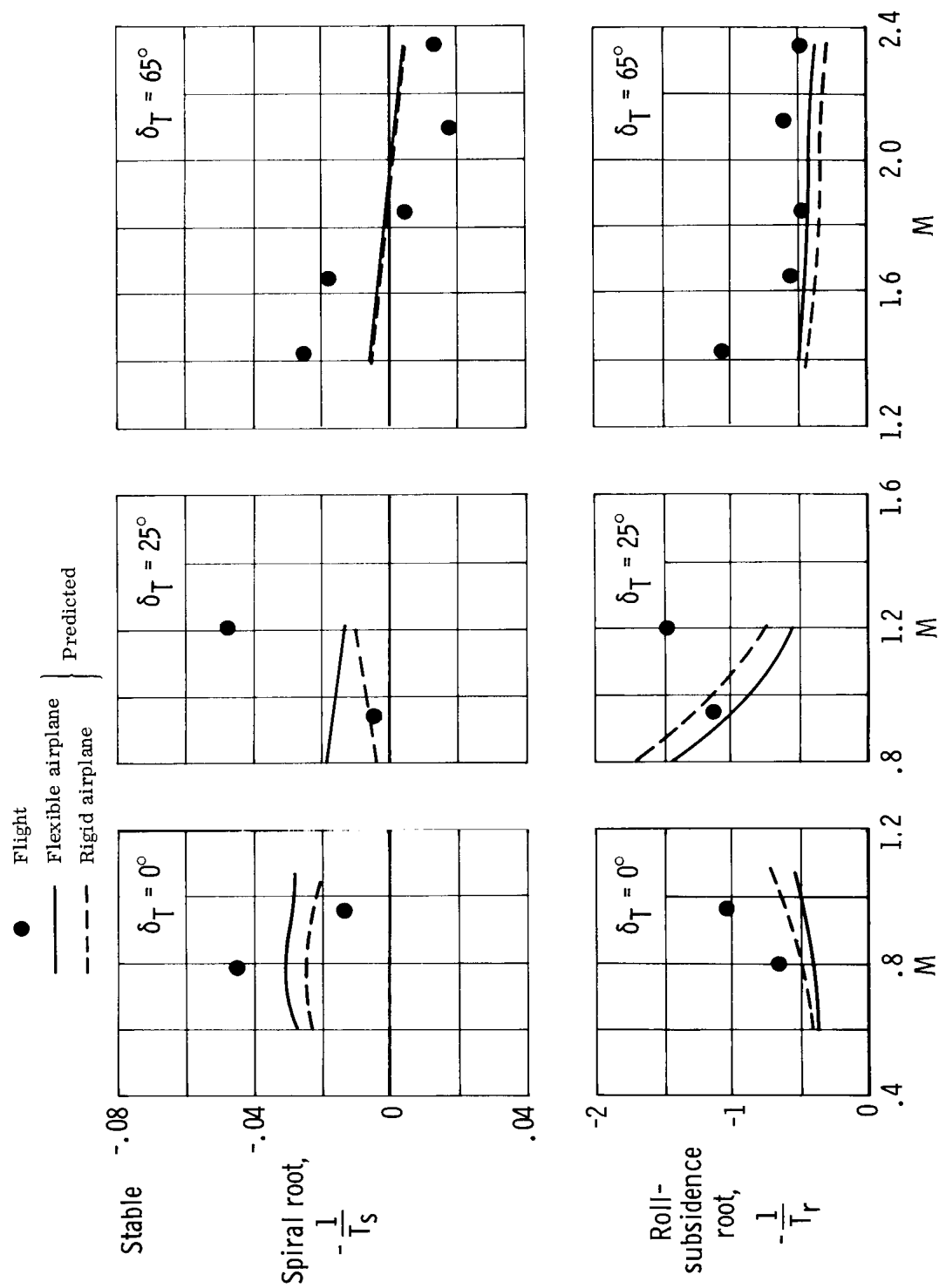


Figure 30.— Variation of XB-70-1 flight-based and predicted spiral- and roll-subsubsidence roots with Mach number in hypothetical climbout profile.